



Dipl.-Ing. Bettina Schafzahl, BSc

**The Aprotic Li-O₂ Battery
Fighting the Detrimental Impacts of Oxygen**

DISSERTATION

zur Erlangung des akademischen Grades
Doktorin der technischen Wissenschaften
eingereicht an der

Technischen Universität Graz

Betreuer

Assoc. Prof. Dipl.-Ing. Dr. techn. Christian Slugovc

Institut für Chemische Technologie von Materialien

Dipl.-Ing. Dr. sc. ETH Stefan A. Freunberger

Graz, Januar 2018

EIDESSTATTLICHE ERKLÄRUNG

Ich erkläre an Eides statt, dass ich die vorliegende Arbeit selbstständig verfasst, andere als die angegebenen Quellen/Hilfsmittel nicht benutzt, und die den benutzten Quellen wörtlich und inhaltlich entnommenen Stellen als solche kenntlich gemacht habe. Das in TUGRAZonline hochgeladene Textdokument ist mit der vorliegenden Dissertation identisch.

Datum

Unterschrift

'The greatest teacher, failure is.'

Master Yoda (Episode VIII)

Danksagung

Ich möchte mich bei all jenen bedanken, die mir über die letzten Jahre hinweg geholfen haben.

Ich bin meinen beiden Betreuern, Prof. Christian Slugovc und Dr. Stefan A. Freunberger, sehr dankbar, dass sie mir die Möglichkeit gegeben haben, an diesem sehr interessanten aber auch anspruchsvollen Thema der Li-O₂ Batterien arbeiten zu dürfen. Sie sind mir beide immer bei Problemen jeder Art zur Seite gestanden, und haben mir wann immer notwendig neue Denkanstöße gegeben und mit mir erhaltene Ergebnisse diskutiert. Außerdem war es mir durch sie möglich, meinen Horizont auf mehreren internationalen Konferenzen zu erweitern.

Einfach nur ‚Danke‘ sagen kann ich auch zu meinen lieben Schreibraumkollegen der letzten drei Jahre, Aleksej, Chrissi, Petra und Simone. Egal ob fachliche Gespräche und Hilfen oder ein Witz an passender (oder manchmal auch unpassender) Stelle, sie waren immer für mich da und haben mich großartig unterstützt. Ich möchte mich auch bei dem restlichen ‚Team Kellerassel‘, Anita, Christian, Eléonore, Luki, Mani, Nika, und Yann für die gemeinsame Zeit bedanken. Egal ob gemeinsame Mittagspause oder Kellerexpedition, ohne euch wäre es bestimmt nur halb so lustig und interessant geworden. Auch unser gemeinsames Teambuilding mit Wanderungen, Murmeltieren, Kegeln und gutem Essen wird mir immer in Erinnerung bleiben. Auch bei Anjana, Lisa, Lara, Hana und David, meinen studentischen Helfern, möchte ich mich für ihre Unterstützung und die gemeinsame Zeit bedanken. Dank gilt auch Dr. Petra Kaschnitz für NMR Messungen, Prof. Robert Saf für seine Hilfe mit dem Massenspektrometer, Ing. Josefine Hobisch für TGA Messungen und Johann Schlegl für den Bau unzähliger Messinstrumente.

Auch bei meinen Freunden möchte ich mich herzlich für ihre Unterstützung bedanken; fürs Zuhören wenn es einmal nicht lief wie es sollte, fürs Auf-andere Gedanken-bringen wenn notwendig aber auch fürs gemeinsam Freuen über gehaltene Vorträge oder publizierte Paper. Liebe Yassi, vielen Dank für deinen Beistand und deine Hilfe in den letzten Jahren. Danke Rahel und Yu für eure tolle Unterstützung und das offene Ohr bei Problemen, danke Bernd, Berni und Hari für spannende Spielnachmittage und Abende ganz ohne Chemiebezug, danke an meine Lichtbringer-Illaris-Truppe für die schönen, spannenden und lustigen gemeinsamen Abenteuer und für eure Geduld, obwohl die vorliegende Arbeit die Zeit zwischen den Spieleabenden jetzt deutlich vergrößert hat.

Weiters möchte ich auch noch meiner Familie danken. Meine Eltern, Christine und Max, haben mich schon mein ganzes Leben unglaublich gut unterstützt, an mich geglaubt und mich motiviert. Ohne ihre Hilfe wäre mein Studium nicht möglich gewesen. Auch meine Schwester Sandi war immer für mich da und hat mit den gemeinsamen Lauffreffen für einen Ausgleich zum Unialltag gesorgt. Weiteres danke ich meinen Schwiegereltern, Gisi und Hans, denn auch sie haben mich in den letzten Jahren unterstützt und mich in ihre Familie aufgenommen.

Zu guter Letzt gebührt aber der größte Dank meinem Ehemann Luki. In den letzten drei Jahren war er nicht nur ein sehr wichtiges Arbeitsgruppenmitglied, sondern hat mich auch privat in allen Aspekten unterstützt. Er hat mir mit seiner Liebe und Unterstützung die Möglichkeit gegeben, mich wann immer es notwendig war, komplett auf die Arbeit zu konzentrieren und ist mir immer mit Rat und Vorschlägen zur Seite gestanden.

Abstract

Lithium-oxygen batteries could fulfil societies growing demand for energy, as they offer the highest formal energy density of all known battery systems. Instead of intercalating ions into a crystal lattice, lithiumperoxide is formed and reversibly stored in the porous cathode material. The employed materials are readily available: oxygen can be used from the air or by utilising an oxygen tank, porous carbon is widely used as working electrode and elemental lithium as counter electrode. The immense potential of this technique could lead to a new generation of batteries; however, before being commercialised many challenges have to be overcome. Most importantly parasitic reactions accounting for a reduced cycle life, low efficiencies and an early cell death have to be tackled.

Many side products are formed in addition to lithium peroxide during discharge and all stages of charge. Neither the causes nor the mechanisms are fully understood yet. To further improve this understanding, a combined and refined method to quantify total superoxide/peroxide and carbonaceous side products was published in this work. The amount of oxygen and hydrogen peroxide is analysed by mass spectrometry and UV-Vis spectrometry yielding exact information about the total superoxide/peroxide content. Inorganic and organic carbonates/ carboxylates can be quantified by the evolution of carbon dioxide in two separate steps using pure acid and Fenton's reagent, respectively.

This method helped identifying that singlet oxygen is as a main reason for parasitic reactions in lithium-oxygen and sodium-oxygen batteries. By using various analytical methods, the formation of singlet oxygen was directly and indirectly proven during all stages of discharge and charge. Based on these results, first ideas to mitigate the negative impacts of singlet oxygen could be investigated.

Another possibility to further impede parasitic reactions is to develop a novel cathode material. Titanium carbide is already known to be a suitable and mostly inert cathode material. In the course of this work, a titanium carbide material with high surface areas and porosity was synthesised to ensure the expected cell performance. The macroporous polymer foam was impregnated with a titanium containing organic material and subsequently carbonised at high temperature under inert atmosphere leading to a hierarchically porous titanium carbide/carbon composite. It was possible to prepare cathode materials with surface areas in the range of 200-400 m² g⁻¹, porosities of approximately 90% and capacities exceeding those of titanium carbide nanoparticles tenfold.

Kurzfassung

Die Lithium-Sauerstoff Batterie könnte die steigenden Energieforderungen der Gesellschaft erfüllen, da diese über die höchste formale Energiedichte aller bekannten Batteriesysteme verfügt. Anstelle der Einlagerung von Ionen in ein Kristallgitter wird Lithiumperoxid gebildet und reversibel in der porösen Kathode gelagert. Die hierbei verwendeten Materialien sind leicht zugänglich: Sauerstoff kann aus der Luft oder mittels Sauerstofftank zugeführt werden, als Kathode wird weitestgehend poröser Kohlenstoff verwendet und als Gegenelektrode fungiert elementares Lithium. Das unglaubliche Potential dieser Technologie könnte zu einer neuen Batteriegeneration führen; jedoch müssen vor der kommerziellen Nutzbarkeit viele Herausforderungen bewältigt werden. Insbesondere verursachen parasitäre Reaktionen in der Batterie verringerte Zyklendauer, geringe Effizienz und einen frühen Zelltod.

Während des Entlade- und des Ladeprozesses entstehen zusätzlich zu Lithiumperoxid unerwünschte Nebenprodukte wie zum Beispiel Lithiumcarbonat oder organische Carbonate. Um die Ursache und in weiterer Folge die Mechanismen der Nebenproduktbildung studieren zu können, wurde eine kombinierte und verbesserte Methode entwickelt. Damit können die Mengen an Superoxid/Peroxid und kohlenstoffhaltigen Nebenprodukten bestimmt werden. Die Analyten Sauerstoff und Wasserstoffperoxid lassen auf den Gehalt an Superoxid/Peroxid schließen und wurden mit Massenspektrometrie und UV-Vis Spektrometrie quantifiziert. Der Gehalt an anorganischen und organischen Carbonaten wurde durch die Austreibung und massenspektrometrische Detektion von Kohlendioxid bestimmt.

Nicht zuletzt mit Hilfe dieser Methode wurde Singulett-Sauerstoff als einer der Hauptursachen für parasitäre Reaktionen in der Lithium-Sauerstoff und der Natrium-Sauerstoff Batterie identifiziert. Die Entstehung dieser hochreaktiven Sauerstoffspezies konnte sowohl während des Entladens und Ladens der Batterie nachgewiesen und als Ursache für parasitäre Reaktionen identifiziert werden. Auf Basis dieser Erkenntnisse konnten Wege gezeigt werden, die negativen Auswirkungen von Singulett-Sauerstoff zu minimieren.

Die Entwicklung von, unter Betriebsbedingungen stabilen Kathodenmaterialien ist eine alternative Strategie um die negativen Auswirkungen parasitäre Reaktionen zu verringern. Titancarbid wurde in der Vergangenheit als in dieser Hinsicht geeignetes, weitgehend inertes, Kathodenmaterial identifiziert. In dieser Arbeit wird nun ein Weg gezeigt, Titancarbid mit hoher Oberfläche und Porosität herzustellen und damit auch eine hohe Kapazität der Lithium-Sauerstoff Batterie zu gewährleisten. Dafür wurde ein makroporöser Polymerschäum mit titanorganischen Verbindungen imprägniert und anschließend bei hoher Temperatur unter Sauerstoffausschluss in einen hierarchisch porösen Titancarbid/Kohlenstoffschaum überführt. Dabei konnte Kathodenmaterialien mit Oberflächen im Bereich von 200-400 m² g⁻¹ und Porositäten im Bereich von 90% hergestellt werden und mit Titancarbid erreichte Kapazitäten verzehnfacht werden.

Table of Content

Danksagung	I
Abstract.....	II
Kurzfassung.....	III
1 Introduction	1
1.1 The Li-O ₂ Battery	1
1.1.1 Reactions during Cycling of a Li-O ₂ Battery.....	2
1.1.2 Problems of the Li-O ₂ Battery	4
1.2 Aspects Discussed in this Work.....	7
1.2.1 Cathode Materials	7
1.2.2 Side Product Formation.....	9
2 Cathode Analysis	11
2.1 Metal (per-)oxides.....	11
2.1.1 Oxygen Evolution with Iron(III) Salts	12
2.1.2 Peroxide Quantification with Ti(IV)-oxysulfate.....	13
2.1.3 Quantification of pure Superoxides and Peroxides	14
2.2 Quantification of Carbonaceous Compounds	16
2.2.1 Quantification of Organic Carbonates/Carboxylates	16
2.2.2 Classification in Inorganic and Organic CO ₂	17
2.3 Whole Setup	18
2.3.1 Real Cells	19
2.4 Summary.....	23
3 Porous Cathode Materials for Li-O ₂ Batteries	22
3.1 Theoretical Background	22
3.1.1 Porous Polymers.....	22
3.1.2 Porous Titanium Carbide	25
3.2 Dicyclopentadiene based Porous Materials	28
3.2.1 Polymerisation with a Porogenic Solvent	28
3.2.2 High Internal Phase Emulsion of DCPD.....	30
3.3 Titanium Containing Cathode Materials.....	40
3.3.1 Different Routes to Ti Containing Materials.....	40
3.3.2 Titanium Precursors for a Polymerisation Route.....	46
3.3.3 Ti-Norbornene based Polymers.....	47
3.3.4 pDCPD HIPE Modification with Titanium based Materials.....	52
3.4 Summary.....	63

4	Singlet Oxygen as Major Cause for Parasitic Chemistry in Metal-O ₂ Batteries.....	64
4.1	Theoretical Background.....	64
4.1.1	Properties and Synthesis of Singlet Oxygen.....	64
4.1.2	Quenching and Trapping of Singlet Oxygen.....	65
4.2	Singlet Oxygen in Li-O ₂ and Na-O ₂ Batteries.....	67
4.2.1	Summary of the Published Work.....	67
4.2.2	Search for the Right Setup.....	69
4.2.3	Cathode Analysis.....	70
4.2.4	Online Electrochemical Mass Spectrometry (OEMS).....	73
4.2.5	Pathways to Singlet Oxygen.....	76
4.3	Summary.....	78
5	Methods and Preparation.....	79
5.1	General.....	79
5.1.1	Chemicals.....	79
5.1.2	Analytical Methods.....	79
5.1.3	Battery Setup.....	80
5.2	Method for Electrode Analysis.....	82
5.2.1	Sample Preparation.....	82
5.2.2	Calibration.....	83
5.3	Preparative Work.....	84
5.3.1	High Internal Phase Emulsion Polymerisation of Dicyclopentadiene.....	84
5.3.2	TiO ₂ based Materials.....	86
5.3.3	Electrospinning of Ti Containing Materials.....	87
5.3.4	5-Norbornene-2-methanol.....	88
5.3.5	Tetra(5-norbornene-2-methoxyl)titanate.....	89
5.3.6	Modification of a DCPD-HIPE with a Ti-source.....	90
5.3.7	Lithiumperoxide.....	92
5.3.8	Delithiation of LFP.....	92
	Abbreviations.....	93
	Bibliography.....	95

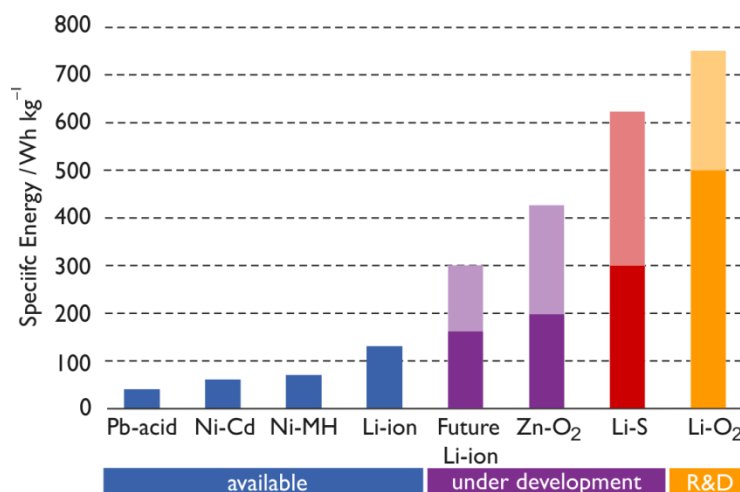
I Introduction

Society demands energy storage beyond the limits of current technology. Rising interest in electric vehicles has spurred the demand for electrochemical energy storage with energy and power per mass and volume, materials sustainability and cost beyond the possibilities of current technology. Ranging from small electronic devices to electric cars, batteries with long lifetimes, short charging times and high capacities are more and more important in everyday life. The extent of performance possible with current Li-ion technologies based on intercalation does not meet the demands of this steadily growing market.¹ Possible solutions could be the metal-air/O₂ battery or the Li-S battery.

I.1 The Li-O₂ Battery

Comparing specific energies is important when analysing and comparing battery technologies. Pure lithium metal appears to be an attractive anode material owing to its specific capacity of 3862 mAh g⁻¹. Sometimes this value is falsely translated into the theoretical energy density of Li-O₂ batteries by multiplying it with the thermodynamic voltage of 2.96 V to arrive at ~11 500 Wh kg⁻¹ (without taking O₂ into account).² Additionally it is important to differ between the formal(only Li₂O₂), the theoretical (Li₂O₂ plus a minimum of active material and current collector) and the achieved true (Li₂O₂ plus used electrode and current collector) capacity of a Li-O₂ cell.³ The theoretical energy density of a Li-O₂ battery is 3485 Wh kg⁻¹, which would double the energy density of Li-ion battery technologies.² In Figure 1, the specific energies in Wh per total battery weight are given for currently available battery systems. For technologies still under development, a possible range is given.¹

Figure 1: Specific energies of different battery types. For future technologies (violet to yellow coloured) a possible range for the specific energy is given; redrawn from Tarascon *et al.*¹



By rule of thumb, the difference between practice and theory is a factor of three. Typically the Li-S battery, however, deviates by a factor of seven. This factor of seven was also assumed for other 'beyond Li-ion systems'.¹ Recent more realistic estimations were made for materials with large volume changes.^{3,4}

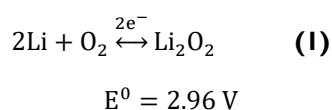
The significantly higher specific energy of metal-oxygen batteries results from a fundamentally different reaction mechanism during cycling. In contrast to intercalating/releasing Li in the electrode material, the current is generated by forming a new molecule that consists of the metal cation and the oxygen anion.² This fact arises new problems when calculating the achieved specific capacities of tested Li-O₂ cathode materials. These problems were discussed in a recent review by Mahne *et al.* and will be shortly summarised in the following.³ First, the term 'super-host-structure' has to be defined when discussing

different cathode materials; the cathode material consists of two main components, the electrode and the pore filling electrolyte. Second, the capacity has to be given per total electrode mass instead of only dividing the real capacity by the weight of active carbon. This significantly reduces the reached capacities, but leads to a better comparison to other tested cathode materials and also to intercalation based battery systems. In addition, linked to the second problem, in many publications cells are only cycled to a small fraction of their possible specific capacities. By only showing one discharge to 10 000 mAh g⁻¹ and then cycling with a limited capacity of 1000 mAh g⁻¹, the true performance strongly depends on the initial porosity of the cathode material. With set capacity limitation and porosities greater than 85% the resulting material does not reach the true specific capacity of the widely used intercalation material lithium iron phosphate (LFP).

In 1987, the first Li-O₂ battery was published by Semkow *et al.*⁵ It was a solid setup and operated at elevated temperatures of 650 – 800 °C. The first Li-O₂ operating at room temperature was proposed by Abraham *et al.* in 1996.⁶ He and co-workers wanted to study the lithium intercalation into graphite but formed Li₂O₂ instead due to some air leaks of the apparatus. Since approximately 10 years, research regarding metal-air batteries in general and Li-O₂ systems in particular, has significantly increased.⁷ Nowadays, four different types of Li-O₂ batteries are known: non-aqueous, aqueous, hybrid and all solid state cells.⁸ In the following the non-aqueous Li-O₂ will be discussed in more detail.

1.1.1 Reactions during Cycling of a Li-O₂ Battery

During cycling of a non-aqueous Li-O₂ battery, lithium peroxide is reversibly formed/decomposed in the pores of the cathode material during discharge/charge following Equation (1).

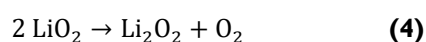
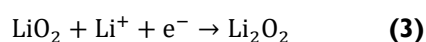
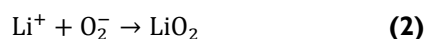


During discharge, at the anode Li is oxidised to the metal ion and dissolved into the electrolyte. At the cathode, oxygen is reduced and combines with Li-ions to form Li₂O₂, the discharge product. This process is termed oxygen reduction reaction (ORR). On charge, O₂ and Li⁺ are re-formed in the oxygen evolution reaction (OER). If no side reactions are happening, the ratio between e⁻ and reduced/oxidised oxygen is two. In a completely reversible cell reaction, no gases except O₂ must evolve during charging, no solid side products are formed and the number of oxygen molecules consumed equals the evolved oxygen.³ In practice, none of these conditions are met.

Oxygen Reduction Reaction (ORR)

The main product formed on ORR is Li₂O₂. Different mechanisms leading to that product have been proposed in literature, are summarised in Figure 2, and are discussed in the following.

In any case, the ORR starts with the one e⁻ reduction of O₂ to O₂⁻. Gaseous O₂ is dissolved in the electrolyte, which floods the porous electron conducting cathode host, is reduced to superoxide O₂⁻ and then binds to the Li⁺ to form LiO₂ (Equation (2)). Li₂O₂ is then either formed by a subsequent one e⁻ reduction (Equation (3)) or a disproportionation reaction (Equation (4)).



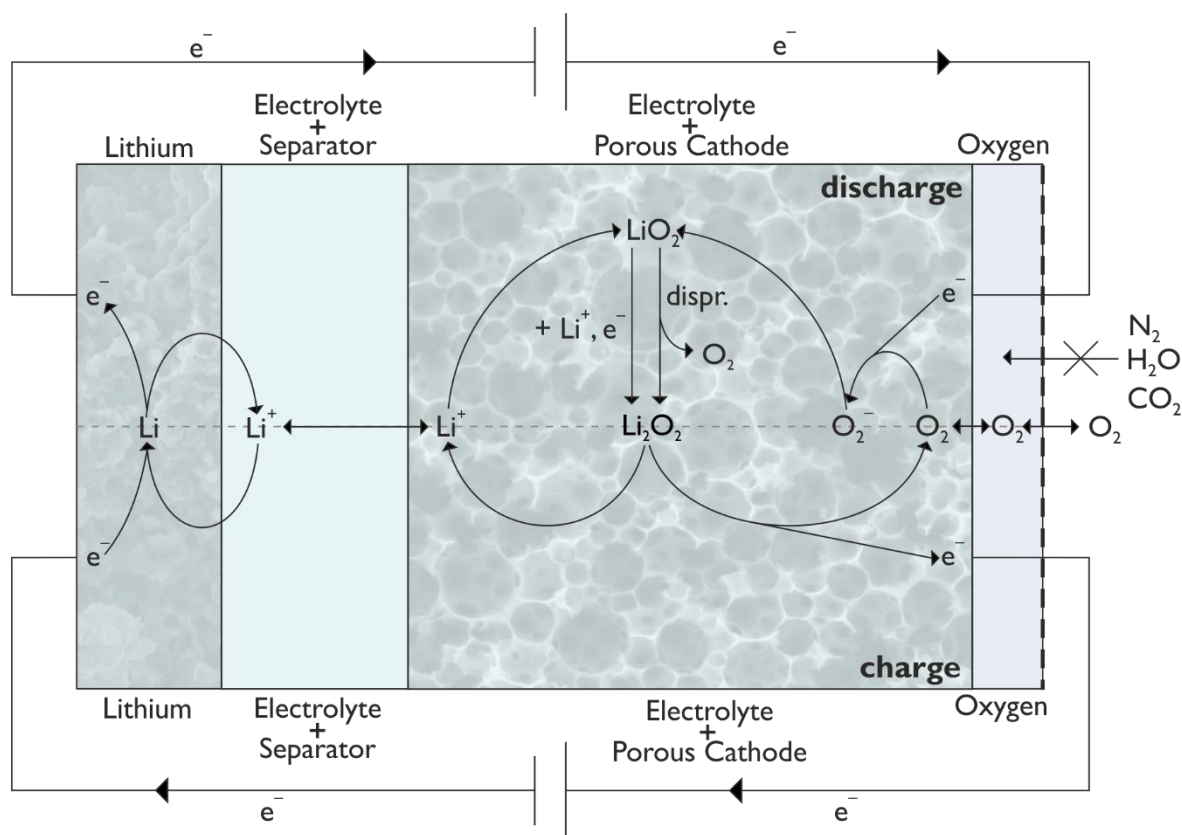
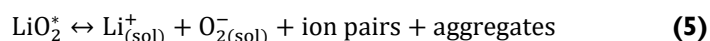


Figure 2: Schematic of a Li-O₂ cell with all cell elements (anode, separator + electrolyte, cathode, oxygen reservoir) and the occurring reactions on discharge (upper part) and charge (lower part).

Two mechanisms, a solution and a surface one, have been proposed on how these steps proceed and how they are governed. More recently a unified mechanism was proposed, where both mechanisms are limiting cases with the true mechanism being somewhere in between. Central to whether the one or the other mechanism dominates is the solubility of the superoxide intermediate along the equilibrium in Equation (5), where * corresponds to a surface species.⁹



The first mechanism is the so-called surface mechanism^{10,11}, having the equilibrium on the left side of the equation. Here, electrolytes with low donor numbers are used, leading to a low solubility of Li⁺, O₂⁻ and LiO₂ in the electrolyte. LiO₂ is adsorbed on the electrode surface and reacts to Li₂O₂ *via* reduction or disproportionation. The superoxide is barely mobile and the subsequently formed Li₂O₂ cannot agglomerate to bigger particles but forms a thin film on the cathode surface. When thicknesses of five to ten nm are reached, the film is too insulating for further electron transport and an early cell death occurs.^{11,12}

The second one is the solution mechanism,¹³ where the equilibrium in Equation (5) shifts to the right, superoxide species thus solvate and are mobile in the electrolyte. The solvation of ionic species in aprotic solvents is mostly determined by the solvation of the cation.⁹ This is determined by the Lewis basicity, which in turn may be expressed by the Gutmann donor number (DN). Anionic solvation is driven by Lewis acidity or the acceptor properties as expressed by the acceptor number (AN) and is typically much weaker than cation solvation.¹⁴ Widely used solvents range from nitriles and sulfones (DN=14-16) and glymes (DN=20-24) to amides (DN~26) and sulfoxides (DN~30).^{9,15} The solution mechanism can additionally be favoured by the use of Li⁺-coordinating salts¹⁶ like LiNO₃ or O₂⁻

solvating additives like water or alcohols.^{17,18} All parameters influencing the equilibrium given in Equation (5) are summarised in Figure 3.³

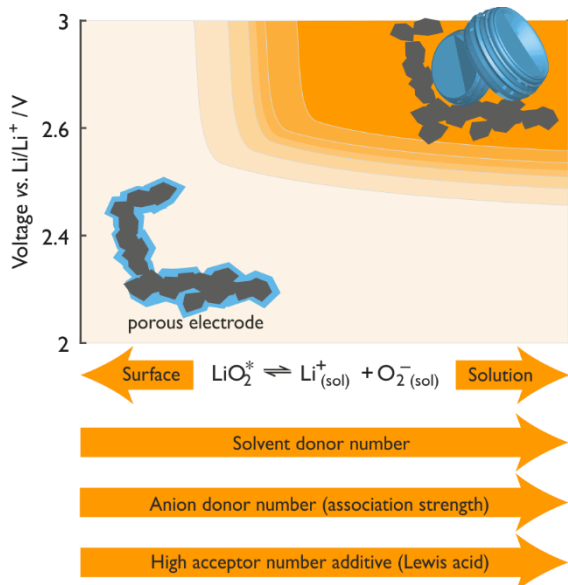


Figure 3: Summary of parameters responsible for surface and solution growth. While surface growth of Li_2O_2 leads to a thin layer on the cathode material, the solution mechanism forms larger particles. The solvents DN, strong Li^+ -solvating salts, additives with high Lewis acidity and low discharge currents can favour the solution mechanism; redrawn from Mahne *et al.*³

A typical drawback of high donor number solvents like dimethyl sulfoxide (DMSO) or dimethylformamide (DMF) is their instability regarding the Li anode.¹⁹ Similar problems occur with protic additives like water, which increase side product formation. Some redox mediators, like 2,5-di-tert-butyl-1,4-benzoquinone (DBBQ), also increase the solubility of discharge intermediates and favour the solution mechanism regardless of the used electrolyte. Additionally, LiO_2 is bound to the mediator and forms the less reactive LiDBBQO_2 , thus decreasing side reactions.²⁰

Oxygen Evolution Reaction (OER)

On charge, Li_2O_2 reacts back to Li^+ and O_2 , and has to overcome a major hurdle – its insulating character. Even five to ten nm thick layers of Li_2O_2 lead to early cell death due to the insulating character of the discharge product. The electronic and ionic conductivity of crystalline Li_2O_2 are in theory in the range of $10^{-19} \text{ S cm}^{-1}$.²¹ Only due to different defects like the presence of heteroatoms, an amorphous character of the material or lithium deficiency it is possible to reach conductivities high enough to allow charging.²² Some of those defects occur during discharge, but others, like lithium vacancies, are primarily formed during charge. Here, first LiO_2 is formed on the surface of the Li_2O_2 particles leading to $\text{Li}_{2-x}\text{O}_2$. This reaction is already possible at small overpotentials of approximately 0.3-0.4 V and kinetically favoured compared to direct Li_2O_2 decomposition.²³ If partly amorphous Li_2O_2 is formed during discharge, it is oxidised on charge before the, less conductive, crystalline one. This then can lead to Li_2O_2 particles losing contact to the electrode surface, if the oxidation takes place at the cathode/ Li_2O_2 and not the electrolyte/ Li_2O_2 interface.³

1.1.2 Problems of the Li- O_2 Battery

Although a number of ways have been shown that allow the Li- O_2 battery to reach high discharge capacities and to reversibly form Li_2O_2 for a number of cycles with limited capacity, many problems have yet to be overcome. Significant overpotentials during cycling, the use of O_2 instead of air, the stability of various battery components and linked to that the formed side products are the most important obstacles for replacing currently used Li-ion batteries. In the following problems not

investigated in the scope of this thesis will be shortly explained before the aspects dealt with in the last three years will be more thoroughly discussed.

Overpotential

High overpotentials, especially on charge, limit the energy efficiency of a Li-O₂ cell. The reversible thermodynamic potential of the O₂/Li₂O₂ couple is 2.96 V. In practice the ORR takes place at voltages in the range of 2.5-2.8 V, the OER at even higher overpotentials when the cell exceeds the 4 V mark.² With moderate overpotentials of ≥ 0.26 V on discharge and > 0.5 V on charge, the battery would only reach an overall efficiency of approximately 75%.⁸ The overpotential originates on the one hand from loosened contact of the discharge product on the cathode⁸ and on the other hand from side product formation.³ A possible solution for that problem is therefore to reduce side product formation and introduce an oxidation mediator like LiNO₃.²⁴ This electrolyte salt increases the solubility of superoxides during ORR and as NO₂⁻ acts as an oxidation catalyst on charge.

Additionally, different metal-oxides were investigated as catalysts. As powder, oxides like MnO₂ or TiO₂ do not have a high enough conductivity.²⁵ By direct growth of Co₃O₄ nanowires²⁶ or ϵ -MnO₂ nanostructures²⁷ on a nickel foam, binder and carbon free cathodes with suitable discharge capacities and less side product formation were built.²⁸ To overcome the insulating character of TiO₂, Kundu *et al.* prepared a Ti₄O₇ Magnéli phase with high conductivity and corrosion resistance. Although they were able to form Li₂O₂ on discharge and reduce the charge overpotential, the specific capacity was only in the range of Li-ion cells.²⁹

Composition of the used Gas

In literature, the term 'Li-air battery' is used frequently when actually pure O₂ or at least dried air are used. Up to now, the term 'Li-O₂ battery' is more appropriate and therefore used in this work. Main problems of using air are the presence of H₂O and CO₂.^{2,30} Both dissolve in the electrolyte and form LiOH and Li₂CO₃ as side products. This significantly reduces coulombic efficiency and cycle life of the battery. N₂ too is problematic if pure Li-metal is used as the anode, as LiN₃ is already formed at ambient conditions. The disadvantages of these gases could be overcome by incorporating an oxygen diffusion membrane³¹ or using an oxygen tank instead of air.

Anode Stability

In all calculations regarding the possible energy density of Li-O₂ batteries, Li metal is employed as the anode material. More stable alternatives would alleviate this problem, but significantly reduce energy density. However, when Li is exposed to the electrolyte, a solid electrolyte interface (SEI) is immediately formed. High capacities demand a small Li excess and thus a large fraction of Li being dissolved/deposited during cycling. The high utilisation of Li results in cracking of the SEI and dendrite formation.^{32,33} This continuously decomposes electrolyte, exposes Li to oxygen and increases all parasitic reactions.²

Electrolyte Stability

In the beginnings of Li-O₂ battery research, similar electrolytes as in Li-ion cells were used. However, carbonate based solvents like dimethyl carbonate are not chemically stable in the environment of a Li-O₂ battery, which will be explained in Chapter 1.2.2.³⁴ Therefore, a new electrolyte has to be found which has a high O₂ solubility, a high boiling point, is (electro-)chemically stable and stable towards oxygen and its reduced species.³⁵ A large variety of organic solvents including ether based electrolytes like

glymes and DMSO were tested in the last years regarding their suitability for Li-O₂ batteries. Main advantages of the glymes are their high oxidation potentials and low volatilities (especially triethylene glycol dimethyl ether and tetraethylene glycol dimethyl ether (TEGDME)). Although they were thought to be stable in the cell environment,³⁶ they are vulnerable to autoxidation and are therefore decomposed during cycling.³⁷ DMSO based electrolytes have very high donor numbers and are thus highly solubilising to ionic species. They are, however, vulnerable to oxidation to DMSO₂ and do not passivate Li metal by a stable SEI.³⁸⁻⁴⁰ Ionic liquids were also tested as possible electrolytes.⁴¹ Here the right choice of cation and anion is crucial for the reversible recharge ability of the Li-O₂ battery.^{42,43} In this work two different electrolytes, 0.1 M LiNO₃ in dimethylacetamide (DMAc) and 1 M LiClO₄ in TEGDME, were used.

1.2 Aspects Discussed in this Work

The main focus of this work was on the synthesis of a novel cathode material (marked in green Figure 4) for Li-O₂ cells, discussed in Chapter 3. The porous cathode, at which pore surface ORR and OER occur during cycling and where Li₂O₂ is stored, constitutes a critical component of the battery. One main problem of the cathode material is its stability in the cell environment and its potential promoting effect on electrolyte decomposition.⁴⁴ Directly connected to the stability of the cathode material are the formed products and by-products from both cathode material and electrolyte decomposition during cycling (marked in red in Figure 4). Increasing the stability of the electrode reduces the amount of formed side products. A tool to quantify the products and side products is necessary to characterise the different materials. Therefore, existing methods for the quantification of inorganic and organic carbonaceous side products as well as peroxides and superoxides were modified and combined, which is further explained in Chapter 2. The final Chapter 4 focuses on identifying and suppressing a major cause for the formation of side products during cycling, singlet oxygen (blue in Figure 4).

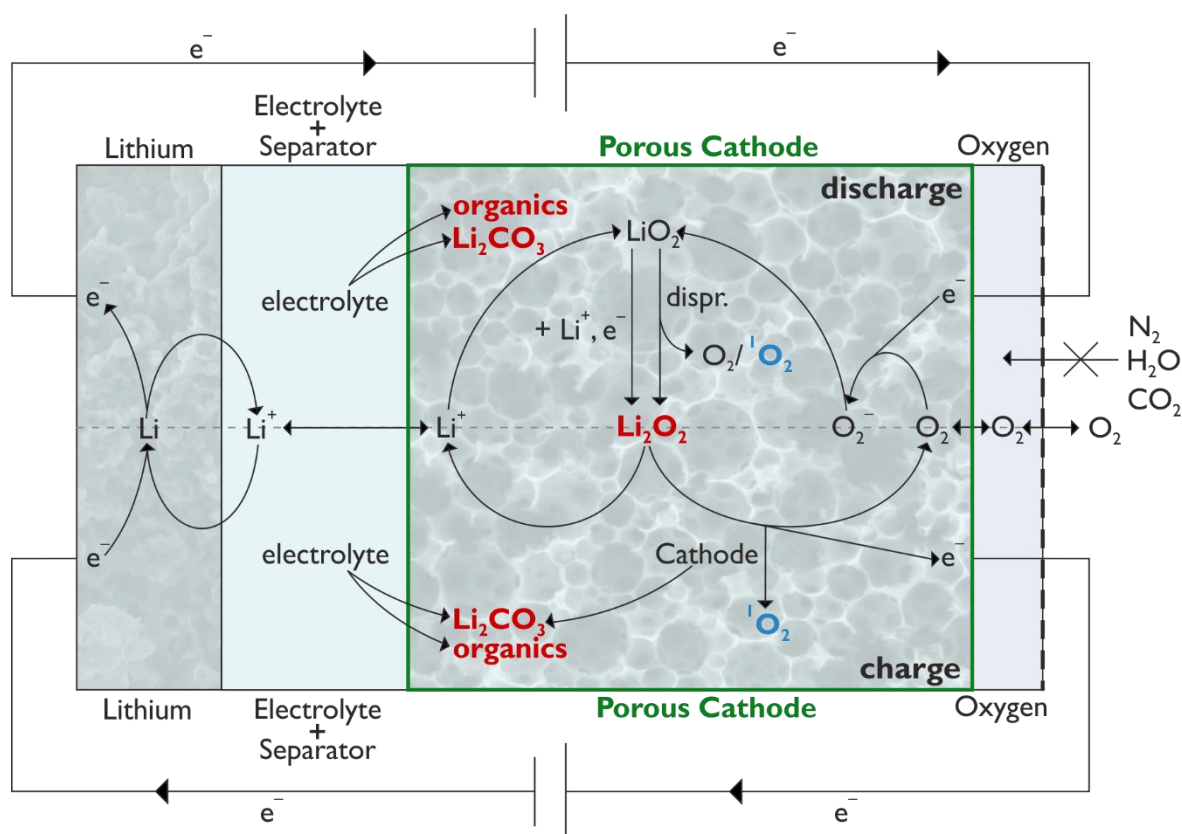


Figure 4: Schematic of a Li-O₂ cell with all cell elements (anode, separator + electrolyte, cathode, oxygen reservoir) and the occurring reactions on discharge (upper part) and charge (lower part). The main focus of the different chapters are coloured in blue (singlet oxygen formation), red (side product formation and the development of a quantifying method) and green (synthesis of a porous cathode material).

1.2.1 Cathode Materials

Requirements for as well as the preparation of different cathode materials was the topic of many reviews and publications over the last years.^{1,3,7,22,25,31,35,39,40,42,43} These requirements are:²

- **open porosity:** mesopores provide space to store the reaction products and macropores facilitate the gas transport to the active site

- **stability:** chemical stability against reduced oxygen species and products as well as electrochemical stability in the operating window
- **conductivity:** a conductive material is needed to partly balance the insulating character of Li_2O_2 and transport the e^- to the active site
- **low density:** light materials as electrodes are directly correlated to high theoretical specific capacities

A versatile and often used material fulfilling most of the requirements is porous carbon in various morphologies. Due to an easily changeable surface area and pore size, low cost, high conductivities and a low density, it was widely used in the metal- O_2 cell community. The main problem, however, is its instability against reactive oxygen species and its promoting effect on electrolyte decomposition. It was particularly shown that carbon is relatively, not yet entirely, stable on discharge and at charging voltages below 3.5 V, but decomposes more severely on charge above 3.5 V *vs.* Li/Li^+ . These instabilities do not seem to differ by changing the morphology from amorphous carbons to nanotubes or graphene but are more pronounced for hydrophilic carbon in comparison to hydrophobic carbon.^{44,45}

Materials without those drawbacks are for instance nanoporous gold or TiC nanoparticles.⁴⁰ Gold is too expensive, difficult to fabricate and has a high density that significantly diminishes the theoretical energy density. TiC, which is lighter and less expensive than nanoporous gold, was therefore investigated as a suitable cathode material. When cycling in DSMO or TEGDME based electrolytes, side product formation can be significantly reduced in contrast to porous carbon materials.⁴⁰ One reason for that is the formation of a thin conductive TiO_{2-x} layer formed on the TiC surface, which prevents further side product formation.⁴⁶ However, the specific capacity of cells cycled with TiC nanoparticles is only in the range of 350 to 500 $\text{mAh g}_{\text{TiC}}^{-1}$ and therefore approximately tenfold smaller than generally used porous carbon materials like Ketjenblack (KB, see page 36).⁴⁰ This is, however, still not the true capacity of the electrode, for which the total weight of porous cathode and discharge product needs to be taken into account. Governing factors for the true capacity are the initial porosity of the porous electrode, the degree of pore filling and the density of the porous material.³ The limiting case for true capacity is full pore filling, which is shown in Figure 5 as a function of initial porosity for C and TiC cathodes. High porosity becomes thus even more important when going from C to the much denser TiC. Pure Li_2O_2 has a capacity of 1168 mAh g^{-1} .

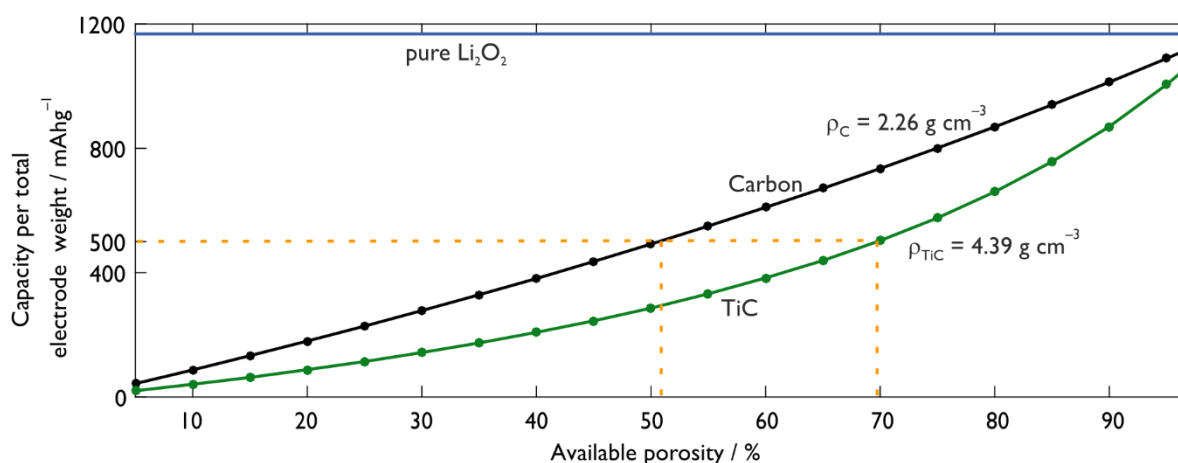


Figure 5: Maximum true capacity per total electrode weight including active material as a function of initial electrode porosity for C and TiC cathodes.

An exemplary line is drawn at a capacity of 500 mAh g^{-1} to emphasise the correlation between weight and available porosity. Due to the lower density of carbon, only a porosity of approximately 50% is necessary to reach the wanted capacity, while a porosity of about 70% is needed for the TiC material.

1.2.2 Side Product Formation

For true reversibility of a Li-O₂ battery, a few requirements regarding oxygen consumption/evolution, electron consumption and so on have to be fulfilled.³ For Li₂O₂ as the only discharge product, the moles of e⁻ have to be twice the moles of discharge product and consume oxygen and the ratio of O₂/Li₂O₂ has to be one. For all types of Li-O₂ batteries (having pure LiO₂ or Li₂O₂ or mixtures of both as discharge products) it is further important that no gases other than O₂ evolve during cycling and no other solid products are formed. Additionally, all electrons have to be used for the ORR and the OER reaction and, if discharge and charge capacity are the same, consumed and evolved moles of oxygen have to be the same. Though, these requirements cannot be fulfilled up to date due to parasitic chemistry of the electrolyte and cathode material with reactive oxygen species or lithium.

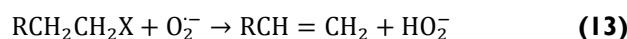
On discharge, the number of electrons per consumed O₂ molecule is normally close to the theoretical value of 2 (2.03 ± 0.2). This may indicate that side product formation on discharge is of chemical and not electrochemical nature.⁴⁷ Regardless of the state of discharge/charge, the electrolyte decomposes due to oxygen species; through nucleophilic substitution, proton or H-abstraction, O₂⁻ and O₂²⁻ and O₂ attack the electrolyte. Possible decomposition reactions are summarised in Table 1. Many of the given reactions are not likely due to high activation energies above 100 kJ mol⁻¹. Carbonate based electrolytes are especially vulnerable regarding the nucleophilic attack of oxygen species (Equation (6)) and then form a [solvent-O₂]⁻ complex, which decomposes exergonic.²² If a proton source is present, the even more reactive species HOO[•], HOO⁻ and HO[•] are formed and react similar to the reactive oxygen.³

Table 1: Possible reactions of electrolytes with molecular oxygen and reduced oxygen species. R' is used for organic moieties with polymerisable heteroatoms like N or S.³

reactant	type of reaction	reaction	E ^{act} / kJ mol ⁻¹	ref.
O ₂ ⁻	nucleophilic substitution	ROR' + O ₂ ⁻ → RO ⁻ + ROO [•] (6)	121–144 ^a , 105 ^b , 65–95 ^c	48–51
	H-atom abstraction	RH + O ₂ ⁻ → R [•] + HOO ⁻ (7)	129–180 ^d , 191 ^e	49,50,52,53
	H ⁺ abstraction	RH + O ₂ ⁻ → R ⁻ + HOO [•] (8)	pK _a > 30 stable ^f	54
Li ₂ O ₂	nucleophilic substitution	ROR' + Li ₂ O ₂ → RO ⁻ Li ⁺ + R'OO ⁻ Li ⁺ (9)	134–192 ^a	55
	H-atom abstraction	RH + Li ₂ O ₂ → R [•] + [Li ₂ O ₂ – H [•]] (10)	96–112 ^a	55
	H ⁺ abstraction	RH + Li ₂ O ₂ → R ⁻ Li ⁺ + HOO ⁻ Li ⁺ (11)	116–311 ^a	51,55
O ₂	H-atom abstraction	RH + O ₂ → R [•] + HOO [•] (12)	163–183 ^g , 138–161 ^h	49

^adimethoxyethane (DME); ^bacetonitrile; ^ccarbonate and lactones; ^dfree DME; ^ethe DME₂-Li⁺ complex; ^fexamples for pK_a < 30: -CH₂-CF₂-, polyvinylidene difluoride (PVDF), aliphatic dinitriles, alkyl imides. pK_a > 30: acetonitrile, DMSO, N-alkyl amides and lactams, aliphatic ethers; ^gthe lower value for free DME, the higher one for the DME₂-Li⁺ complex; ^hlactams and amides.

Ether-, sulfone- or amide- based electrolytes are more stable against nucleophilic attacks, but contain polarisable bonds due to the heteroatoms.⁵⁶ In the presence of lithium ions, thermodynamically favoured reactions are possible with reactive oxygen species again leading to electrolyte decomposition, as displayed in Equation (13).



(Poly-)ethers, although they are generally more inert solvents, are attacked on the α- or β-H atom when Li⁺ is present (see Figure 6). On the Li anode, ether based electrolytes like TEGDME readily decompose resulting in a mixture of organic decomposition products.^{56,57}



Figure 6: Glyme decomposition due to reaction with Li₂O₂.

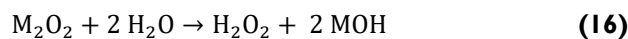
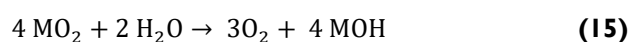
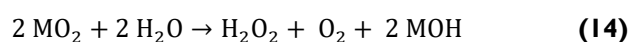
Up to now, the high amount of side products formed during cycling is one of the major drawbacks of the Li-O₂ battery. It is closely linked to electrolyte and cathode stability – the latter being one of the main topics in this work. Although this technology has been investigated for many years, the exact mechanisms leading to various side products and to Li₂O₂ have not been completely understood. Minimising the amount of side products by choosing electrochemically and chemically stable electrolytes and cathodes have to be one of the main goals leading to a commercially available Li-O₂ battery. One main aspect helping to reach this goal is to identify and quantify the side products formed during cycling.

2 Cathode Analysis

The importance of minimising side products formation in the area of metal-O₂ batteries was already summarised in the introduction and is a key aspect investigated in literature.^{2,3,8,17,18,22,25,29,35,56,58–60} To be able to influence the amount of side products formed during cycling, in a first step information about the amount and the kind of formed parasitic products has to be gained. Methods used in literature mainly focus on the latter aspect and use FT-IR, NMR, XPS or XRD analysis.^{37,61,62} In the course of this work, different already published techniques were combined, pitfalls of these methods were identified and a way to quantify total superoxide/peroxide as well as carbonaceous compounds of metal-O₂ and Li-ion batteries was found. The method was published in ACS Energy Letters⁶³ and is described in the following combined with a few unpublished results. Shortly summarised, all materials formed during cycling are extracted with aqueous solutions and digested into H₂O₂, O₂ and CO₂, which were quantified using mass spectrometry (MS) and UV-Vis spectrometry.

2.1 Metal (per-)oxides

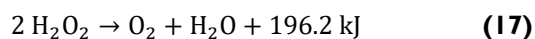
Additional to the quantification of parasitic products, it is also important to gain information about the amount of (su-)peroxides reversibly formed during cycling. Alkine superoxides and peroxides (M = Li, Na, K, Rb, Cs) dissolve according to⁶⁴



Recently, Wang *et al.* have shown that NaO₂ and KO₂ hydrolyse according to Equation (14) whereas LiO₂ follows Equation (15), which they could rationalise based on the reaction free energies.⁵⁸ LiO₂ can thus not be quantified *via* the H₂O₂ formed.⁵⁸ Later on, the case with MO₂/M₂O₂ mixtures will be discussed (see page 15ff). Literature describes a range of methods to determine H₂O₂ including redox titration with I⁻, MnO₄⁻ and Ce⁴⁺ or photometric detection of Ti⁴⁺ or Co²⁺ peroxo complexes.⁶⁵

Decomposition of H₂O₂

A common pitfall is, however, that H₂O₂ is prone to decompose following⁶⁴



The reaction does not occur at ambient conditions, as the forming the intermediates is highly endothermic (211 kJ). Different catalysts like silver, gold, MnO₂, Fe(III) salts can favour this reaction. In the context of metal-O₂ batteries, H₂O₂ has been quantified by 1) iodometric titration after immersing the electrode in H₂O and neutralizing with HCl⁶² or 2) measuring the absorbance of the [Ti(O₂)OH]⁺ complex after immersing the electrode in acidic TiOSO₄ solution.^{64,66–68} To test whether and how much these methods could underestimate the H₂O₂ by loss into the gas phase, we measured the evolved O₂ by MS during the immersion steps, Figure 7. The setup consisted of a hermetically sealed glass vial equipped with a stirring bar and a lid with septum and tubing for purge gas, Figure 81 on page 82. The gas space was continuously purged into a MS for gas analysis. To resemble major electrode types we tested next to pure Li₂O₂ also mechanical mixtures of Li₂O₂ with carbon black and a mixture with additional α-MnO₂.

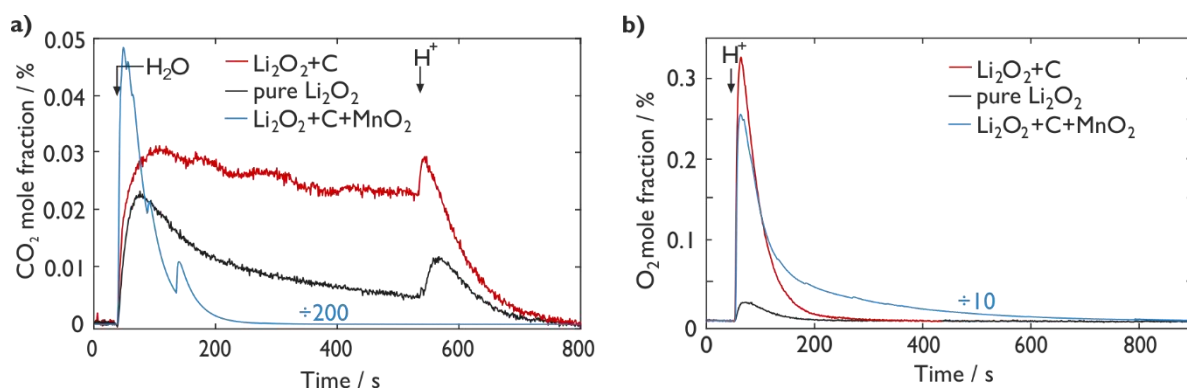


Figure 7: Oxygen loss into the gas phase upon sample preparation for peroxide/superoxide detection by titration (a) or photometry (b). The samples are pure Li_2O_2 and mechanical mixtures of Li_2O_2 with SuperP carbon (1:1) and Li_2O_2 with SuperP carbon and $\alpha\text{-MnO}_2$ (1:0.6:0.4), which mimic discharge Li- O_2 cathodes without and with catalyst. a) Iodometric titration involves adding water and then acid; b) Photometry involves adding TiOSO_4 in 0.1 M H_2SO_4 solution.

Turning first to the preparation for titration, immersing pure Li_2O_2 in H_2O evolves O_2 at somewhat fading rate after an initial peak, Figure 7a. Once acid is added O_2 evolution rises again to fade thereafter quickly to the base line. With the $\text{Li}_2\text{O}_2/\text{C}$ mixture, O_2 evolves at a higher, nearly constant rate and also drops once acid is added. The O_2 amounts equate to ~ 3 and 8% , respectively, of the H_2O_2 . With the $\text{Li}_2\text{O}_2/\text{C}/\text{MnO}_2$ mixture, O_2 evolves at initially ~ 400 times the previous rate to quantitatively evolve all O_2 within ~ 300 s. Turning to the preparation for Ti^{4+} photometry, Figure 7b, immersing pure Li_2O_2 , $\text{Li}_2\text{O}_2/\text{C}$ or $\text{Li}_2\text{O}_2/\text{C}/\text{MnO}_2$ mixtures leads to O_2 evolution in the same order as before. The O_2 amounts equate to 0.3 , 7 and 55% of the total peroxide, respectively. Fast catalytic decomposition of H_2O_2 by transition metal oxides is in accord with its use to probe catalytic activity⁶⁹ and renders measuring H_2O_2 by titration or photometry alone impracticable for electrodes with catalysts. The results also show that significant amounts of H_2O_2 can be lost with only marginally catalyzing C surfaces and even with pure Li_2O_2 . Similarly, immersing NaO_2 or KO_2 in water or acid releases more O_2 than commensurate with Equation (14), which indicates significant decomposition of the formed H_2O_2 , Table 2.

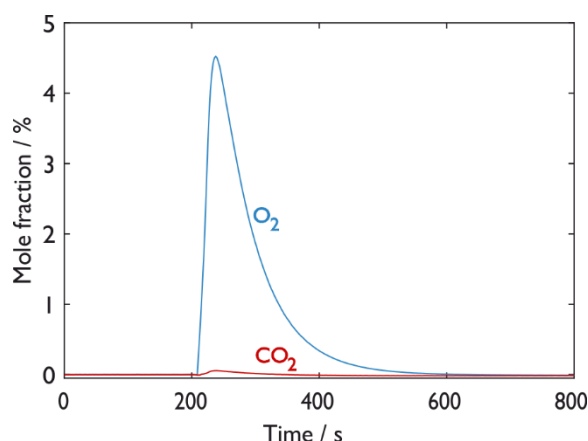
Table 2: Amount of released O_2 with respect to the NaO_2 or KO_2 amount when immersed in water or acid. Note that for every mol O_2 two mol H_2O_2 are decomposed (Equation 17). For NaO_2 , NaO_2 cathodes discharged in 0.5 M NaOTf in diglyme containing 40 ppm H_2O were used. For KO_2 commercial material was used. The total NaO_2 or KO_2 amount was determined by combining MS and UV-Vis measurements.

	O_2/NaO_2	O_2/KO_2
ideal	0.5	0.5
immersed in H_2O	0.554	0.523
immersed in 0.1 M H_2SO_4	0.520	0.528
immersed in 1.0 M H_2SO_4	0.525	0.557

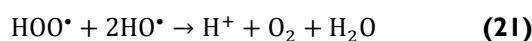
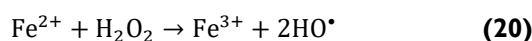
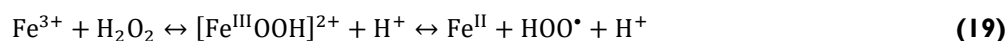
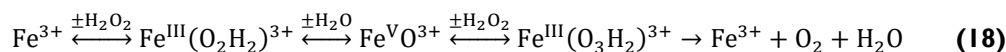
2.1.1 Oxygen Evolution with Iron(III) Salts

Measuring O_2 from peroxide/superoxide by evolving it into the gas phase appears an attractive option given the described significant O_2 evolution. Prerequisite is to evolve O_2 quantitatively and to avoid reactive O_2 species, which could decompose organics into CO_2 . The latter would not allow distinguishing CO_2 from organics and inorganics as intended and underestimate the peroxide/superoxide amount. Although effective in decomposing H_2O_2 , transition metal oxides do form reactive species and prematurely decompose organics, Figure 8.

Figure 8: CO₂ evolution indicates reactive species upon expelling O₂ from H₂O₂. The H₂O₂ source was Li₂O₂ and Li acetate was used as organic probe molecule. A mixture of Li₂O₂/CH₃COOLi (90/10 wt%) was mixed with an equal amount of α-MnO₂ nanowires and immersed in 1 M H₂SO₄ solution.



While O₂ evolved quantitatively, the CO₂ amount corresponds to ~10% of the CH₃COOLi present in the mixture. H₂O₂ may, however, also catalytically be decomposed by Fe³⁺ for which either the Kremer Stein mechanism (Equation (18)) or the Haber-Weiss mechanism (Equations (19)-(21)) were proposed.^{64,70}



While in both cases one O₂ is formed per two H₂O₂ molecules, the Kremer Stein mechanism decomposes H₂O₂ *via* a Fe³⁺/Fe⁵⁺ redox couple while the Haber-Weiss mechanism uses the Fe³⁺/Fe²⁺ redox couple. In the latter case, radicals are formed which can decompose organic side products present in the electrode. In literature, the Kremer Stein mechanism is proposed to be more likely.⁶⁴ The quantitative, catalytic decomposition of Li₂O₂ was analysed by testing FeCl₃ solutions with various concentrations (*cf.* Table 3). In all cases, the salt was dissolved in distilled water and 500 μL were added to the peroxide in the MS-setup. The obtained oxygen yield was in all cases close to 100% and was not influenced by the concentration of Fe³⁺.

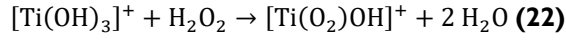
Table 3: Oxygen yields for various Fe³⁺ to Li₂O₂ concentrations.

Fe ³⁺ concentration	Fe ³⁺ to Li ₂ O ₂ ratio	O ₂ yield
0.05 M	0.2/1	96%
0.1 M	0.6/1	100%
0.5 M	2.5/1	99%
1 M	4/1	101%

Additionally, the quantitative decomposition of different H₂O₂ amounts was also analysed using a 0.1 M FeCl₃ solution. In a range of 0.5 to 5×10⁻⁵ mol Li₂O₂ no significant deviation between the measured and expected amounts of O₂ could be identified (see Figure 83 on page 83). Again, lithium acetate (LiAc) was added as a probe for reactive species. The sample evolved CO₂ in a similar amount as when MnO₂ was added, indicating a pathway with reactive species (Equations (19)-(21)). This leads to the conclusion that quantifying superoxide and peroxide by evolving them as O₂ is problematic. That way, reactive oxygen species form, which causes O₂ and organic carbonates to be underestimated.

2.1.2 Peroxide Quantification with Ti(IV)-oxysulfate

Complexation of H₂O₂ is a viable alternative; here, no decomposition occurs and no radicals are formed. The titanium-oxysulfate complex is a very sensitive probe for H₂O₂, as the former colourless molecules form an orange complex (Equation (22)).



This complex can be quantified *via* UV-Vis spectrometry using the calibration curve given in the method section (Figure 84 on page 84). Calibrating UV-Vis absorbance with H_2O_2 is prone to yield a curve that does not pass through zero, i.e. due to loss of H_2O_2 .⁶⁷ To obtain the true H_2O_2 concentration, we thus started from high purity Li_2O_2 and accounted for any H_2O_2 loss by measuring evolved O_2 .

2.1.3 Quantification of pure Superoxides and Peroxides

Superoxide and peroxide may thus best be quantified by combining photometry of the $[\text{Ti}(\text{O}_2)\text{OH}]^+$ complex and MS measurement of the O_2 evolved during sample preparation. First the case is considered where the product is either Li_2O_2 , Na_2O_2 , NaO_2 or KO_2 but no mixtures are formed.

When LiO_2 is measured, according to Equation (15) no H_2O_2 is formed. Therefore then, the total moles n can be obtained *via*

$$n_{\text{LiO}_2} = \frac{3}{4} n_{\text{O}_2} \quad (23)$$

When M_2O_2 is measured, acidifying the sample will convert the peroxide according to Equation (16) while part of the H_2O_2 will decompose into H_2O and O_2 according to Equation (17). Thus any one mole O_2 evolved corresponds to 2 moles M_2O_2 , which are not any more present as H_2O_2 and therefore not captured by UV-Vis. One mole of H_2O_2 detected as $[\text{Ti}(\text{O}_2)\text{OH}]^+$ by UV-Vis correspond to one mole of M_2O_2 . The moles of H_2O_2 and O_2 per mol of M_2O_2 as a function of the H_2O_2 loss into the gas phase are plotted in Figure 9.

With x being the fraction of H_2O_2 lost, the moles n of H_2O_2 and O_2 are

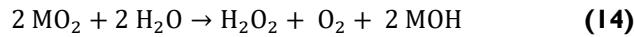
$$n_{\text{H}_2\text{O}_2} = n_{\text{M}_2\text{O}_2} - x \cdot n_{\text{M}_2\text{O}_2} \quad (24)$$

$$n_{\text{O}_2} = 0.5x \cdot n_{\text{M}_2\text{O}_2} \quad (25)$$

Thus moles of Li_2O_2 are

$$n_{\text{M}_2\text{O}_2} = n_{\text{H}_2\text{O}_2} + 2 \cdot n_{\text{O}_2} \quad (26)$$

When NaO_2 or KO_2 is measured, acidifying the sample will convert the MO_2 according to



while again part of the H_2O_2 will decompose into H_2O and O_2 according to Equation (17). With x being the fraction of H_2O_2 lost, the moles of H_2O_2 and O_2 are

$$n_{\text{H}_2\text{O}_2} = 0.5 \cdot n_{\text{MO}_2} - 0.5x \cdot n_{\text{MO}_2} \quad (27)$$

$$n_{\text{O}_2} = 0.5 \cdot n_{\text{MO}_2} + 0.25x \cdot n_{\text{MO}_2} \quad (28)$$

Thus the moles of MO_2 are

$$n_{\text{MO}_2} = \frac{4}{3} \left(n_{\text{O}_2} + \frac{1}{2} \cdot n_{\text{H}_2\text{O}_2} \right) \quad (29)$$

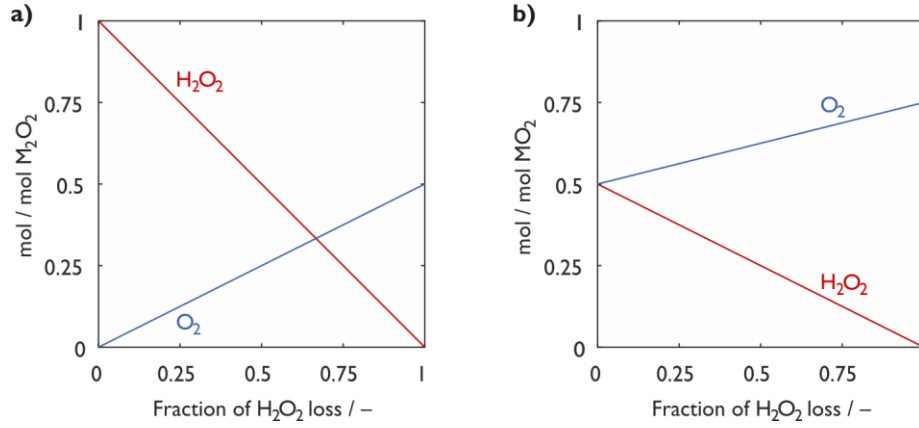


Figure 9: Amount of O₂ in the gas phase and H₂O₂ in the solution as a function of the fraction of theoretical amount of H₂O₂ lost into the gas phase; a) for M₂O₂ as given in Equation (24) and (25); b) for NaO₂ or KO₂ as given in Equations (27) and (28).

Quantification of Superoxide/Peroxide Mixtures

In some cases it was shown that Li-O₂ and Na-O₂ cells can yield mixtures of superoxide and peroxide as discharge product.^{58,67,68,71-73} When mixtures are to be expected, determining the individual amounts requires additionally to measure the moles n of Li⁺ or Na⁺. Then, two cases have to be distinguished.

LiO₂ decomposes without formation of H₂O₂ while Li₂O₂ forms H₂O₂. Since both the fraction x of H₂O₂ being lost and the Li₂O₂-to-LiO₂ ratio are unknowns, n_{Li^+} needs to be obtained as a third measure next to $n_{\text{H}_2\text{O}_2}$ and n_{O_2} . According to Equations (15)-(17), these measures are connected to $n_{\text{Li}_2\text{O}_2}$ and n_{LiO_2} via

$$n_{\text{H}_2\text{O}_2} = n_{\text{Li}_2\text{O}_2} - x \cdot n_{\text{Li}_2\text{O}_2} \quad (30)$$

$$n_{\text{O}_2} = 0.5x \cdot n_{\text{Li}_2\text{O}_2} + \frac{4}{3} \cdot n_{\text{LiO}_2} \quad (31)$$

$$n_{\text{Li}^+} = 2 n_{\text{Li}_2\text{O}_2} + n_{\text{LiO}_2} \quad (32)$$

These quantities are plotted as a function of LiO₂ mole fraction in Figure 10 for various values of H₂O₂ loss x . The moles of Li₂O₂ and LiO₂ are then obtained via

$$n_{\text{Li}_2\text{O}_2} = \frac{6}{13} \left(\frac{4}{3} n_{\text{Li}^+} - \frac{1}{2} n_{\text{H}_2\text{O}_2} - n_{\text{O}_2} \right) \quad (33)$$

$$n_{\text{LiO}_2} = n_{\text{Li}^+} - 2n_{\text{Li}_2\text{O}_2} \quad (34)$$

For sodium batteries, H₂O₂ is formed when NaO₂ and Na₂O₂ are decomposed. Since both the fraction x of H₂O₂ being lost and the Na₂O₂-to-NaO₂ ratio are unknowns, n_{Na^+} needs to be obtained as a third measure next to $n_{\text{H}_2\text{O}_2}$ and n_{O_2} . According to Equations (14), (16) and (17) these measures are connected to $n_{\text{Na}_2\text{O}_2}$ and n_{NaO_2} via

$$n_{\text{H}_2\text{O}_2} = n_{\text{Na}_2\text{O}_2} + \frac{1}{2} \cdot n_{\text{NaO}_2} - x \cdot n_{\text{Na}_2\text{O}_2} + \frac{x}{2} \cdot n_{\text{NaO}_2} \quad (35)$$

$$n_{\text{O}_2} = \frac{x}{2} \cdot n_{\text{Na}_2\text{O}_2} + \frac{1}{2} \cdot n_{\text{NaO}_2} + \frac{x}{4} \cdot n_{\text{NaO}_2} \quad (36)$$

$$n_{\text{Na}^+} = 2 n_{\text{Na}_2\text{O}_2} + n_{\text{NaO}_2} \quad (37)$$

These quantities are plotted as a function of LiO₂ mole fraction in Figure 10b for various values of H₂O₂ loss x . The moles of Na₂O₂ and NaO₂ are then obtained via

$$n_{\text{Na}_2\text{O}_2} = \frac{3}{4} n_{\text{Na}^+} - \frac{1}{2} n_{\text{H}_2\text{O}_2} - n_{\text{O}_2} \quad (38)$$

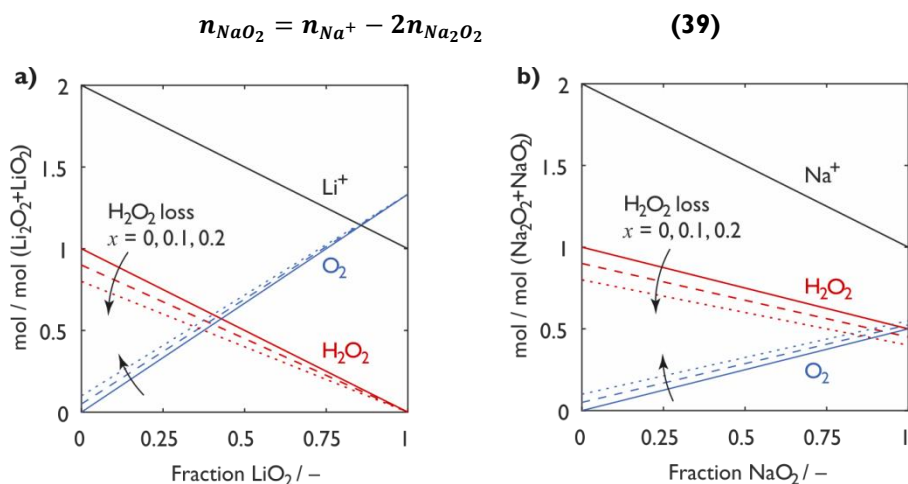
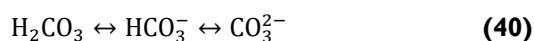


Figure 10: Analysis of mixtures of MO₂ and M₂O₂ (M = Li or Na). Amount of O₂ in the gas phase and H₂O₂ and M⁺ in the solution as a function of the mole fraction of superoxide in the mixture. In either case the effect of a H₂O₂ loss of 0, 10, 20% (i.e., x = 0, 0.1, 0.2) into the gas phase is examined. a) Analysis of LiO₂/Li₂O₂ mixtures as given in Equations (30)-(32); b) Analysis of NaO₂/Na₂O₂ mixtures as given in Equations (35)-(38).

2.2 Quantification of Carbonaceous Compounds

Main side products formed during cycling of a metal-O₂ battery or during the formation of solid electrode interphase of a metal-ion cell are M₂CO₃, in the following called inorganic carbonates or inorganic CO₂ and organic carbonates/carboxylates, in the following termed organic carbonates or organic CO₂. Inorganic carbonates decompose readily aqueous solutions according to following equilibrium:



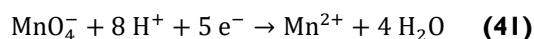
If the solution is slightly acidic (pH < 5), the equilibrium is on the right hand side, CO₂ evolves and can be quantified *via* MS analysis (calibration curve see Figure 82 on page 83).

2.2.1 Quantification of Organic Carbonates/Carboxylates

To decompose organic carbonates to CO₂, which then can be measured using MS, strong enough oxidation agents are necessary.

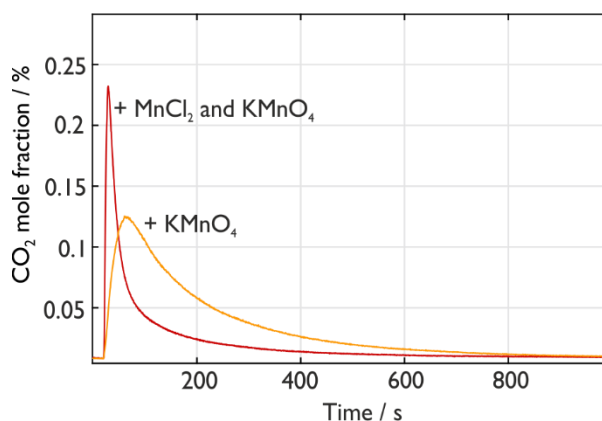
Potassium Permanganate (KMnO₄) as Oxidation Agent

KMnO₄ is a highly reactive oxidation agent and is known to oxidise Fe²⁺, oxalic acid, sulphurous acid or H₂O₂.⁶⁴ In acidic solutions Mn(VII) is reduced to Mn(II)



Starting rather slowly, the reaction accelerates itself with increasing amount of Mn²⁺ in the solution. First tests were performed by adding 0.5 M KMnO₄ in 2 M H₃PO₄ to a known amount of lithium formate (LiFo), Figure 11 (yellow curve). By adding a Mn²⁺ salt, namely MnCl₂, beforehand, the decomposition of LiFo could be significantly accelerated (red curve).

Figure 11: CO₂ evolution after addition of 500 μL 0.5 M KMnO₄ in 2 M H₃PO₄ (yellow curve) or MnCl₂ and 0.5 M KMnO₄ in 2 M H₃PO₄ (red curve) to a known amount of lithium formate (LiFo).



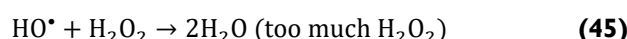
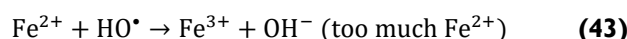
As a next step, carboxylates containing more carbon atoms (acetic acid or sodium acetate) were tested. Here, it was only possible to decompose the acid groups to CO₂ but not the connected carbon atoms. Therefore, KMnO₄ is a sufficient oxidising agent for very small organic side products, but not the method of choice to gain information about the total organic carbon content.

Fenton's Reaction

Another possibility to decompose organic side products is the Fenton's reaction. Highly reactive •OH radicals are formed *via* Equation (42), which are used to decompose organics into CO₂.⁶⁴



Many requirements have to be met to quantitatively decompose organic compounds with the formed •OH. A slight acidic environment, which a pH of approximately 3, provides the best conditions for this reaction.⁷⁴ More acidic solutions significantly reduce the reactivity of the Fenton's reaction, while less acidic ones cannot stabilise the Fe²⁺ salt, which then quickly oxidises to Fe³⁺. Additionally, the right ratio of Fe²⁺ ions to H₂O₂ has to be used. Ideally, first Fe²⁺ is added to the solution before an excess of H₂O₂ is added dropwise. Wrong ratios lead to various side reactions; all diminishing the quantification of organics (Equations (43)-(45)).^{64,75}



2.2.2 Classification in Inorganic and Organic CO₂

In all battery types, inorganic CO₂ is evolved by acid treatment of M₂CO₃. In metal-O₂ batteries, main organic carbonates are formate and acetate based metal-salts solely decomposed by the Fenton's reagent. In the SEI or the SPI of metal-ion cells, also larger organics like alkylcarbonates (ROCO₂M) are present. These molecules evolve CO₂ in two steps as exemplary depicted in Figure 12 for a sodium hexylcarbonate. By adding an acidic solution used for the decomposition of M₂CO₃, already one CO₂ per present alkylcarbonate is evolved and therefore in the following counted as inorganic CO₂. All carbon atoms present in the alkyl chain are subsequently decomposed by the Fenton's reagent and evolved as organic CO₂ whereas one CO₂ evolves per present carbon atom.

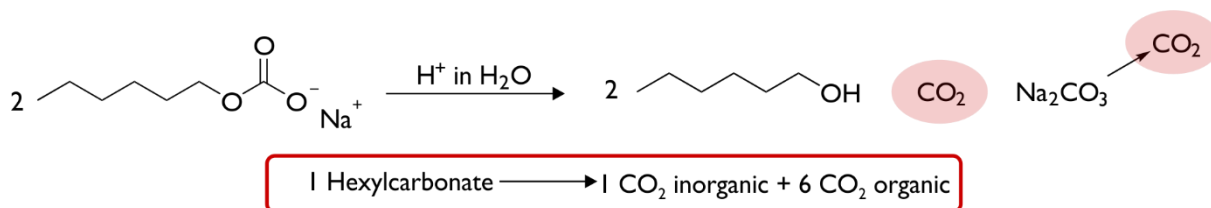


Figure 12: Quantification mechanism of alkylcarbonates using hexylcarbonate as an example. Addition of acid leads to the evolution of 1 CO_2 per alkylcarbonate counting as inorganic CO_2 . CO_2 depending on the chain length of the alkyl group evolves as organic CO_2 .

Table 4 compares expected and evolved moles of CO_2 for a range of compounds including Li_2CO_3 , Li acetate and different Li alkylcarbonates. In all cases the values match the expected values within 3% and confirm the reagents to expel the compounds selectively and quantitatively.

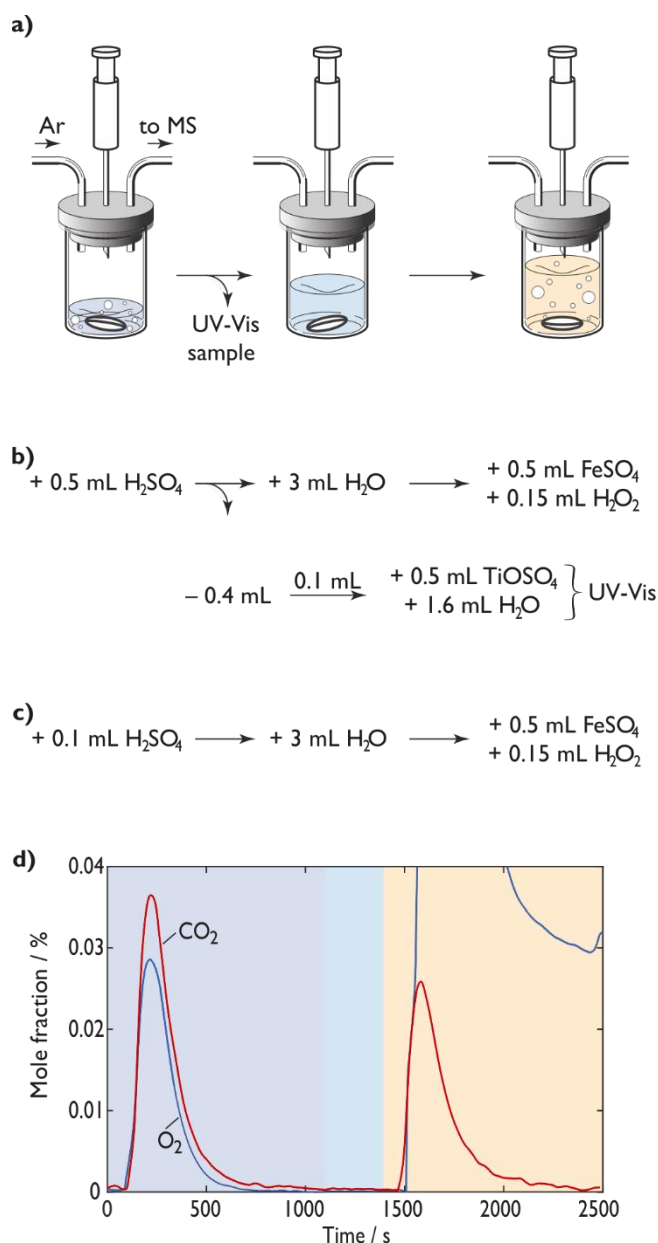
Table 4: Expected and measured moles of CO_2 evolved per mol of Li_2CO_3 , Li acetate and Li alkylcarbonates. Inorganic refers to CO_2 evolved from acid treatment, organic to CO_2 evolved from Fenton's reagent.

compound	expected		found	
	inorganic	organic	inorganic	organic
Li_2CO_3	1	-	1 ± 0.03	-
CH_3COOLi	-	2	-	2 ± 0.01
$\text{CH}_3\text{OCO}_2\text{Li}$	1	1	1 ± 0.02	1 ± 0.02
$\text{CH}_3(\text{CH}_2)_3\text{OCO}_2\text{Li}$	1	4	1 ± 0.02	4 ± 0.04

2.3 Whole Setup

All obtained information about quantification methods of superoxides/peroxides and carbonates (inorganic and organic) have to be combined to result in one quantification procedure. This optimised procedure is depicted in Figure 13 and can be used for sample sizes of several mg, which are typically used in coin cells or Swagelok® type cells. The procedure for metal- O_2 electrodes is summarized in Figure 13b, the procedure for all other electrodes in Figure 13c. The first involves as first step acidifying the sample with 1 M H_2SO_4 upon which CO_2 evolves from M_2CO_3 . The strongly acidic pH prevents excessive O_2 evolution from H_2O_2 . To quantify the dissolved peroxide, after CO_2 and O_2 evolution have ceased, part of the solution is removed and mixed with TiOSO_4 solution and analysed by UV-Vis. The remaining solution in the MS setup is then diluted with H_2O to reach the optimum pH of 3. Fenton's reaction is then initiated by adding FeSO_4 in 0.1 M H_2SO_4 and then, over the course of several minutes, H_2O_2 in 0.1 M H_2SO_4 under vigorous stirring. For electrodes other than metal- O_2 cathodes the first step is modified by adding a smaller amount of 1 M H_2SO_4 . Figure 13d shows a typical concentration profile for O_2 and CO_2 during the analysis of a Li- O_2 cathode.

Figure 13: Analysis protocol to quantify total superoxide/peroxide and carbonaceous products in battery electrodes. a) Schematic of the test setup and the sequence of solution addition and sample drawing. b) Procedure for metal-O₂ cathodes. The concentrations in the added solutions are 1 M H₂SO₄, 0.5 M FeSO₄ in 0.1 M H₂SO₄, 10 wt% H₂O₂ in 0.1 M H₂SO₄ and 2 wt% TiOSO₄ in 1 M H₂SO₄, respectively. Quantification of total superoxide/peroxide by combining O₂ detected by MS and H₂O₂ by UV-Vis photometry is detailed on page 14ff. c) Procedure for electrodes other than metal-O₂. d) CO₂ and O₂ evolution during the course of a typical analysis. In the particular case a discharged Li-O₂ cathode was measured. The colour coded background refers to the stages indicated in a. CO₂ during the blue period stems from inorganic carbonates or terminal -OCO₂Li groups in alkyl carbonates; CO₂ during the yellow shaded period evolves from organics being oxidised by Fenton's reaction.



2.3.1 Real Cells

The presented method was tested on cathodes of Li-O₂ and Na-O₂ batteries as well as on a graphite anode and a LiNi_{0.08}Co_{0.15}Al_{0.05}O₂ (NCA) cathode of a Li-ion cell.

Metal-Air cells

An exemplary Li-O₂ cell gives an Li₂O₂ yield of 94% with the presented method (based on expected amount with respect to the charge passed), while UV-Vis measurement alone after immersing the electrode in 2% TiOSO₄ in 0.1 M H₂SO₄ gave a yield of only 85%. Similar, but not as pronounced results are also obtained by analysing Na-O₂ cathodes. The optimised method gave a yield of 96% whereas UV-Vis alone gave ~94% NaO₂ yield. Figure 14 shows the values obtained with the optimised method over an entire discharge and charge cycle of a Li-O₂ and Na-O₂ cell.

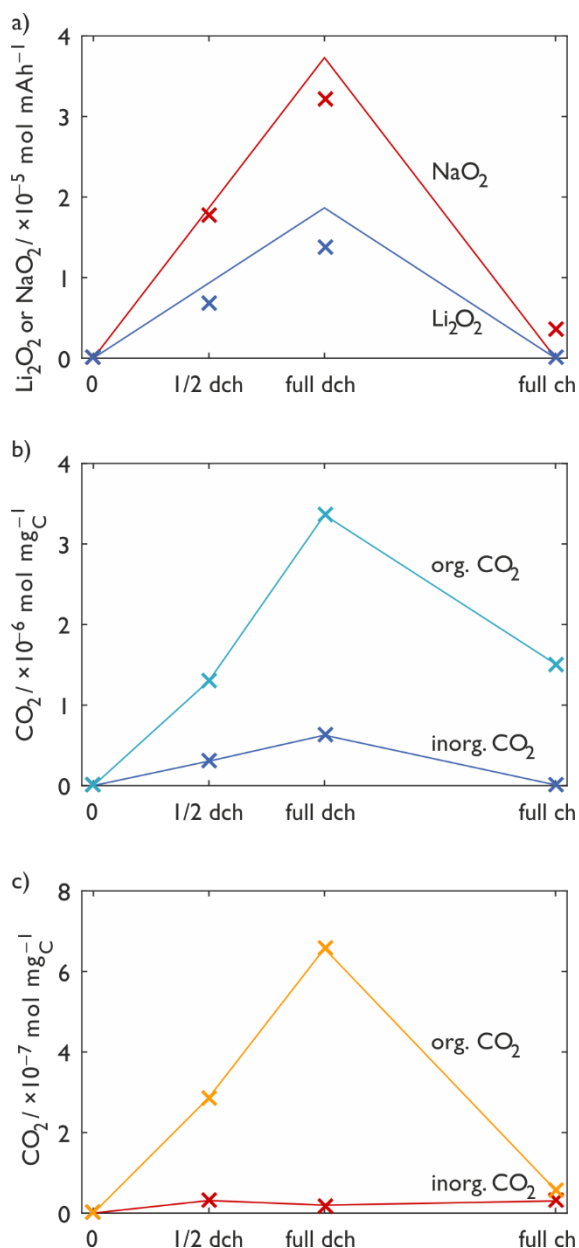


Figure 14: Product quantification over an entire discharge/charge cycle of a Li-O₂ and Na-O₂ cell determined at half and full discharge (labelled 1/2 dch, full dch, full ch, respectively). LiO₂ cells comprised a SuperP/PTFE working electrode, LFP reference and counter electrodes and 0.1 M LiClO₄ in TEGDME as electrolyte and were run at 70 mA g⁻¹ with full discharge corresponding to 1200 mAh g⁻¹. Na-O₂ cells comprised a carbon paper working electrode, Na-metal reference and counter electrodes and 0.1 M NaOTf in diglyme containing 40 ppm H₂O as the electrolyte and were run at 90 μ A cm⁻² with full discharge corresponding to 1 mAh cm⁻². Markers represent the measured amounts of Li₂O₂ and NaO₂, respectively, and full lines the theoretical values. b) Amounts of inorganic and organic CO₂ at the sampling points for the Li-O₂ cell. c) Amounts of inorganic and organic CO₂ at the sampling points of the Na-O₂ cell. The first sampling point is in either case the electrode brought in contact with the electrolyte overnight. Electrodes were washed with DME and dried under vacuum prior to analysis.

In both metal-air cell types, a significantly higher amount of organic side products is formed during cycling, while the whole amount of side products is in the range of approximately 20% corresponding to the amount of formed superoxides/peroxides.

Li-Ion Cells

Figure 15 exemplifies the capabilities of the method to follow SEI/SPI evolution on graphite anodes and NCA cathodes. The electrodes were cycled *vs.* Li-metal in LP30 electrolyte to various stages of charge, then stopped and analysed. Electrodes were either washed with dimethyl carbonate or used unwashed to capture the difference the washing introduces. It is a known problem for interphase analytics that washing is at the one hand required for surface sensitive methods such as XPS but on the other hand may alter the interphase composition. Unwashed electrodes were only analysed for inorganic CO₂, capturing M₂CO₃ and terminal -OCO₂M groups of alkylcarbonates, since Fenton's reagent would decompose the electrolyte.

Considering first the initial lithiation of graphite, inorganic CO₂ in the unwashed electrodes continuously grows to full lithiation, Figure 15a. Values for inorganic and organic CO₂ from the washed

electrodes show, in contrast, a pronounced maximum at half lithiation and decrease to full lithiation. Multiple measurements at half lithiation confirm the values to be statistically significant. To interpret this behaviour it needs to be recalled what the values represent. Organic CO₂ captures all organic compounds not washed away by dimethyl carbonate. These may not only comprise Li-containing ones but also oligo carbonates, oligo ethylene oxides, carbonate terminated ethylene oxides, and remaining electrolyte.^{76–79}

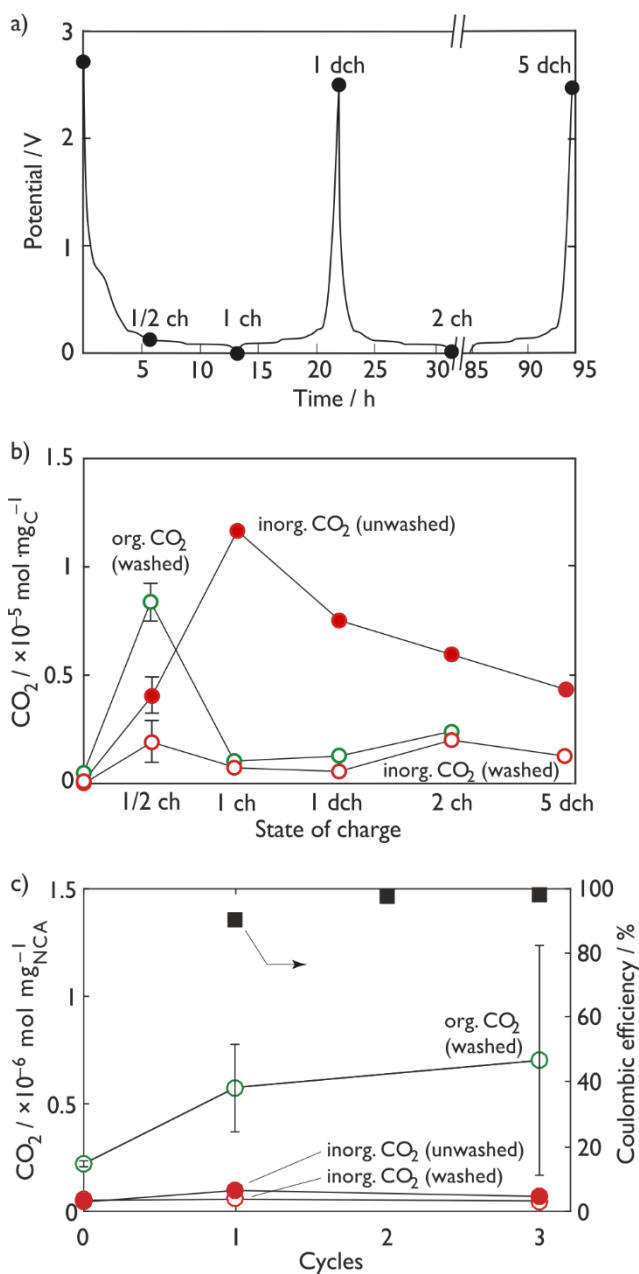


Figure 15: The evolution of total carbonaceous SEI and SPI components. The first sampling point is in either case the electrode brought in contact with electrolyte overnight. Electrodes were either washed with dimethyl carbonate (DMC) prior to analysis or analysed unwashed to capture soluble SEI components. Washed electrodes were analysed with acid and Fenton's reagent for inorganic and organic CO₂; unwashed electrodes were analysed only with acid. a) Voltage versus time during cycling of a graphite anode in LP30 electrolyte with the sampling points indicated by the black markers. b) Amount of CO₂ found at the sampling points. c) Coulombic efficiency and evolution of total carbonaceous SPI components during cycling of a LiNi_{0.8}Co_{0.15}Al_{0.05}O₂ cathode in LP30 electrolyte. The error bars are derived from at least three measurements.

Declining amounts from half to full lithiation may be explained along the reaction schemes described by Gachot *et al.* by ongoing reactions triggered by CH₃OLi, which breaks initially present oligo carbonates into the more soluble oligo ethylene oxides and CH₃OCO₂Li.¹⁹ These reactions not only take place directly on the graphite surface but in a distance such as in the separator. Conversion into more soluble or poorly attached species is also suggested by the trend of the inorganic CO₂ beyond the first lithiation in the unwashed electrodes, which captures both Li₂CO₃, terminal -OCO₂Li groups and soluble compounds. Another feature seen in the washed electrodes is a tendency for higher/lower amounts in the lithiated/delithiated states, which is in accord with dynamic change in SEI thickness noted earlier by Edström *et al.*⁸⁰ A more detailed analysis of the underlying phenomena is, however,

beyond the scope of this study, which is concerned with the method itself. As another example we measured the SPI evolution on NCA cathodes, Figure 15c. Inorganic CO₂ is slightly lower in the washed compared to unwashed electrodes and remains at nearly the same level without clear evolution. The main constituents in quantitative terms are organic compounds, which grow with cycle number and correlate well with the growing efficiency.

2.4 Summary

In conclusion, a refined method is presented to accurately and sensitively quantify total superoxide or peroxide and carbonaceous compounds in battery electrodes. The method for peroxide and superoxide clears out pitfalls with uncontrolled O₂ loss into the gas phase, which makes previously reported methods prone to underestimated values. Carbonaceous compounds are differentiated into inorganic and organic ones and the measures can discriminate between soluble and insoluble compounds by comparing washed and unwashed electrodes. The method used for metal-air electrodes is summarised once again in Table 5.

Table 5: Protocol for the analysis of a metal-air cathode analysed with the presented method.

	solution	amount	signal	corresponding to
1	1 M H ₂ SO ₄	500 μL	O ₂	M _x O ₂
			CO ₂	M ₂ CO ₃
2		-400 μL		+ TiOSO ₄ → UV-Vis (TiO ₂ SO ₄) → M _x O ₂
3	H ₂ O	3 mL	CO ₂	CO ₂ diluted in the water evolves due to decrease of pH
4	0.5 M FeSO ₄ in 0.1 M H ₂ SO ₄	500 μL	CO ₂	organic carbonates
5	10 wt% H ₂ O ₂ in 0.1 M H ₂ SO ₄	150 μL	CO ₂	organic carbonates
			O ₂	by-product of Fenton's reaction

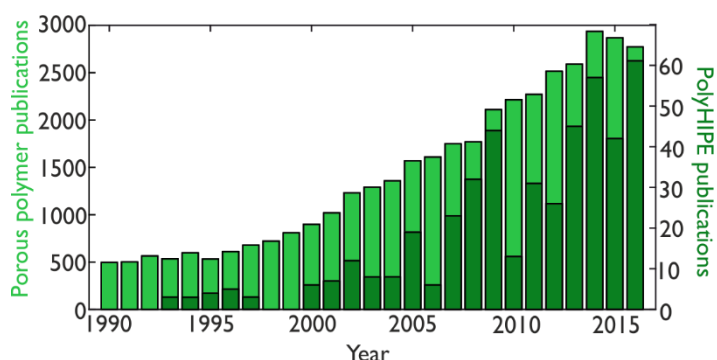
With the use of this method, it is now possible to further investigate the two other fields investigated in this work.

3 Porous Cathode Materials for Li-O₂ Batteries

3.1 Theoretical Background

The requirements for cathode materials in lithium oxygen batteries, namely high and open porosity as well as chemical and electrochemical stability were already discussed in the introduction. Here, the goal to synthesise an electrode material based on a carbonised porous polymer was followed and the possibility was investigated to replace all or part of the carbon by Ti ceramics such as TiC, TiO_x or TiO_xC_y regarding preparation options, morphology and electrochemical characteristics. The research on polymers, and particularly porous polymers, has increased immensely over the last 25 years (see Figure 16, left handed y-axis).

Figure 16: Number of publications regarding 'porous polymers' (left handed y-axis) and 'poly-HIPEs' (right handed y-axis) in the last 25 years.



With regard to porous polymers, the high internal phase emulsion (HIPE) route has received increased interest. Also the integration of Ti in organic polymers and the formation of (more or less) porous TiC materials have been investigated in literature and will be discussed in the following sections.

3.1.1 Porous Polymers

This group of polymers consists of macromolecules containing at least one, but normally many pores inside the polymer network. These materials are divided into three groups according to IUPAC recommendation based on their pore diameter:⁸¹

- macroporous: > 50 nm
- mesoporous: 2-50 nm
- microporous: < 2 nm

Porous polymeric materials have, in comparison to non-polymeric porous materials, many advantages in terms of preparation. Polymers are easily processable, as they can be cured in different moulds⁸²⁻⁸⁴ or as thin films.^{85,86} They are usually organic, which means that they have a bulk density of typically 0.9 to 1.5 g cm⁻³ and are therefore often lighter than comparable inorganic materials. Additionally, a broad range of synthesis routes enables the preparation of various porous macromolecules with diverse chemical functionalities.⁸⁷⁻⁹⁰ A very simple method for the preparation of porous polymers is the direct templating method.⁹¹⁻⁹³ For that technique, the same approach as for plastic bottles is used; the template is in the μm to nm range and therefore a few orders of magnitude smaller than the afore mentioned. Silica nanomaterials are most frequently used as templates. After mixing template and monomer by infiltration or adsorption, the material is polymerised *in situ*. Subsequently, the template is removed, which in case of the silica nanoparticles is done by wet chemical etching with HF or NaOH.⁹⁴ Another method uses self-assembling block copolymers, which is especially useful for the formation of meso-

and macropores.^{85,95,96} In contrast, all three pore size ranges can be synthesised with the direct synthesis approach. Here, the pores are formed during the solvent polymerisation and remain in the sample after the solvent is removed.⁶³⁻⁶⁵ Porous polymers can also be prepared by interfacial polymerisation or high internal phase emulsion polymerisation. Both techniques are performed in a system of two liquid, immiscible phases. In the former case, the polymerisation takes place at the interface of both liquids, while in the latter only one phase takes part in the polymerisation.

Porous polymers are characterised by a number of properties as summarised in Figure 17.⁹⁴ Pore size and geometry are key properties and influence directly the specific surface area of a material. Small pores contribute stronger to the surface area per total pore volume than larger pores according to $\text{surface/volume} = 3/\text{radius}$ for spherical pores. Additionally, chemical characteristics like the framework structure, the functionality of the surface¹⁰⁰ and the pores¹⁰¹ are important and can be tuned by employing functionalised monomers⁹⁶ or post-modification processes.^{102,103}

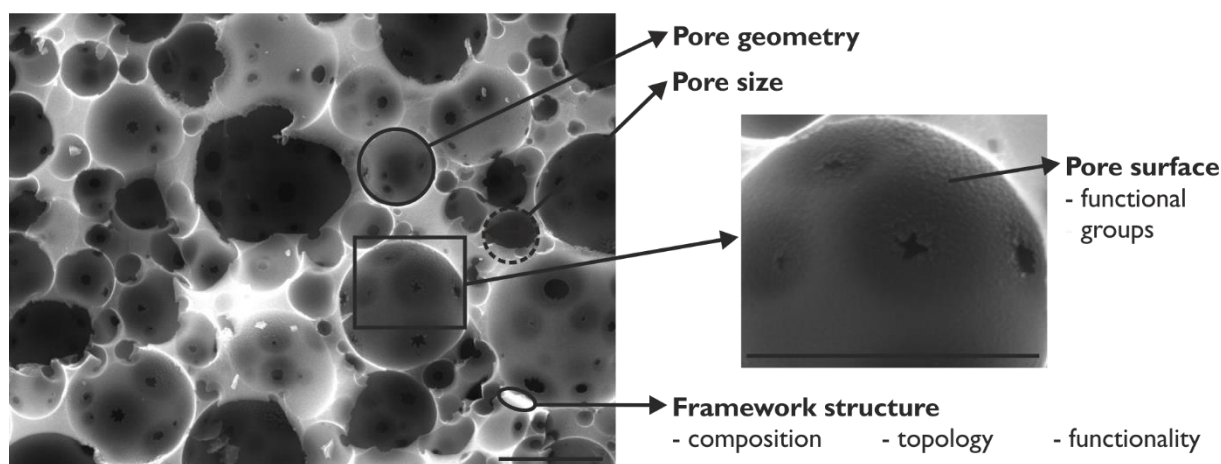


Figure 17: Illustration of the important porous polymer characteristics exemplary shown for a polyHIPE material; scale bars correspond to 10 μm .⁹⁴

Depending on those parameters, and also the synthetic method, porous materials have various possible applications ranging from gas or drug storage^{104,103} *via* separation materials/membranes^{105,106} to electrode materials for energy storage^{107,108} or precursors for nanostructured carbon. For the latter application, and to obtain porous carbon in general, mainly highly ordered porous polymers like aerogels¹⁰⁹ or hierarchically structured copolymers^{110,111} are carbonised at temperatures above 900 $^{\circ}\text{C}$ under inert conditions, resulting in high surface areas beyond 600 $\text{m}^2 \text{g}^{-1}$.

High Internal Phase Emulsion (HIPE) Polymerisation

As mentioned above, high internal phase emulsion (HIPE) polymerisation is sometimes used to prepare porous polymers. In this technique, an emulsion consisting of two immiscible liquids is formed. First, the continuous, external, phase is mixed with the dispersed phase; normally the first is the monomer and the second an immiscible solvent, see Figure 18. The internal phase forms droplets, which are evenly distributed in the mixture. When the ratio of the dispersed phase reaches 74.05%, the maximum packing density for uniform spheres in a face centred cubic lattice is reached. By increasing the ratio of the dispersed phase even further, the droplets are deformed to polyhedral structures, which are surrounded by a thin layer of the external phase. Now the monomer is polymerised, fixing the polyhedral structure in the process. Concurrently the density of the continuous phase changes, which ruptures the pore walls at the thinnest points of the external phase forming holes. This phenomenon leads to the open porous character of polymerised HIPEs (polyHIPEs). In a final drying step, the internal phase is removed resulting in the polymer with an open-porous structure.

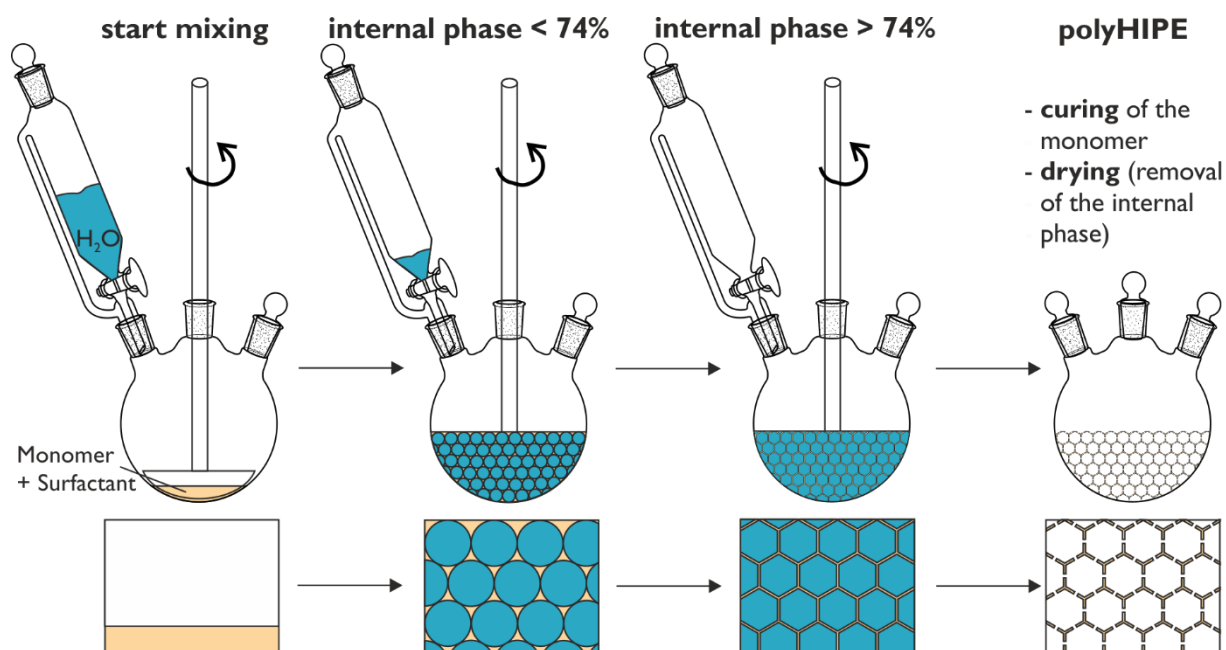


Figure 18: Step by step preparation of a polyHIPE and changes in the structure of the internal phase.¹¹²

Additional to the above explained HIPE setup, also medium and low internal phase emulsions are used with an internal phase volume between 30% and 74% or even below 30%.¹¹³ In this work however, the focus will lie on setups with an internal phase ratio larger than 74%. These materials have a very characteristic morphology with an open cell structure consisting of macropores resulting from the dispersed phase (=voids) with sizes of 0.5-600 μm which are interconnected through windows (0.1-300 μm).¹¹⁴

As pictured in Figure 18, water is used as dispersed phase in a typical setup, as it is easy disposable, cheap and non-toxic. For monomers/setups where this is not possible, supercritical CO_2 ¹¹⁵⁻¹¹⁷ or ionic liquids¹¹⁸ can be used as dispersed phase. Combined with oil-in-oil emulsions, this leads to a broad scope of potential monomers. To further vary the scope of monomers, also different polymerisation techniques can be applied. Starting from the mainly used free radical polymerisation, now also atom transfer radical polymerisation (ATRP),¹¹⁹ thiol-ene click chemistry,¹²⁰ poly-condensation and ring opening metathesis polymerisation (ROMP)¹²¹ are frequently used in the preparation of polyHIPEs.

To finally obtain a porous polymer, a stable emulsion during the mixing and subsequent curing step is essential. For this purpose mainly organic and non-ionic surfactants are used. The surfactant has to be chosen with respect to its solubility in the external, continuous phase, as stated by the Bancroft rule.¹¹² According to that rule, the continuous phase is always the phase where the surfactant is better soluble. Often, high amounts in the range of 10 to 30 vol% of surfactants like sorbitanmonooleate (Span 80) have to be used to obtain stable emulsions;¹¹⁹ some surfactants like PEO-PPO-PEO (Pluronic L-121),¹²² lead to significant changes in the morphology depending on the used amounts. Nanoparticles, too, can act as suitable surfactants in a HIPE polymerisation, then called Pickering HIPE.^{114,123} These materials can, with rather low ratios of about 1 wt%, stabilise the emulsion by self-assembling at the emulsion interface¹²⁴⁻¹²⁶ and can additionally enhance the polyHIPE properties in terms of mechanical strength or thermal conductivity.¹²⁷ The nanoparticles are divided into three groups: non-bond (fillers), single bond (grafted onto) or multibond (crosslinked) to the polymer network.¹¹² When only nanoparticles are used as surfactants, it results in a polymer with equally distributed closed pores.¹²⁴ By combining both nanoparticles and organic surfactants, less surfactant is needed and an open porosity can be obtained

in the final material.^{128,129} A wrong surfactant to monomer ratio, elevated curing temperatures or slow polymerisation rates can lead to droplet coalescence or Ostwald ripening.¹¹²

While the materials are highly porous (> 74%), the specific surface area is typically below 50 m² g⁻¹.⁹⁴ The surface area can be increased by using a porogenic solvent during the HIPE polymerisation. In a divinylbenzol/ glycidyl methacrylate (DVB/GMA) system for instance, toluene was added during the polymerisation, which led to a surface area of 371 m² g⁻¹ and a mesopore diameter of approximately 5.6 nm.¹³⁰ Other possibilities to increase the surface area and/or functionalise the polyHIPE are different post modifications, ranging from chemical etching to hyper crosslinking. With the latter method, the surface area can be increased to up to 1200 m² g⁻¹.¹³¹ In a particular impressive example, a DVB based setup containing different ratios of vinylbenzyl chloride (VBC) and styrene the polymer is cross linked subsequently.¹³¹ By adding an initiator for post-polymerisation modification to the HIPE mixture, functional polymers can be grafted from the pore surface.¹¹²

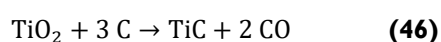
PolyHIPEs as Precursors for Porous Materials

The as-made or further modified porous polymers then can be carbonised in a subsequent heating step. In many examples, the specific surface area as well as the conductivity of the material could be increased due to the carbonisation. Resorcinol-formaldehyde,¹³² poly(furfuryl alcohol)¹³³ or styrene/divinylbenzene¹³⁴ polyHIPEs were carbonised at 800 °C to 1200 °C, resulting in materials with surface areas of 250 m² g⁻¹ to 400 m² g⁻¹ and conductivities of approximately 30 S m⁻¹.

PolyHIPEs can also be used as templates for porous inorganic materials. Porous metal-oxide monoliths can be prepared by filling the pores with suitable precursors and calcining the resulting monolith.^{135,136} For instance the calcinations of aluminium containing polyHIPEs at temperatures above 900 °C giving a material purely consisting of alumina without any organic traces. The typical polyHIPE structure consisting of voids and windows was maintained, but the size of both cavity types increased significantly with higher calcination temperatures. The surface area, however, decreased with higher calcination temperatures and was only 5 m² g⁻¹ at 1300 °C instead of approximately 230 m² g⁻¹ at 600 °C.¹³⁷

3.1.2 Porous Titanium Carbide

Titanium carbide, as one member of the broad group of transition-metal carbides, has a low electrical resistivity, a good corrosion and oxidation stability, is stable when exposed to high temperatures and its hardness is in the range of diamond.^{138,139} Possibilities to synthesise TiC range from physical and chemical vapour¹⁴⁰ deposition and chemical solution deposition to film growing techniques on different substrates or carbothermal reduction. Many of those methods do not result in significantly porous carbides, but is one of the main requirements for the application in Li-oxygen batteries. Therefore, this chapter will focus on methods to prepare porous materials, particularly carbothermal reduction, which was the method of choice in this thesis. The carbothermal reduction of TiO₂ by C, following Equation (46)



which in industry is performed at 1700 °C to 2000 °C,¹⁴¹ leads to TiC. The mechanism was studied thoroughly in the literature and can be divided into three steps, which consist mainly of two parts as depicted in Figure 19.^{139,142,143} Theoretically literature states that this reaction is already possible above 1289 °C¹³⁹ or even at temperatures around 1100 °C,¹⁴¹ but impeded by uneven reactant distribution or limited contact area.

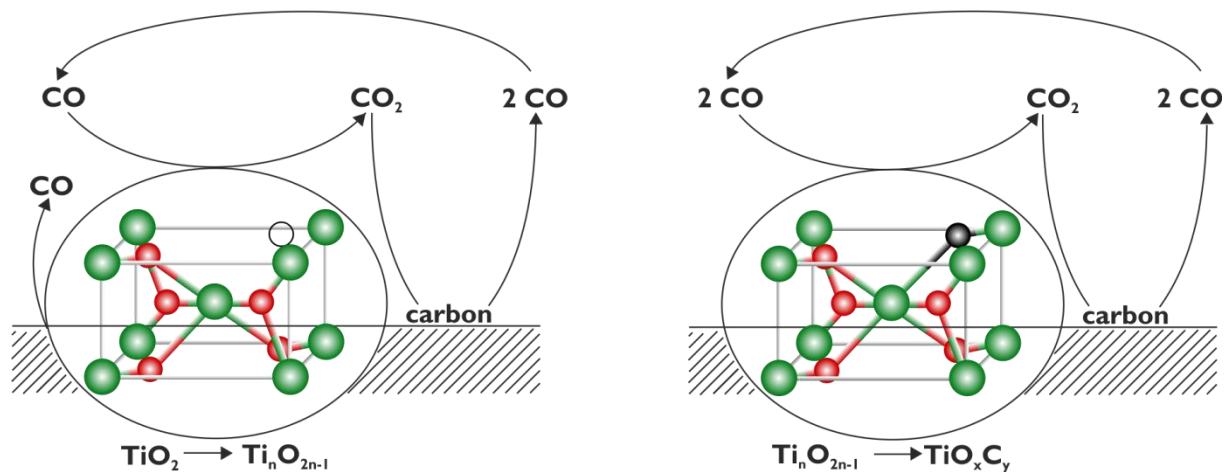
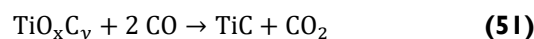
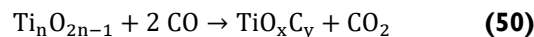
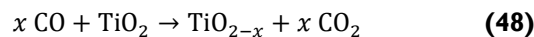


Figure 19: Reaction mechanisms during carbothermal formation of TiC; left: reactions leading to oxygen vacancies in the TiO₂ lattice; right: reactions that introduce carbon into Ti lattice.¹⁴²

The first step is a solid state reaction between carbon and titania, resulting in the formation of CO (*cf.* Equation (47) and Figure 19, left part). CO then reacts with the TiO₂ to form CO₂ and different Magneli phases with the general formula Ti_nO_{2n-1}, Equation (48). The CO is regenerated in the Boudouard equilibrium throughout the whole process as seen in Equation (49). During the whole step, no carbon is introduced into the metal-oxide network.



The formed TiO_{2-x} (also written as Ti_nO_{2n-1}), mainly Ti₃O₅ and Ti₂O₃, is further reduced to a sub stoichiometric TiO_x, wherein carbon starts to insert according to the right side of Figure 19. Now, carbon is inserted into the Ti_nO_{2n-1} lattice *via* the oxidation of CO to CO₂, Equation (50). In this step, CO acts as reducing agent of the Ti_nO_{2n-1} and as carbon source. As the rate of the C insertion is rate limiting, the formed oxycarbide is sub-stoichiometric with respect to the carbon content. In the final step towards pure TiC, both mechanisms as depicted in Figure 19 substitute oxygen for carbon.^{139,142}

The choice of the carbon source is, on the one hand, important, as its structure directly influences the CO regeneration according to Equation (49) and is decisive for the TiC formation. On the other hand, by choosing the carbon source with care, it can also result in porous TiC materials with significant surface areas. In many cases, however, the surface area is reduced by increasing heating temperature, whereas especially Equation (51) only removes all the oxygen at temperatures above 1500 °C.¹³⁹ If, for instance, Vulcan (surface area 250 m² g⁻¹) is used as carbon source, the resulting TiC still shows a surface area of approximately 100 m² g⁻¹ after heat treatment at 1400 °C.¹⁴¹ Graphene as carbon source was also tested and led to a TiC material after heating to 1250 °C containing interconnected nanocrystals with an average particle size of 3.6 nm and a surface area of 175 m² g⁻¹.¹⁴⁴ This material was, due to its good electrical conductivity, even used as a Li-intercalation material. Tubular TiC fibres were for instance already used as supercapacitor electrodes. These materials were synthesised using cotton and carbon nanotubes as carbon sources which led to a surface area of around 255 m² g⁻¹.^{145,146} Also the size of TiO₂ is significant for the complete removal of oxygen. Large TiO₂ particles can, due to diffusion problems,

hinder the complete conversion of TiO_2 to TiC at temperatures below $1700\text{ }^\circ\text{C}$.^{141,147} With small enough TiO_2 particles, the mass transfer occurring during the carbothermal reduction, progresses quicker.

There are also concepts starting with TiC and implementing the porosity in an additional modification step. Here, again appropriate particle sizes as well as a homogeneous distribution of all materials are essential to form porous TiC . By pursuing this method, Ma *et al.* mixed TiC , Ni (as metallic binder) and urea (as space holder) and heated it to $1500\text{ }^\circ\text{C}$. Upon heating under reduced pressure, gases evolving from the urea form micropores in the TiC particles. The resulting material had a porosity in the range of 60-70% but no surface area was given in that case.¹⁴⁸ Spallation targets used at CERN are also produced starting from a ball-milled TiC /carbon mixture that is heated to $1500\text{ }^\circ\text{C}$ under reduced pressure. Here, different Ti/carbon ratios and a variety of carbon materials were tested resulting in grain sizes of 60 to 85 nm but surface areas only in the range of 2 to $24\text{ m}^2\text{ g}^{-1}$.¹⁴⁹

3.2 Dicyclopentadiene based Porous Materials

In all polymerisation experiments, dicyclopentadiene (DCPD) was polymerised *via* a ring opening metathesis polymerisation (ROMP) using a Grubbs-type Ru based initiator, as were all other monomers used in this work. The mechanism of this reaction is depicted in Figure 20 and starts with the activation of the Ru-initiator (2). The removal of the tricyclohexylphosphine-ligand (PCy₃) is a thermally driven process which accelerates at elevated temperatures. The cyclic olefin can now add to the vacant coordination site of the initiator *via* a [2+2] cycloaddition (3) forming a ruthena-cyclobutane based intermediate (4). This reaction is formally symmetry forbidden and has therefore a high activation energy which is lowered by the Ru initiator. The next step, leading to again a C-Ru double bond and a coordination site, is driven by the release of ring strain (5). Subsequently a new monomer can add to the catalyst and start the reaction anew. Additionally to the chain grow mechanism, also crosslinking *via* the ROMP mechanism and olefin addition is possible for monomers containing more than one ring-double bond.

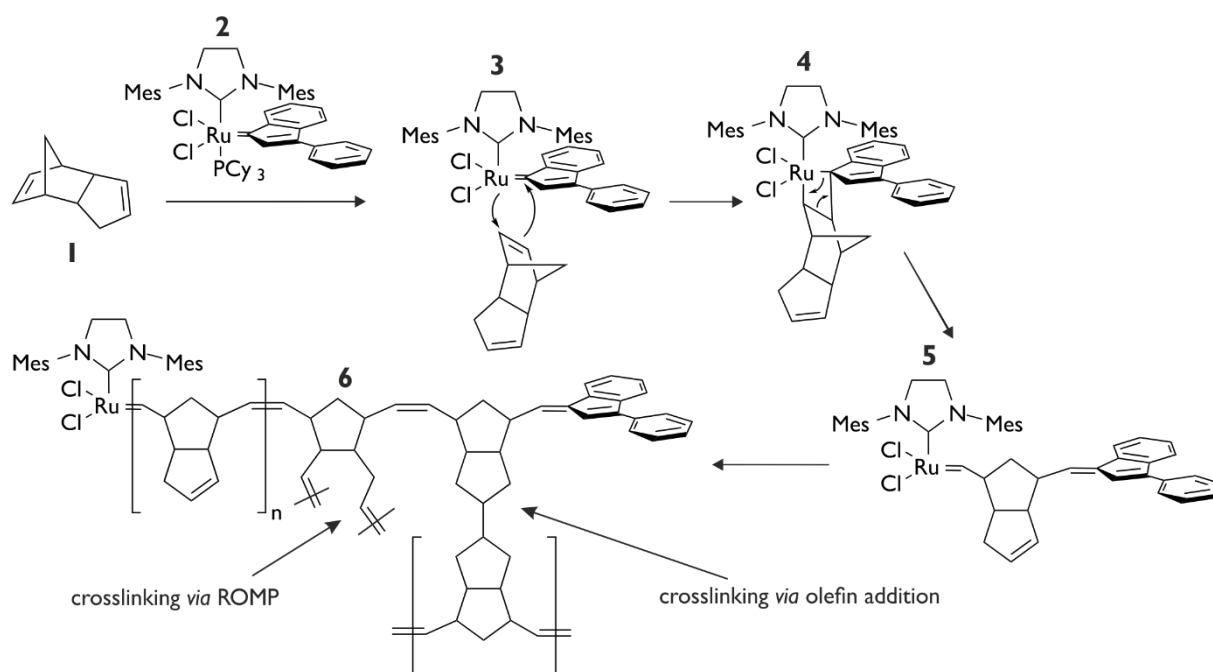


Figure 20: Ring opening metathesis polymerisation of DCPD using a Ru-initiator.¹⁵⁰

3.2.1 Polymerisation with a Porogenic Solvent

For the use as cathode material, the first goal was to obtain a highly porous carbon network in a suitable shape with a stable morphology. Therefore, high porosities of the dried polymers of 70% or higher are targeted. Additionally, a high surface area and combined meso- and macroporosity are crucial for obtaining suitable materials. By polymerisation with a porogenic solvent, the monomer is diluted in a suitable solvent, polymerised and dried leading to a, hopefully, stable and porous monolith.

Searching for the Right Solvent

DCPD is highly soluble in many organic solvents like toluene or heptane and is still sufficiently soluble in more polar solvents like acetone or isopropanol. A porous polymer may be achieved by polymerising diluted DCPD solutions with the DCPD-to-solvent ratio in the range of 1/5 to 1/10. With the solvents mentioned in Table 6, transparent or opaque monoliths could be obtained. The goal was to gain further

information about the properties of the DCPD polymerisation in different solvents. Solvents were analysed for their ability to form porous polymers with control of morphology, porosity, and shrinkage after solvent removal. Products were analysed visually and by SEM imaging.

Table 6: DCPD polymerised in different solvents and subsequent characterisation and drying of the monoliths. In terms of solubility, the monomer was either badly (–), partly (~) or completely (+) soluble.

solvent	solubility	after polymerisation	after drying
acetone	~	solid, opaque	opaque, high volume loss, strong adhesion to the glass wall
cyclohexane	+	transparent, slightly yellow, elastic	transparent, elastic, little volume loss
cyclohexanone	+	solid, opaque	solid, opaque, little volume loss
dichloroethane	+	solid, getting opaque with increase in solvent amount	high volume loss, strong adhesion to the glass wall
ethyl acetate	~	solid, opaque, surface slightly yellow and soft	opaque, soft, light
heptane	+	opaque solid in a colourless solution	opaque, brittle
isopropanol	–	colourless, opaque, easy to cut	high volume loss, colourless, opaque
tetrahydrofuran	+	transparent, solid	transparent, high volume loss

The samples usually shrunk significantly upon drying. Only cyclohexane and cyclohexanone resulted in acceptably low volume loss. The high boiling point of many solvents required the drying to be performed under reduced pressure, which led to a rapid reduction of the solvent content in the sample. This caused the morphology to collapse and significantly decreased the porosity. To be able to dry the samples under ambient conditions, we tested first exchanging the solvent with acetone or dichloromethane (DCM) which then evaporates more easily. The samples were immersed in the liquid for a few hours, which led to slight increase in size during the process but could not diminish the shrinkage in the subsequent drying step.

Regarding the polarity of the solvents tested in Table 6, the macroscopic morphology changes significantly when solvents are changed from low to high polarity (*cf.* Figure 21, left and right). While non-polar solvents like cyclohexane led to a lamellar structure, the polymerisation with isopropanol or also cyclohexanone (CHO) resulted in a formation of a network that consists of small particles.

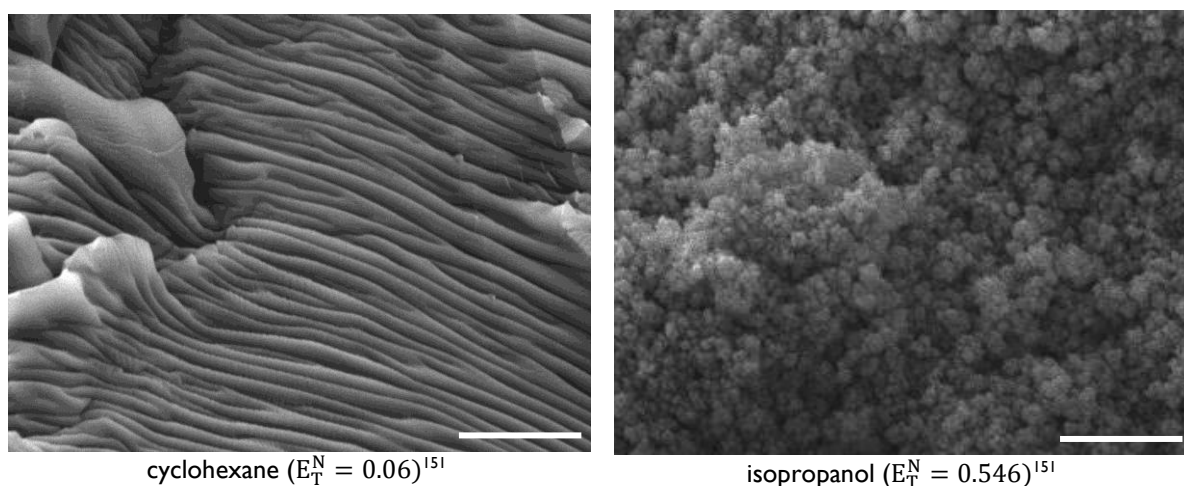


Figure 21: SEM images of air dried pDCPD-samples polymerised with a solvent excess of 1:5; E_T^N is the relative polarity (water = 1); scale bars correspond to 20 μm .

To increase and vary the surface of the DCPD polymer (pDCPD), the polymerisation of DCPD with a solvent mixture (cyclohexane (CH) and isopropanol) was tested. Due to the poor solubility of the monomer in isopropanol, a ratio of 9/1 (CH/isopropanol) was used. Adding a small amount of isopropanol led to an opaque solution, which resulted in a solid polymer consisting of opaque and transparent parts (Figure 22a). The shrinkage of that material was more pronounced for the mixed

solvent sample than when pure cyclohexane was used. Oxidation of the pDCPD, visible through the colour change to orange, worked well in both cases. Regarding SEM images, it was not possible to truly combine both morphologies. In the bulk material, the mainly used cyclohexane strongly influenced the morphology which resulted in a lamellar structure. The surface did not show any open porosity and when breaking the sample, a mixture of a slightly porous structure combined with non-porous areas was visible, as shown in Figure 22b.

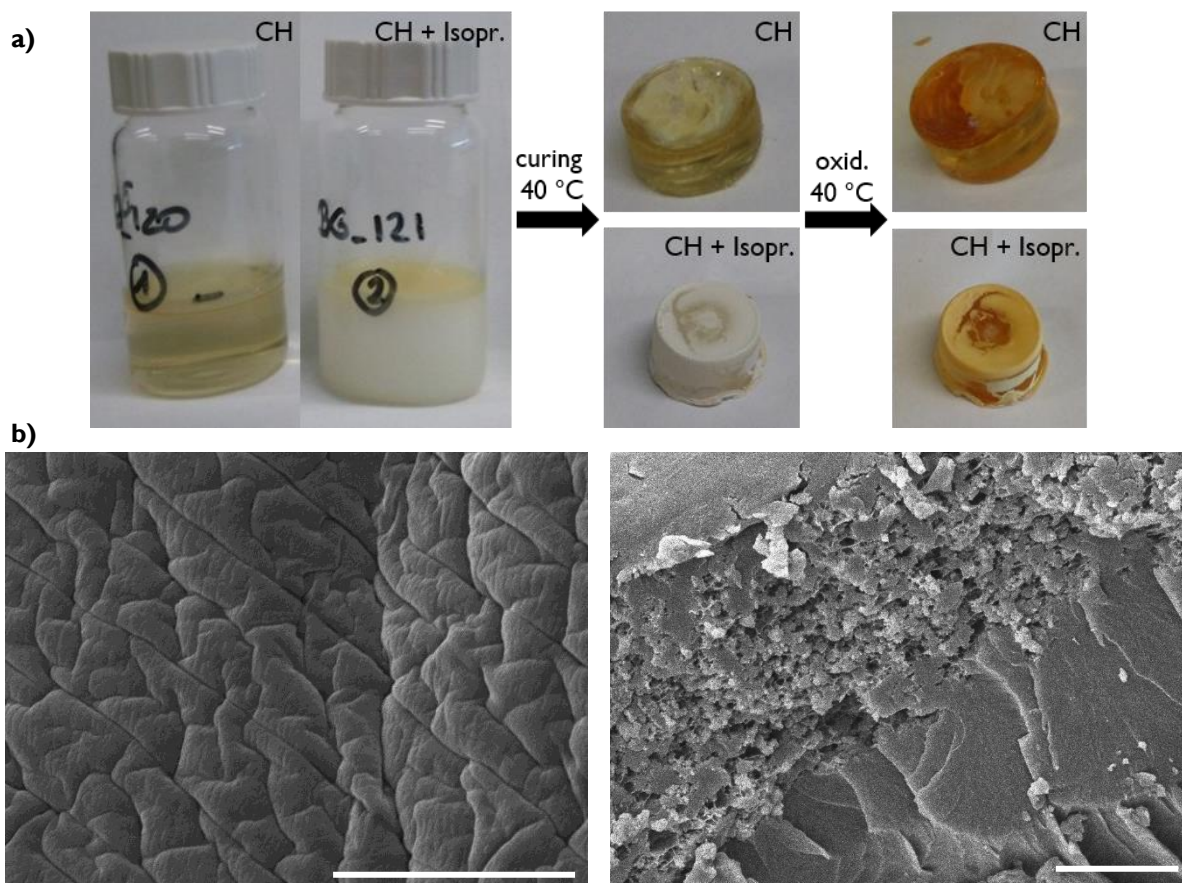


Figure 22: Polymerisation of DCPD with 1/5 solvent (solvent was CH or a 9/1 mixture of CH/isopropanol); a) vessels before polymerisation and monoliths after polymerisation and oxidation; b) SEM images of the bulk and a crack of the polymer synthesised with the solvent mixture; scale bars correspond to 10 μm .

Tests with other solvent ratios could not improve the shrinkage or the morphology of the samples. With pure cyclohexanone and cyclohexane two solvents could be identified that modify the pDCPD structure without immense shrinkage stress during the drying process.

In the future, the electrode material should be directly polymerised in a disc-shaped mould, which consists of a solid glass or Teflon[®] plate as bottom plate and a Teflon[®] plate with a round hole in different thicknesses. Both plates are fixed with clasps, which cannot hinder solvents with low viscosity from leaking during the polymerisation step. When comparing cyclohexane and cyclohexanone, the latter has a significantly higher viscosity and will therefore be used for further tests with porogenic solvents (see page 47ff). Cyclohexane was tested as a co-solvent for the high internal phase emulsion polymerisation of DCPD (see page 32ff).

3.2.2 High Internal Phase Emulsion of DCPD

In contrast to the use of porogenic solvents, polyDCPDs synthesised with this technique do not suffer from shrinkage during drying which results in a stable surface morphology. To have a high enough

surface area, the amount of the internal, aqueous, phase was tuned to obtain a porosity of 80%. For this work, DCPD was used as the continuous phase, Pluronic L-121 as surfactant and water as continuous phase, as depicted in Figure 23.

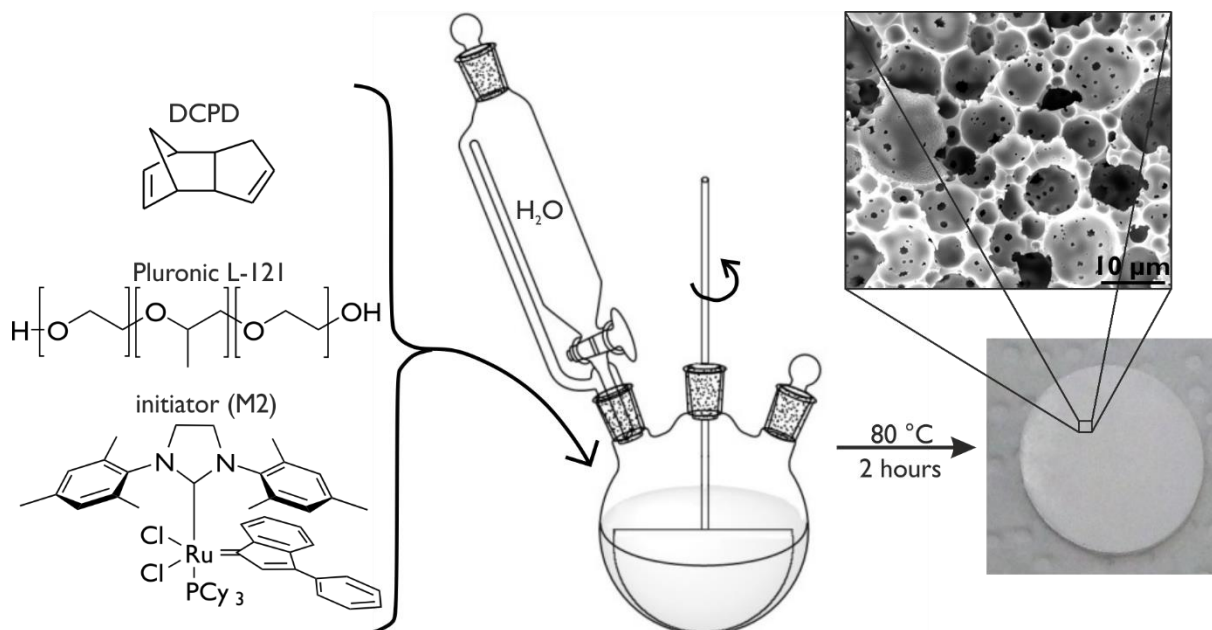


Figure 23: Preparation scheme for the synthesis of pDCPD *via* a HIPE polymerisation with a continuous phase consisting of DCPD (monomer) and Pluronic L-121 (surfactant) and water as the internal phase. After polymerisation, typical picture and SEM image are given.

After adding the water slowly and stirring for one hour, the initiator is added and the honey-like, creamy mixture turns red. In that case, M2 is used as the initiator, as it polymerises rather slowly at room temperature and allows the mixture to be filled in disc-like moulds. The curing takes place at 80 °C resulting in colourless opaque discs after 2 hours. They are still easily bendable, but already have the desired morphology, as visible in the SEM image of Figure 23. However, they do not maintain their shape when immersed in organic solvents like toluene or during heat treatment. The first is necessary to later on modify the purely organic material with a Ti-source. The latter is important to obtain a conductive material. Shape and morphology can be maintained when the discs are oxidised under ambient conditions or at 40 °C prior to further modification steps. The double bonds still present after the polymerisation react with oxygen from the air. In this step, the material turns yellow and becomes more brittle, but the macroporous morphology does not change.

Instead of melting during the carbonisation, an oxidised disc results in a black and smaller version after the heating step. This is nicely visible in Figure 24a, where all four discs are scaled equally. In contrast to that, the macroporous structure did not change significantly when comparing Figure 23 and Figure 24b. The size of the cavities and the connecting windows stay approximately the same. How this is possible in combination with the significant shrinkage of the disc is still unclear.

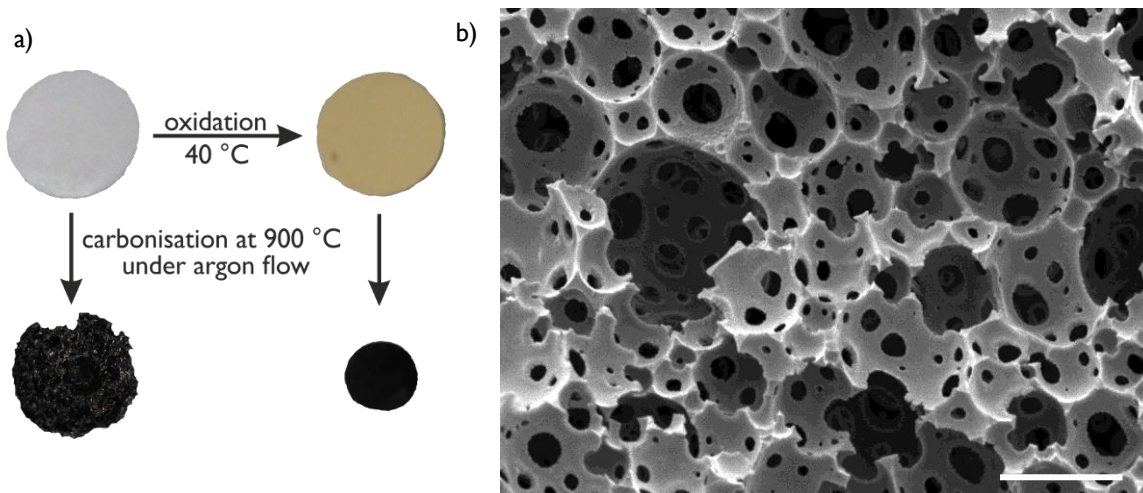


Figure 24: Carbonisation of a pDCPD disc; a) carbonisation of an un-oxidised and an oxidised sample, b) SEM image of a carbonised sample, which was beforehand oxidised; scale bar corresponds to 10 µm.

Porogenic Solvents combined with the HIPE Setup

To obtain high surface areas, the porogenic solvent approach was combined with the HIPE setup. Cyclohexane is an aprotic solvent, dilutes DCPD very well and leads to a lamellar surface of the resulting polymers. The ratio of DCPD and cyclohexane was varied from 1:0 to 1:2 and the amount of water reduced accordingly to result in a stable monomer/liquid ratio. The samples depicted in Figure 25 show increasing shrinkage, but also the change in appearance.



Figure 25: pDCPD monoliths synthesised with the HIPE procedure using different DCPD:cyclohexane ratios for the continuous phase. Samples are depicted after the drying step.

While the sample with only 20% cyclohexane looks quite similar to the one without any additional organic solvent, both monoliths with a higher solvent content differ significantly. When pure cyclohexane is added, the sample shrinks strongly and the surface was slightly darker after oxidation and drying. As soon as the amount of cyclohexane exceeds the weight of the monomer, a phase separation occurs which leads to a yellow opaque cylindrical body ('HIPE' part) combined with a transparent, brownish upper part ('porogenic solvent' part). The phase separation occurred despite the fact that a higher amount of surfactant was added with increasing amount of the external organic phase; apparently the surfactant could not stabilise the emulsion. The resulting monoliths also had a decreasing inherent stability. In contrast to drying with pure water as the liquid phase, additional cyclohexane caused significant shrinkage during the drying process. The extent of shrinkage depends on the organic solvent ratio used for the polymerisation, as visible in Figure 26. As monoliths without cyclohexane did not shrink, they are not shown in this diagram. While both losses are below 5% for the samples with 20% cyclohexane, the shrinkage strongly increases for polymers with higher cyclohexane content. Additionally to the 'normal' shrinkage in both height and diameter of the cylinders, the samples are less dimensionally stable which leads to bellied monoliths. This explains the reduced average diameter

shrinkage for the samples with a high amount of cyclohexane and a strong increase in the height loss of more than 30%.

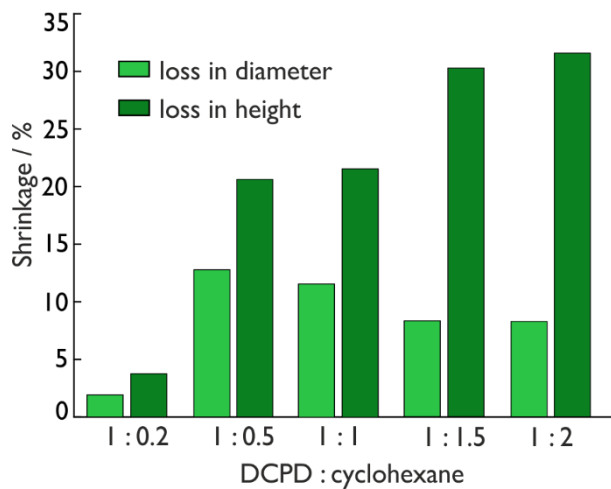


Figure 26: Relation between shrinkage in diameter/height of the prepared monoliths and the amount of cyclohexane used during polymerisation. All measurements were done for two different samples and at three different positions and the mean values are given.

Materials made with cyclohexane are even after oxidation elastic like rubber instead of being stiff and brittle, two parameters characteristic for DCPD-HIPes. This complicates the sample preparation for SEM imaging as the new properties lead to a tearing of the material instead of creating a clean break. The results of that problem are visible in the lower left picture of Figure 27, where the characteristic HIPE structure is not visible any more. Partly, that is due to the flexibility of the material, but additionally, the high cyclohexane content also leads to a loss of the HIPE-structure.

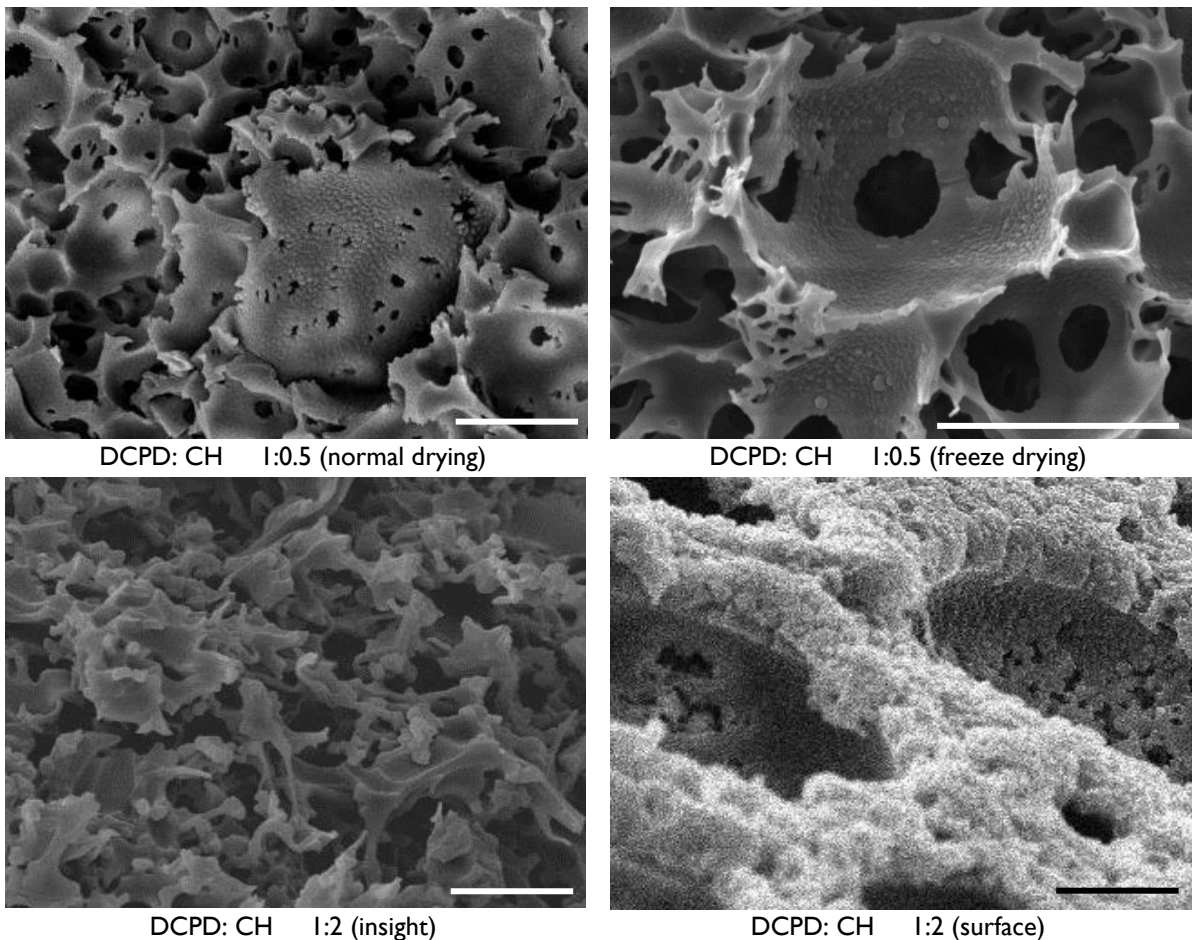


Figure 27: SEM images of samples with varying CH amount in respect to the DCPD (upper vs. lower images) and changing drying procedure (*cf.* both pictures in the upper row); scale bars correspond to 20 μm .

An additional lamellar structure, which was the goal of these experiments, is not clearly visible. A slight surface roughness is visible for both samples with 1/5 DCPD/CH. However, the possibility cannot be excluded that those irregularities in the surface do simply originate from shrinkage during drying. On the surface of the material (Figure 27, lower right side), which could be measured without tearing the monolith apart, the HIPE-like cavities are still visible. Shrinkage occurs during drying and depends on the cyclohexane content of the material. Cyclohexane has a melting point of approximately 7 °C, which makes freeze drying possible when cooling the monoliths with ice water. Then, the visible shrinkage can be slightly minimised and the macro-porous structure visible in the upper right SEM images of Figure 27 is still present after the drying step.

CO₂ Activation of DCPD-HIPEs

The introduction of a porogenic solvent did not result in the wanted changes in porosity and surface area. The carbonisation of pDCPD polyHIPEs already leads to a conductive material. But despite high porosities, the surface areas of carbonised pDCPD polyHIPEs are in the range of 10-20 m²g⁻¹. These materials solely contain macropores but lack micro- and mesoporosity, which mainly contribute to the surface area. Therefore, this material is porous enough to store some Li₂O₂ but may not result in high capacities of a few 1000 mAh g⁻¹.

One possibility to increase the surface area by adding micro- and mesopores is the activation of the material with CO₂. This is performed at the same temperature as the carbonisation step and can either be carried out directly after the carbonisation or by heating the samples a second time. Both options were tested with different heating plateaus and heating times with the exact values summarised on page 85.

Table 7: Different parameters of the carbonised and activated pDCPD HIPE samples.

heating			mass loss	bulk density	porosity ^{a)}	open porosity ^{b)}	surface area ^{c)}	pore diameter ^{d)}
temp.	carb.	act.						
900 °C	2 h	2 h ^{e)}	77%	0.273 g cm ⁻³	88%	65%	668 m ² g ⁻¹	3.42 nm
900 °C	2 h	1 h ^{f)}	71%	0.234 g cm ⁻³	90%	88%	734 m ² g ⁻¹	5.45 nm
900 °C	2 h	2 h ^{f)}	84%	0.175 g cm ⁻³	93%	61%	1065 m ² g ⁻¹	5.46 nm
1100 °C	2 h	1 h ^{e)}	85%	0.223 g cm ⁻³	90%	72%	814 m ² g ⁻¹	4.01 nm

^{a)}calculated using the formula given in the experimental section; ^{b)} measured using TEGDME as pore filler; ^{c)} measured using BET; ^{d)} measured using BJH, average value is given; ^{e)}carbonisation and activation were performed in one heating cycle; ^{f)}sample was cooled down between carbonisation and activation.

Three of the synthesised materials were carbonised at 900 °C, albeit the total time under elevated temperatures differs depending on the heating program, shown in Table 7. With increasing mass loss due to sustained high temperatures from heating in one step to two heating processes to 900 °C, the bulk density of the obtained product decreases. The bulk density is calculated using the density of graphite ($\rho = 2.26 \text{ g cm}^{-3}$) as reference for non-porous carbon materials. The surface area increases with carbonisation time. The cooling and heating between carbonisation and activation nearly doubled the surface area from 668 m² g⁻¹ to 1065 m² g⁻¹. The open porosity, on the other hand, does not follow a significant trend. Here, TEGDME was used to fill the pores of the mortared pDCPD HIPE. The resulting porosity can be seen as the minimum value, because small pores in the nanometre range can be quite difficult to fill with organic solvent. For a better estimation, removing the air under reduced pressure prior to the solvent filling would be necessary. This would, however, require finding or building a suitable setup and therefore was not performed as the received values are an acceptable estimation of the overall trend.

Surface area and pore diameter were both analysed using nitrogen adsorption analysis. While the first takes the whole range of pores present into account, the latter (calculated using BJH), only analyses pores in the meso- or macroporous range (> 2 nm). Therefore, the average pore diameters mentioned in Table 7 do not take the certainly high amount of micropores into account and are all in the same range at the lower detection limit. This is also the case for the sample heated to 1100 °C, which has similar characteristics as the materials heated to 900 °C using different heating programs. While the mass loss is equal to the sample heated to 900 °C twice (two hours for carbonisation, two hours for activation), bulk density, porosity and surface similar to the material heated to 900 °C for two and then one hour. Other carbonisation programs at 1100 °C were not possible, since all the material was consumed throughout the process.

For all the samples discussed in this section, the morphology was retained as the cavities and windows are still nicely visible in SEM images (depicted in Figure 28). The pore size does not change throughout the heating step and therefore all materials regardless of the heating time or temperature look similar.

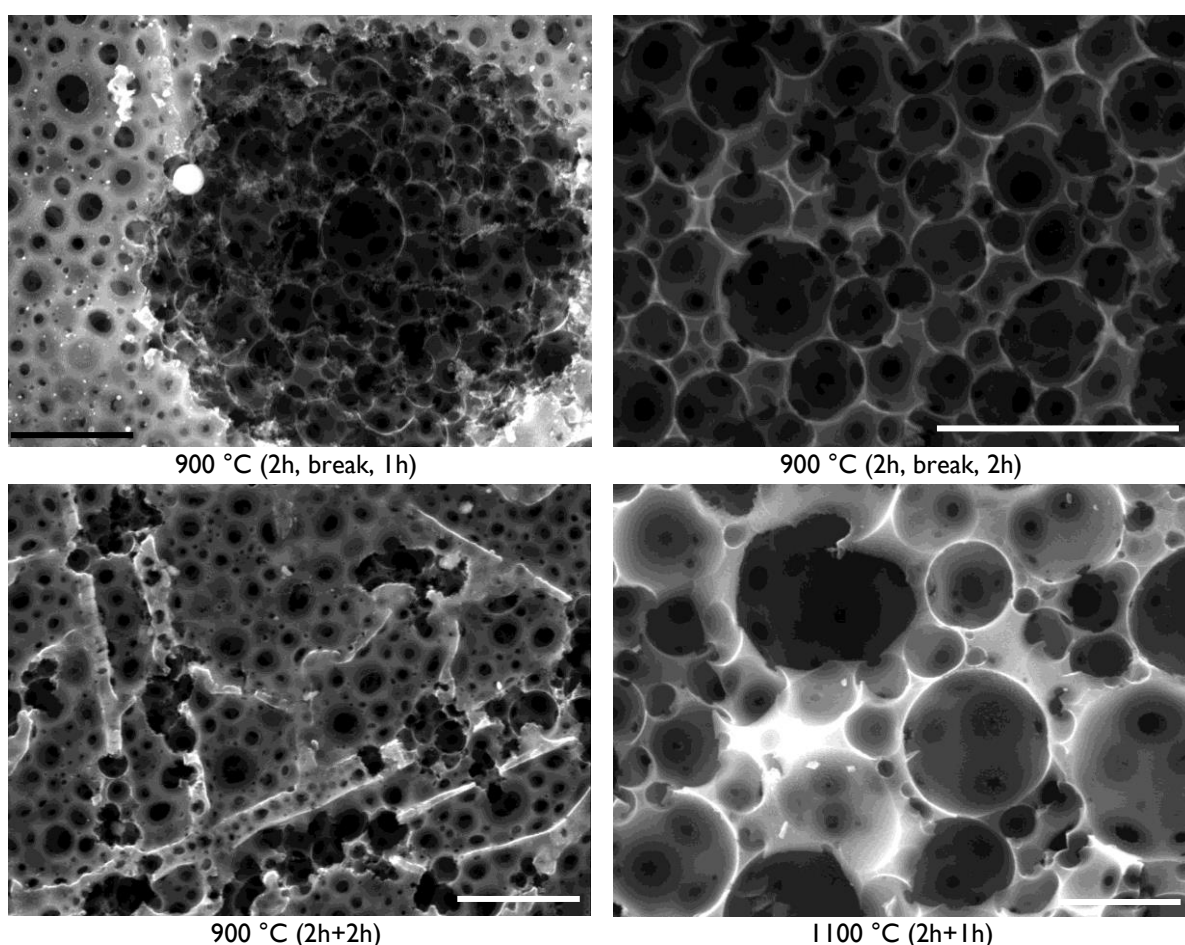


Figure 28: SEM images of the pDCPD HIPE materials activated at different temperatures for various time periods; scale bars correspond to 10 μ m.

Only the material heated to 1100 °C seems to have bigger pores, but here the reason can be found in the synthesis of the monolith, where 5 instead of 7 wt% surfactant were used. The surface of the pDCPD HIPE discs (both images on the left hand side) looks slightly different compared to the depicted cracks (both pictures on the right hand side), but the open porosity of the material is nicely visible in all images.

Subsequent to the heating step, all materials nearly solely consist of pure carbon and are conductive enough for electrochemical testing. First, cyclic voltammetry was performed with all four synthesised materials. For that purpose, the active material was discharged by applying a constant potential of

50 $\mu\text{V s}^{-1}$ using lithium-iron phosphate as counter and reference electrode. Theoretically, as already mentioned in the introduction, the formation of the discharge product Li_2O_2 occurs at 2.96 V *vs.* Li/Li^+ . Practically it takes place at slightly lower potentials and varies depending on the overpotential. This can be influenced by the applied voltage, the used cathode material and the battery environment. As visible in Figure 29b, all samples show a current density peak onset below ~ 2.75 V *vs.* Li/Li^+ . This onset implies two things: a suitable electrical conductivity of the material and the formation of Li_2O_2 . Both parameters indicate that a suitable cathode material is tested. Only for the sample carbonised and activated at 900 °C without an interim cooling step (blue curve) and the carbon black reference material (KB, black curve), the current decreases after the first peak. All other materials show a second peak. Here, it seems that additional reactions (like lithium intercalation) take place at voltages slightly above (violet curve) or below (both green curves) 2.4 V. The reached current density differs from 0.5 mA cm^{-2} (carbon reference) and 1.8 mA cm^{-2} (carbon activated at 900 °C for two hours). Although cyclic voltammetry is a quick and easy method to gain information about various materials, normally the weight of the active material is not taken into account when discussing the data. This is also true for the CV shown in Figure 29b, where the potential is correlated to the current density. The area below the current density peaks corresponds to the capacity of the tested materials giving a first indication about the capability of the material. But again, the weight of the active material is not taken into account.

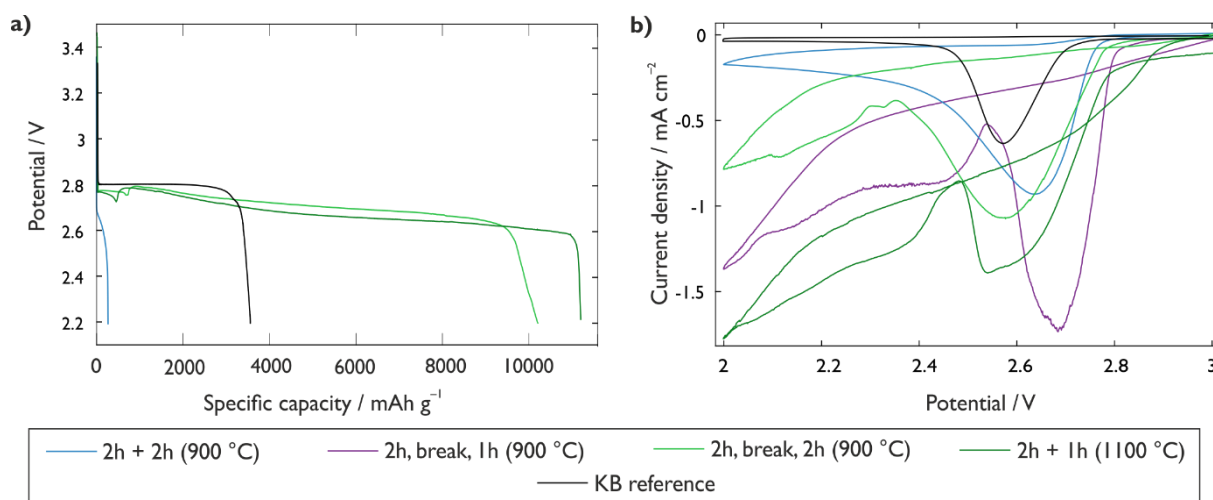


Figure 29: Electrochemical cycling of differently activated pDCPD-HIPES; a) galvanostatic discharge with 70 mA g^{-1} using 1.0 M LiNO_3 in DMAc in the electrolyte; b) cyclic voltammetry using the same setup at a scan rate of 50 $\mu\text{V s}^{-1}$.

For that purpose, the materials were also tested by discharging them galvanostatically at a constant current of 70 mA g^{-1} , Figure 29a. The corresponding current is removed from the cell until a potential limit, which was set to 2.2 V *vs.* Li/Li^+ , is reached. If Li_2O_2 is formed, a plateau in the range of 2.7-2.85 V *vs.* Li/Li^+ is visible during that time period. Combined with the applied current and the amount of active material, this time period is used to calculate the reached specific capacity, given as the x-axis, which directly correlates to the amount of Li_2O_2 formed during discharge. All materials except the one heated to 900 °C for two hours and afterwards one hour (violet curve, 2 h, break, 1 h), resulted in reproducible curves. While the sample, which also looked differently in the cyclic voltammetry experiment (blue curve), only resulted in small specific capacities below 500 mAh g^{-1} , both other synthesised products had capacities close to (light green curve) or above 10 000 mAh g^{-1} (dark green curve). Because those two materials also had concerning high surface areas and open porosities, both were investigated further.

After deep discharge, the cathode material was analysed *via* SEM imaging, Figure 30a. On the top right side of the picture, the HIPE structure is still visible, while the rest of the surface is completely filled

with discharge products. EDX results showed significant oxygen content of 10 to 50% at different positions on the surface. As Li cannot be analysed using EDX, the oxygen content can be an indication for the Li_2O_2 formation but cannot be taken for certain.

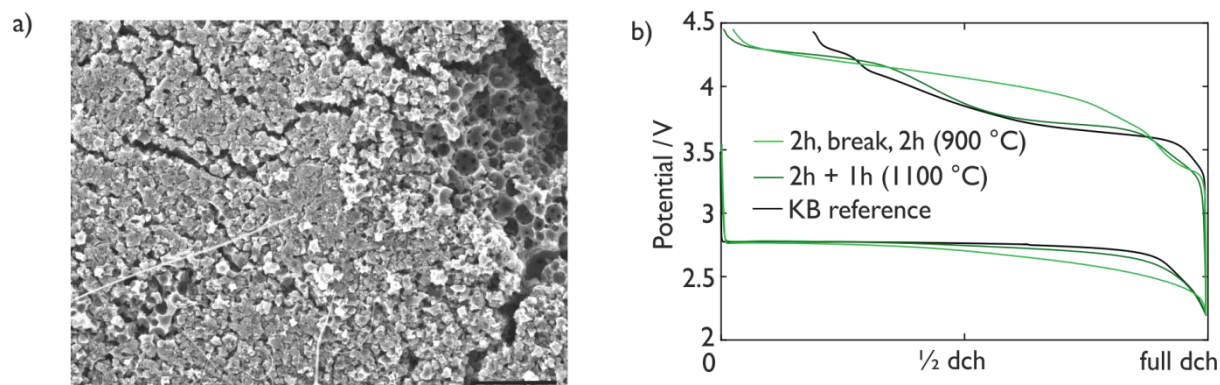


Figure 30: SEM and pressure cell analysis of the activated HIPEs; a) SEM image of a washed cathode after full discharge of the cell (scale bar corresponds to 20 μm); b) discharge/charge curve of two activated HIPEs compared to a carbon reference, cycled with 100 μA using 1.0 M LiNO_3 in DMAc as the electrolyte.

To further confirm that the high discharge capacities correspond to the formation of Li_2O_2 , the discharge was monitored with a pressure cell during cycling, Figure 30b and Figure 31. As mentioned above, both materials with really high discharge capacities in the Swagelok[®] type batteries were tested and compared to KB, a porous carbon black material. Different absolute capacities were achieved and for better comparison all graphs were normalised. While the KB electrode performed similarly in the pressure cell as in the Swagelok[®] setup and reached capacities of approximately 4000 mAh g^{-1} with the chosen electrolyte, the activated HIPEs only achieved a mere fraction of their original capacity. One problem was the unreasonably high absolute capacity, which resulted in a pressure decrease of the cell below 0.6 bar and a thus induced cell death. By decreasing the amount of active material used for cathode fabrication, the capacity could be increased to approximately 20% of the capacity obtained with the Swagelok[®] cell setup. During discharge all three materials experienced plateaus in the same potential range. While the potential stayed rather constant for the KB material, both activated HIPE materials experienced an earlier potential loss, which was more pronounced for the material carbonised at 900 °C. On charge, the materials differ significantly, but as various reactions can occur, the results should not be interpreted too much. Nonetheless, difference in the charge potential is obvious, as the KB reference and the carbonised HIPE activated at 1100 °C (dark green curve) both started at a charging potential of approximately 3.5 V *vs.* Li/Li^+ and only at about half charge polarised to potentials above 4 V *vs.* Li/Li^+ . The material activated at 900 °C (light green curve), on the other hand, experienced significant overpotentials nearly from the beginning of charge. For both activated HIPEs (green curves), full recharge was possible while the KB reference triggered the potential limit of 4.5 V at approximately $\frac{3}{4}$ of charge.

The changes in pressure and, related thereto to the oxygen consumption and evolution are depicted in Figure 31. In Figure 31a, the molar flux of oxygen evolved/consumed is compared with the electron flux of the cell. As two electrons are needed for the reduction/oxidation of one oxygen molecule, the theoretical molar flux of the oxygen is at half the electron flow. The same results, but cumulated throughout the cycling, are depicted in Figure 31b. Here, the cumulative moles of oxygen were multiplied by two for a direct comparison with the cumulative electron flow. Both representations show that during discharge the ratio of consumed oxygen to e^- follows the ideal value of two. The oxygen flux is, in all three cases, nearly a straight line. During charge, all three materials show less ideal behaviour. Starting with the oxygen flux, left handed graph, the KB reference (black curve) has a slightly

decreased flux at the beginning, increases during the charge process but decreases again at the end. One reason for this behaviour could be that the potential limit was reached. This is also depicted in the right handed image, where a decrease in the cumulated moles of oxygen is visible. Before that drop, the slope of the graph is already significantly lower than for the e^- used for oxidation.

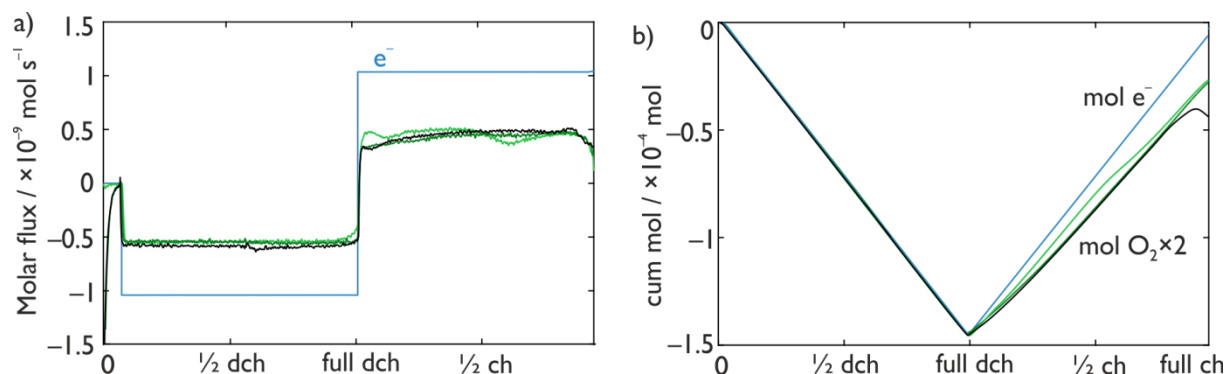


Figure 31: Pressure measurement analysis of the activated HIPEs with 1.0 M LiNO_3 in DMAc as electrolyte, cycled with 100 μA ; a) molar flux of the gaseous oxygen, calculated from the pressure change; b) deviation of the oxygen consumption/evolution from the theoretical value of $2 e^-/\text{O}_2$ during discharge and charge.

While the material heated to 1100 $^\circ\text{C}$ (dark green curve) behaves similarly for most of the charge, here no pressure drop at the end of charge is visible. The sample carbonised and activated at 900 $^\circ\text{C}$ (light green curve) results in the same oxygen to e^- ratio, visible due to the same final position in Figure 31b. During charging, however, the material activated at 900 $^\circ\text{C}$ in the beginning experiences increased oxygen evolution, which decreases significantly at $\frac{1}{2}$ charge.

Summing up, a highly porous carbon material was synthesised, which maintained the initial morphology of the pDCPD HIPE. Different carbonisation/activation conditions resulted in slightly varying characteristics of the materials; high temperatures and long activation resulted in samples most promising for the application in Li- O_2 batteries.

Comparison of pDCPD Samples to other Carbon Based Cathode Materials

The true significance of the synthesised material can be seen by comparing it to two commercially available carbon based active materials and a solely carbonised, but not activated pDCPD sample, Figure 32.

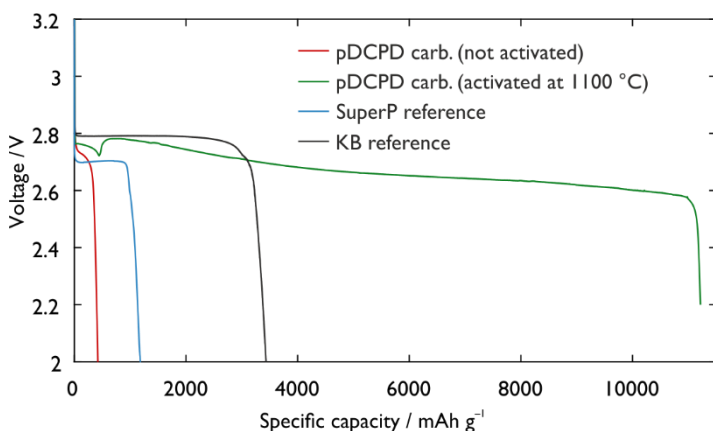


Figure 32: Galvanostatic discharge of four different carbon materials with 0.1 M LiNO_3 in DMAc as electrolyte. Carbonised pDCPD poly-HIPE materials not activated and activated are compared with two commercially available carbon materials, KB and SuperP.

By activation of the pDCPD polyHIPE, the 'roughness' of the material (=micro- and mesoporosity) is significantly increased which is visible regarding the increase in surface area. The macroporosity visible *via* SEM analysis stays approximately the same before and after the activation step. While simply

carbonised materials (red curve) have a surface area in the range of approximately 10-20 m² g⁻¹, by CO₂ treatment (green curve) this value can be increased to 800-1000 m² g⁻¹. This difference seems to have a significant impact on the discharge capacity of the two materials with 400 mAh g⁻¹ and 11 000 mAh g⁻¹, respectively. This impact is also obvious when comparing both commercial carbon materials with the surface area as the main difference; KB (black curve) obtains more than double of the specific capacity of SuperP (blue curve).

But also the morphology in the μm range strongly influences the achievable capacity. KB, with a surface area of approximately 1300 m² g⁻¹, has an even higher roughness than the carbonised and activated pDCPD material. However, the reached capacity of the activated pDCPD is about two to threefold higher than for the commercial carbon material. The reference material consists of particles in the low μm to nm range agglomerating on the steel grid when used as active material. Although having a high surface area, there are no macro pores capable of storing a high amount of Li₂O₂ without breaking. The possibly resulting loosened electrical contact could lead to a potential drop to the set limit of 2 V *vs.* Li/Li⁺. The polyHIPE material, on the other hand, may be able to maintain good electronic conductivity throughout the whole discharge process.

In conclusion, it can be said that there are different possibilities to obtain DCPD based polymers with various morphologies and porosities. The use of a porogenic solvent in the DCPD polymerisation resulted in different surface morphologies, but lacked high porosities due to significant shrinkage during drying. *Via* high internal phase emulsion, the porosity of the polymers could be tuned and the surface area was increased in an activation step. Also the combination of both techniques was analysed, but shrinkage destroyed the HIPE structure. Furthermore, despite high capacities, the problem with the side product formation, as a main drawback of all carbon based electrodes, still remains in activated pDCPD HIPEs.

3.3 Titanium Containing Cathode Materials

The element titanium is widely distributed in the earth's crust, has a low density and is stable against corrosion and high temperatures. Also its chemical compounds have many useful characteristics. TiC, for instance, is electrochemically and chemically stable over a wide voltage range and has a sufficient electrical conductivity ($3 \times 10^7 \text{ S cm}^{-1}$).¹³⁹ Up to now, it lacks the porosity necessary to obtain high capacities. To synthesise a stable and porous network, it was built on the experience gained through the pDCPD preparation. Additionally other approaches leading to a Ti-based porous cathode starting from TiO_2 nanoparticles or electro spun fibres containing a Ti precursor were pursued.

3.3.1 Different Routes to Ti Containing Materials

First of all, various previously reported routes to a porous, Ti containing material were investigated. These routes include TiO_2 nanorods and other non-stoichiometric Ti-containing compounds as well as TiO_2/TiC prepared *via* electrospinning; the resulting materials were analysed using SEM imaging, XRD, EDX and battery testing.

TiO₂-based Materials

Titanium dioxide is easy to prepare and a versatile material, due to different crystal structures and slight changes in the exact Ti/O ratio, which introduces electronic conductivity. Different preparation methods were tested in this work and the resulting materials were tested in Li-O₂ cells.

Purchased TiO_2 nanoparticles of two different sizes, 5 nm and 20 nm, and slightly different morphologies were heated to 400 °C and 800 °C under argon/air atmosphere. The goal was to provoke either a change in morphology or in the Ti/O ratio. In all cases, the materials mass did not change significantly during the heating process, which implies that only the modification but not the chemical structure is changed during the process. If TiO_{2-x} had formed, the molecular mass would have been lowered and therefore the total mass of the material would have decreased. Also the particle size and appearance are retained; see the exemplary SEM image in Figure 33a, showing the 5 nm sample heated to 400 °C. The agglomerated nanoparticles were easily visible in all analysed samples.

Before the heating experiments, the nanoparticles with a size of 5 nm solely consisted of anatase, the bigger particles (20 nm) contained rutile and anatase in a ratio of approximately 1:4. The transition of anatase to rutile only takes place at temperatures higher than 400 °C and therefore the samples heated to that temperature still consisted of the same anatase/rutile ratio. The only difference visible in the XRD was the increase of crystallinity after the samples were heated. Crystallinity increases, because the TiO_2 moieties can slightly change position at elevated temperatures. The diffraction patterns of the 20 nm sample heated to 400 °C and 800 °C under air and the 5 nm sample heated to 800 °C are depicted in Figure 33b and compared to anatase and rutile reference patterns. When the samples were heated to 800 °C, which is above the transition temperature from anatase to rutile, the morphology of the materials changed significantly. While all the anatase is converted to rutile in the bigger particles, with about 20-30% (air or Ar) a significant ratio of the material still has the anatase structure in the 5 nm nanoparticles.

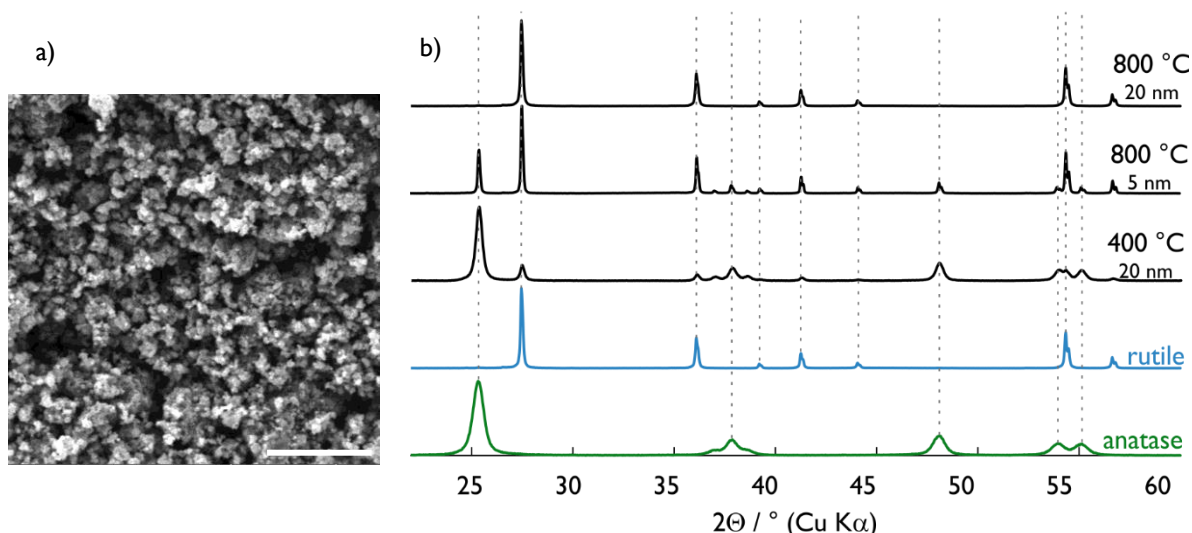


Figure 33: a) SEM image of the 5 nm sample heated to 400 °C under argon. The particle size visible in the image is the size of the agglomerates formed by the nanoparticles. The scale bar corresponds to 10 μm; b) XRD results from three different samples heated under air compared with both most common TiO₂ modifications.

Altogether, five different anatase/rutile ratios could be obtained which were all tested electrochemically using cyclic voltammetry. Results of the samples heated to 800 °C and 400 °C, respectively, together with a pure carbon reference (KB) are depicted in Figure 34. The most important feature is the missing signal at around 2.6 V *vs.* Li/Li⁺ of almost all TiO₂ samples. Only the pure rutile material (20 nm to 800 °C under air) has a small increase in current at that potential range. Two other samples, both mainly consisting of rutile (20 nm to 400 °C) have a defined current maximum at about 2.1 V with an onset at 2.4 and 2.6 V *vs.* Li/Li⁺. This could correspond to Li intercalation. The currents achieved for all the materials heated to 800 °C are drastically lower compared to the carbon reference. Overall, the CV results suggest that the prepared TiO₂ samples are not suitable as cathode materials for the Li-O₂ battery due to insufficient conductivity. Additionally it can be noted, that small parts of rutile first increase the conductivity and result in defined signals before a too large content (at least 70% for the samples heated to 800 °C) results in nearly insulating materials with very small peak currents.

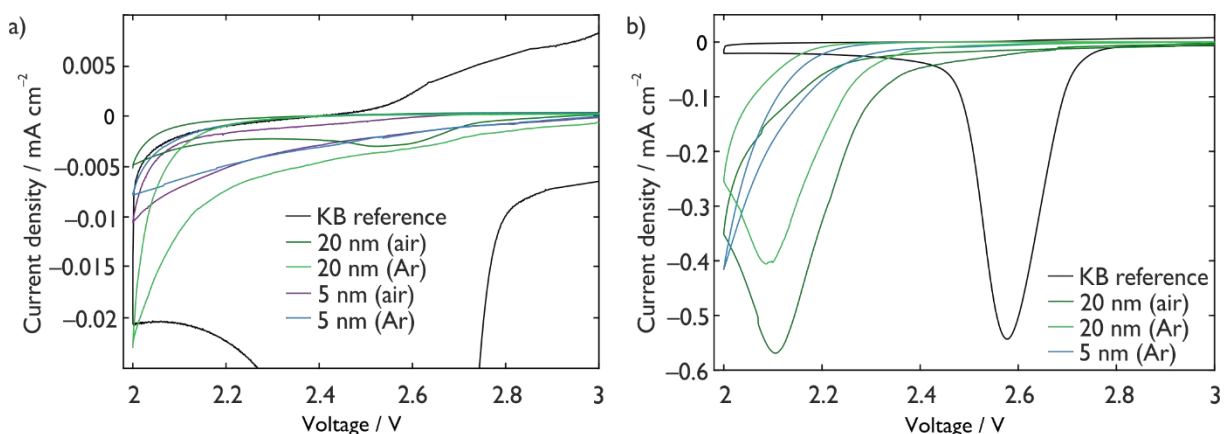


Figure 34: Cyclic voltammetry of the samples with 0.1 M LiClO₄ in TEGDME as electrolyte (cycled with 50 μV/s) compared to a porous carbon black electrode; comparison of the nanoparticles heated to 800 °C (a) and 400 °C (b).

The electrochemical activity of different titanium oxides and non-stoichiometric TiO₂ is already known. To obtain TiO_{2-x} materials, a synthesis route published by Sun *et al.*¹⁵² was followed to obtain rutile nanorods. Starting with TiN particles, as visible in the centre of Figure 35, different titanium dioxides can be synthesised.

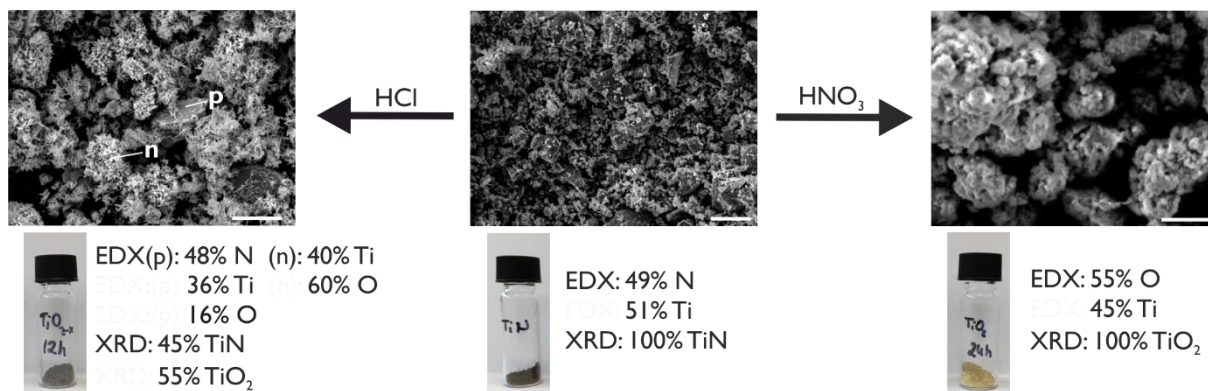
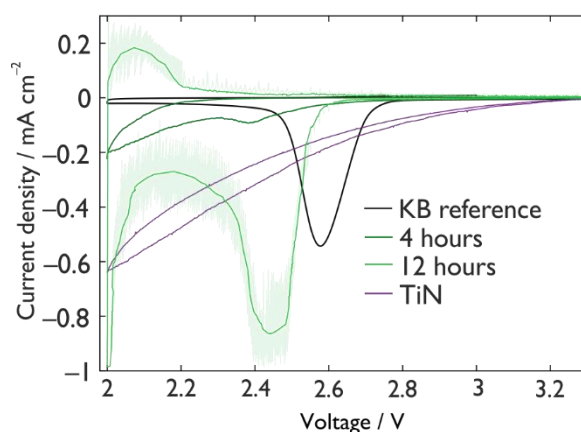


Figure 35: Formation of TiO_2 particles from TiN ; SEM images, EDX and XRD of the products resulting from the addition of different acids are given; scale bars correspond to 10 μm .

The formerly brown powder forms a dark grey solid after 12 hours when stirring with HCl at 180 $^\circ\text{C}$ in an autoclave. The SEM images show a significant change in the size and morphology of the material. While the TiN consists of small particles, the morphology partly changes to small needles of approximately 3-5 nm. With increasing the heating time (2 h, 4 h or 12 h), the content of needles increased. EDX measurements suggest, that while the particles present still consist of nearly 50% N similar to the starting material, the needles only contain Ti and O. While the samples turn to a lighter grey with increasing synthesis time, the resulting ratio of TiN to TiO_2 analysed by XRD does not follow a specific trend and is at about 1:1 for all materials. In contrast, when TiN was heated in HNO_3 , a completely different structure was obtained. Small, agglomerated particles in the range of a few hundred nanometres can be observed by SEM; these particles consist exclusively of rutile. All samples were analysed without prior sputtering with a gold target. This resulted in difficulties with the SEM imaging like low resolutions and blurring of the pictures which indicate low conductivity of the pure TiO_2 material. Therefore, only materials prepared by addition of HCl were tested in the Swagelok[®] setup. The results, referenced against the TiN starting material and a porous carbon reference (KB), are depicted in Figure 36.

Figure 36: Cyclic voltammetry of two different TiO_2/TiN mixtures, a porous carbon black and a TiN reference; all measurements were obtained with 0.1 M LiClO_4 in TEGDME as electrolyte. For the measurement of the 12 h sample, a mean value is given to guide the eye.



While the carbon reference shows the expected current increase in a voltage range of 2.7-2.5 V *vs.* Li/Li^+ , the current of the TiN material increases steadily without forming a defined signal. Both synthesised materials (green lines) show a signal in a slightly lower potential range. While the current increase for the material stirred for four hours is very low, the material heated for 12 hours (light green line) is in the same range as the carbon reference. However, the electrode consisting of the TiO_2/TiN mixture had about five times the mass of the carbon electrode and therefore only about one fifth of the carbon materials capacity.

Both materials synthesised from TiN and the heat treated TiO₂ nanoparticles do not show suitable properties for the use as Li-O₂ cathodes. While TiO_{2-x} may be a suitable compound, it was not possible to synthesise this material and the TiO₂/TiN mixtures obtained instead did not meet the expectations.

Electrospun Fibres

Another way to obtain porous Ti-containing materials is by electrospinning. Polyvinylpyrrolidone (PVP), titanium(IV) n-butoxide (TiBO) and furfuryl alcohol (FA) were used as carrier polymer, Ti- and carbon-source, respectively and the solution was mixed following the instructions of Fong *et al.*¹⁵³ Acetic acid was added to the spin dope to start the polymerisation of the FA as well as the sol-gel process of the Ti-source. In contrast to the literature, a different electrospinning appliance was used. The application of the spin dope was performed using rotating fibres instead of a syringe. This change required both a higher potential and a smaller working distance for the spinning process, resulting in a few problems during the electrospinning. A gelation of the solution occurred after a few minutes, possibly caused by the increase of the potential from 15 kV to 75 kV. This high potential may have induced a sol gel process of the TiBO before the actual spinning and resulted in a lower Ti concentration of the final fibres as the Ti material is not spinnable any more after the sol gel process. The solution/gel mixture then was not spin-able anymore and the application setup had to be cleaned and reinstalled every few minutes. Due to the smaller working distance, not all of the DMF evaporated during the spinning process and the collected fibres still contained a high amount of solvent. This led to the agglutination of the fibres and a significant loss of surface area detectable optically and *via* SEM analysis. By varying the amount of solution, the voltage or the rotation of the rotating fibres, neither the gelation nor the agglutination of the fibres could be prevented (for the exact parameters see page 87).

Both the obtained “fibres” and the gelled spin dope are depicted in Figure 37 before and after the carbonisation process. Before (on the left hand side of the figure), both materials have a light (“fibres”) or dark (gel) orange colour and are conductive enough for acceptable SEM measurements. The gelled spin dope does not contain any visible porosity, while some fibres are visible at the electro spun material. Interestingly, no Ti can be detected in both cases using EDX analysis and the ratio between carbon and oxygen is similar. We therefore presume that the Ti is present in the bulk but not at the surface. The existence of titanium in the sample can be proven by applying the heating program published by Fong *et al.* After a plateau at 325 °C, the materials are heated to 1350 °C for 12 hours. In that time period, the PVP should vanish, the FA-polymer should decompose to C and react immediately with the formed TiO₂ to TiC, both in its crystalline and amorphous form. Due to problems with the tube furnace, the maximum temperature was set to 1350 °C instead of 1400 °C but other than that the proposed procedure was followed. However, for both tested materials, the initial partly fibrous structure could not be maintained during the heating process, as seen in Figure 37. While the electro spun material only contained oxygen and titanium after carbonisation and resulted in a colourless solid; the gel was greyish/black after carbonisation and a lot of carbon was still present in the obtained material. Both materials seemed to be shrunk/ melted during the heating step which could result in the observed surface structure. Although the O/Ti ratio measured *via* EDX varies from the theoretical ratio of 2:1, according to the XRD pattern the colourless solid contains very crystalline rutile without any other Ti_xO_y modifications visible.

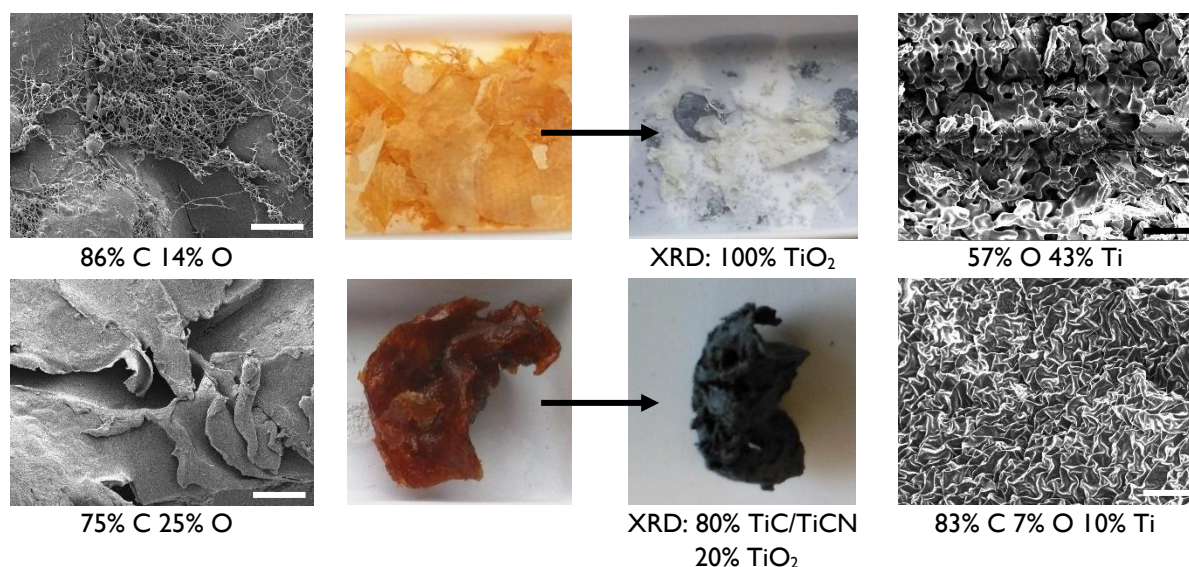
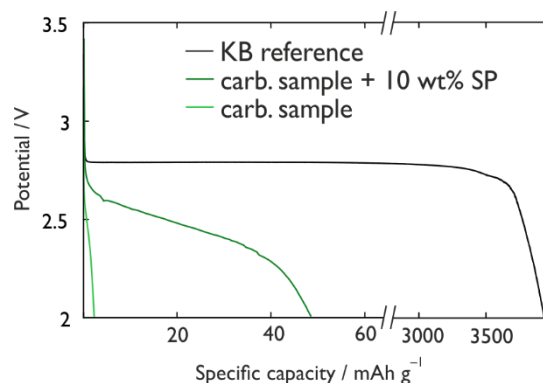


Figure 37: Carbonisation of the electro spun materials and comparison of the materials using SEM imaging, X-ray diffraction and EDX analysis; on the left hand side are the spun fibres (upper part) and the remaining gel (lower part) before, and on the right hand side after carbonisation at 1350 °C; scale bars correspond to 20 µm.

The gelled spin dope, on the other hand, contains 80% TiC/TiCN in a ratio of 1:1 and 20% of TiO₂. The total carbon content of 80% leads to the assumption that amorphous carbon, which cannot be detected using XRD, is also a main part of the resulting material. The diffraction pattern anyhow shows rather broad and small signals, which suggests a poorly crystalline material.

Despite the low porosity, conductivity is a vital parameter for a cathode material and was tested *via* GCPL analysis. While the low conductivity of the electro spun material is already visible in the poor resolution of the SEM image, the carbonised gel was tested in Swagelok® cells. Again, the material was compared to a carbon (KB) reference and the results are depicted in Figure 38.

Figure 38: Galvanostatic cycling at 70 mA/g using 0.1 M LiClO₄ in TEGDME as electrolyte; results of a porous carbon black electrode and the carbonised material containing TiC are depicted.



While the carbon material has a specific capacity of nearly 4000 mAh g⁻¹, the pure carbonised gel only results in capacity of approximately 5 mAh/g. Also, no defined discharge plateau is visible in the light green curve. To increase the conductivity of the material, 10 wt% SuperP (SP) were added to the active material. With that mixture, the capacity could be increased tenfold to about 50 mAh g⁻¹, which is still unsatisfactory. Additionally, the discharge plateau was still not very pronounced and again carbon was present in the electrode which diminished the whole goal of synthesising a Ti-based cathode material.

Since optimizing the electro spinning solution and -setup would consume a lot of time, further tests were done with electro spun fibres prepared by Pardam nanotechnology. For that purpose, two different materials could be used for carbonisation tests. Both consist of an organic carbon source and a Ti-source, which is rutile in one case and Ti-spider (no further details provided by the company) in the other. While the rutile containing material (termed FCSP) consisted of fibres in the diameter range of

400 to 1000 nm and had a cotton like appearance, the spider containing sample (termed ELSP) with slightly smaller fibres (300-700 nm) looks like yellow paper (see Figure 39, left part).

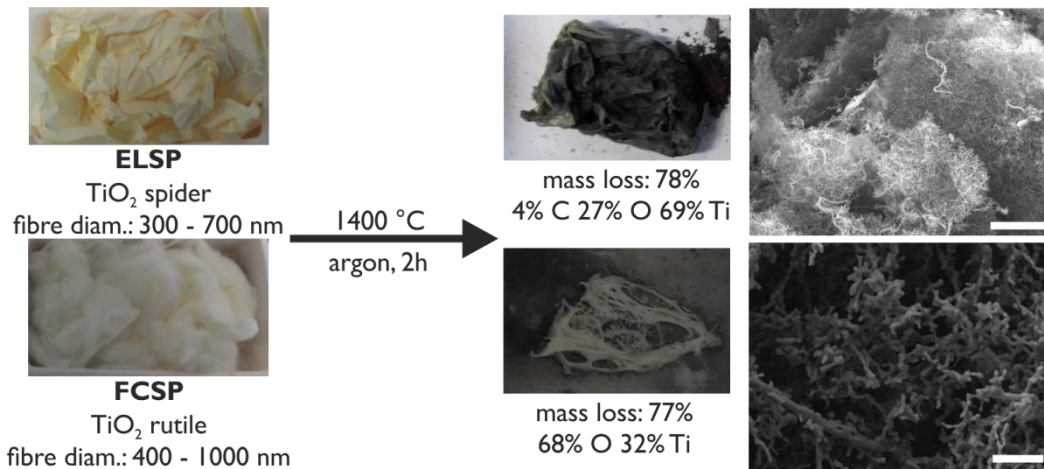


Figure 39: Carbonisation of both types of commercially available Ti containing fibres and the corresponding SEM and EDX results. Scale bars correspond to 20 μm .

To obtain TiC or a TiC/carbon composite, different heating programs were tested. In all cases, the heating programs were performed under inert conditions. First, similar programs as before with two plateaus at 325 $^{\circ}\text{C}$ and 1250/1350 $^{\circ}\text{C}$ were tested. However, in all cases pure TiO_2 was obtained and the fibres melted during the heating process. Only when applying high temperatures of 1400 $^{\circ}\text{C}$ without an intermediate plateau at 325 $^{\circ}\text{C}$, a black solid (visible on the right side in Figure 39) could be obtained after carbonisation. SEM images show that the fibre morphology of the material was preserved during the carbonisation instead of melting the FCSP sample. Both the EDX and the XRD results of that material confirm TiO_2 in the rutile modification as the only component present after the heating program. Nonetheless, the melting during the carbonisation is much less pronounced in comparison to the samples heated to 1350 $^{\circ}\text{C}$ or 1250 $^{\circ}\text{C}$. The ELSP material, on the other hand, still has, in addition to oxygen and titanium, some carbon present after the carbonisation.

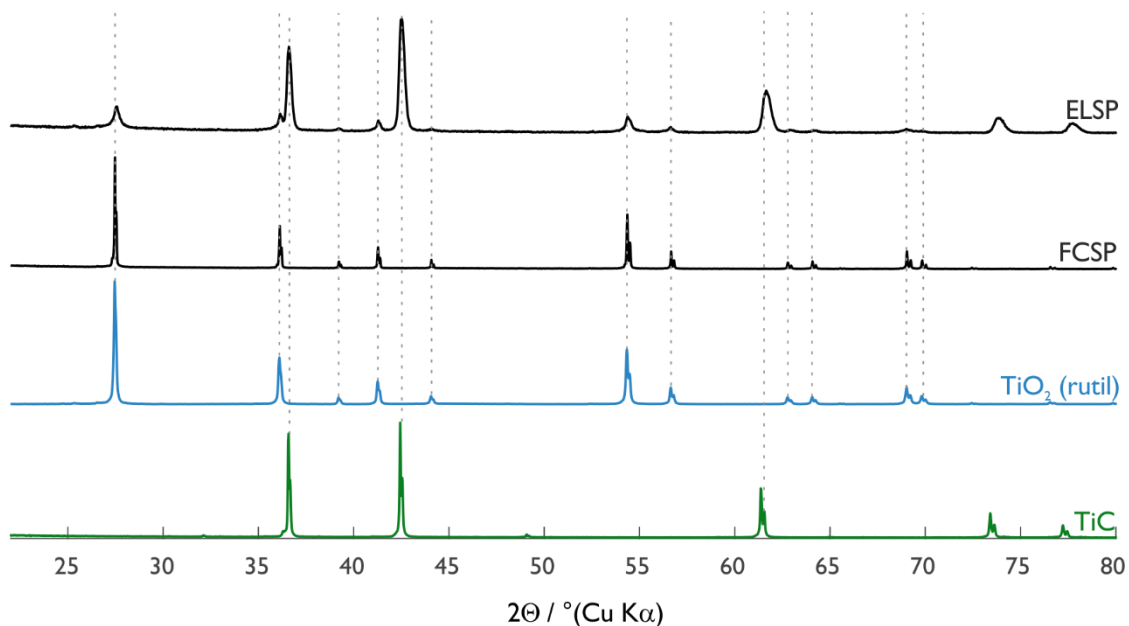
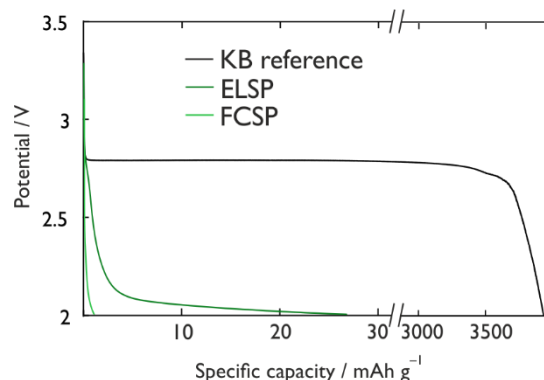


Figure 40: XRD data of the carbonised fibres compared to TiO_2 and TiC reference diffraction patterns.

When analysing the XRD patterns depicted in Figure 40, the crystallinity of the greyish/black material is significantly lower than that of the rutile FCSP. Although the pattern lacks sharp signals, the ratio of

TiC to TiO₂ is rather high with 76% to 24%. For further characterisation, both materials were tested electrochemically using galvanostatic cycling. The first discharge curves are depicted in Figure 41, where they are also compared to a carbon reference material (black curve).

Figure 41: Galvanostatic cycling of the two different carbonised fibres and the porous carbon black reference with a current of 70 mA g⁻¹; 0.1 M LiClO₄ in TEGDME was used as electrolyte.



The lack of a discharge plateau in the range of 2.8-2.6 V *vs.* Li/Li⁺ is very significant for both tested materials. Additionally, the obtained specific capacity is with below 5 and approximately 25 mAh g⁻¹ very low. Here, it may be assumed that no Li₂O₂ formed and the slight plateau at 2.1 V corresponds to Li⁺ intercalation. However, the missing carbon content of the FCSP material and the low crystallinity of TiC in the ELSP as well as the poor electrochemical performance of both materials are not very promising results for the use of these composite materials for Li-O₂ cells.

3.3.2 Titanium Precursors for a Polymerisation Route

As the previously discussed Ti containing precursors did not result in suitable cathode materials with desired conductivities, compositions, morphologies and surface areas, a radically different approach was pursued next.

The titanium should be introduced *via* an organometallic compound consisting of a titanium centre atom and organic ligands. Titanium isopropoxide (Ti(i-Pr)₄) is easily available, but its major drawback is its lack of polymerisable groups. Therefore, titanium-norbornene (Ti(Norb)₄) was synthesised in an alcohol interchange reaction using Ti(i-Pr)₄ and 5-norbornene-2-methanol (see Figure 42). With only isopropanol as side product, the product can be used without any purification steps. The Ti-O bond is very sensitive to moisture and can form Ti-hydroxides/hydrated Ti-oxides and therefore both Ti(i-Pr)₄ and Ti(Norb)₄¹⁵⁴ were stored under inert conditions.

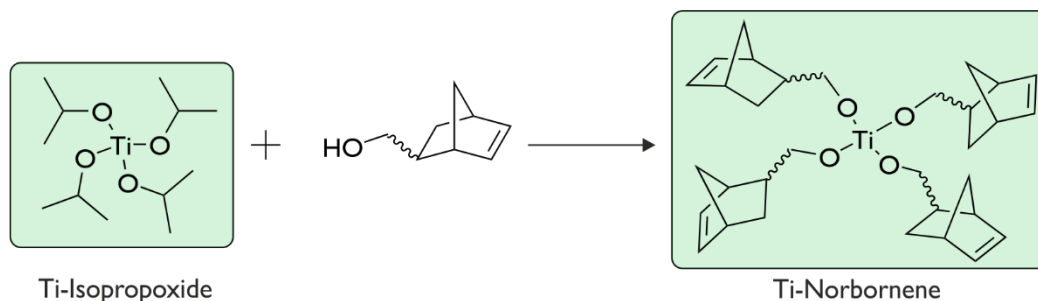


Figure 42: The investigated Ti-based compounds (green boxes); Ti(Norb)₄ was synthesised from Ti(i-Pr)₄ and norbornene-alcohol.

3.3.3 Ti-Norbornene based Polymers

Homopolymerisation of Ti-Norbornene

The double bonds in $\text{Ti}(\text{Norb})_4$ can be polymerised by ring opening metathesis polymerisation. The four equal ligands of the monomer lead to a highly branched polymer, depicted in Figure 43. The monomer-initiator-solvent (cyclohexanone (CHO)) mixture is cured in a Teflon[®] mould for two hours at 80 °C, giving an orange, solid but still flexible polymer. As the solvent must not evaporate during curing, only solvents with relatively high boiling points can be used. To subsequently remove this solvent, a solvent exchange with acetone is necessary before the polymer is dried. The mainly organic polymer is still insulating and has to be carbonised to obtain a conductive material which can be used in Li-O₂ batteries.

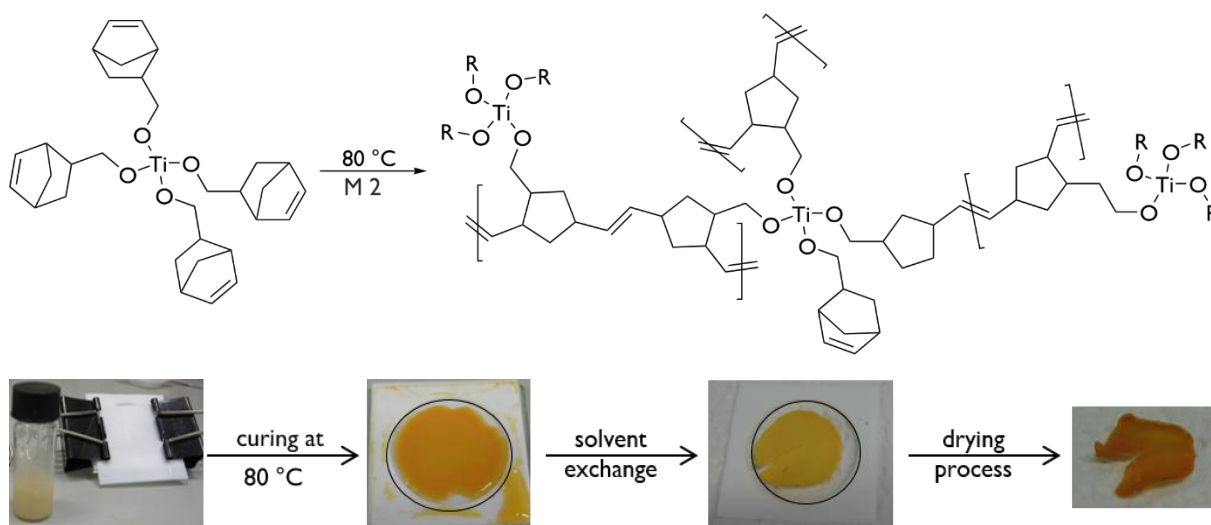


Figure 43: Polymerisation of the $\text{Ti}(\text{Norb})_4$ via ring opening metathesis polymerisation; the monomer is dispersed in CHO, cured in a Teflon[®] mould, immersed in acetone and dried.

The behaviour of the $\text{Ti}(\text{Norb})_4$ during heating under air and inert conditions (Ar) was analysed using thermogravimetric analysis (TGA). Changes in mass of the different samples are depicted in Figure 44. When heated in air, the final material still has 16% of the original mass, which corresponds to TiO_2 formed from the Ti of the sample and oxygen from the air. All the organic material appears to be burned away with that method. This also implies that all the Ti is preserved during the heating process. When the $\text{Ti}(\text{Norb})_4$ is heated under inert conditions both as the monomer and as the polymerised structure, significantly more material is left at the end with 22% and 24%, respectively. The final mass is thus similar, but the shape of the mass loss up to this temperature deviates significantly. While the monomer still has about 80% of its mass at 200/250 °C and the decrease afterwards is rather rapid, the mass of the polymer slowly decreases to 60% at 400 °C, before the mass loss is more significant. The melting point of the monomer seems to be in the range of 160-190 °C.

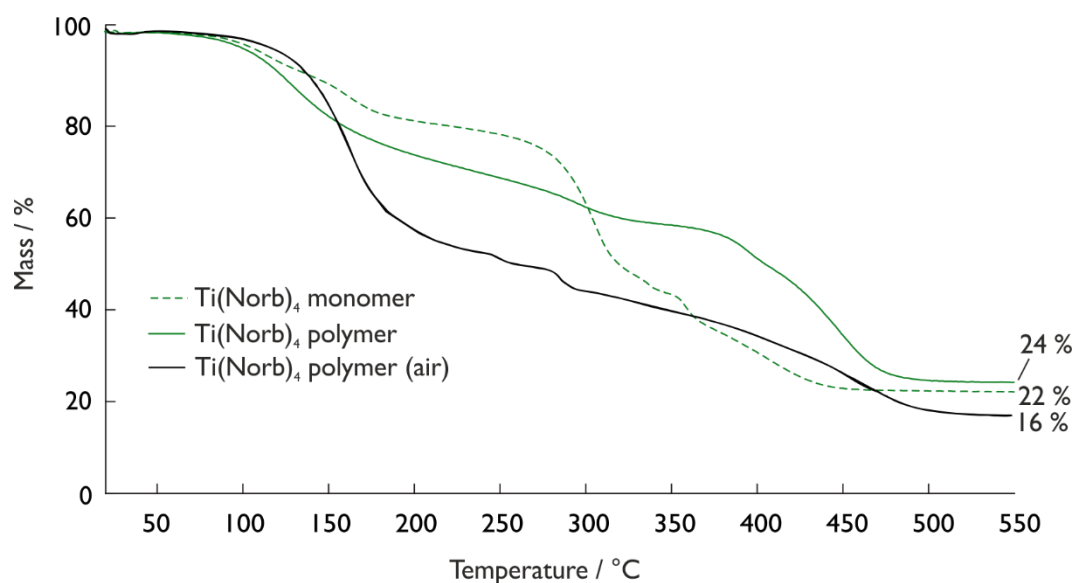


Figure 44: Thermogravimetric curves of different Ti(Norb)₄ samples; all heated with 10 K/min under Ar or air.

The mass loss during the heating process is hoped to an increase in porosity and surface area of the material. To increase that aspect, a porogenic solvent was added during the polymerisation. In that case, the porosity is already introduced during the polymerisation and only increased during the carbonisation due to the decrease of the carbon content of the Norb-ligand of the polymer.

In this work, the addition of two organic solvents, toluene and cyclohexanone, was tested for the Ti(Norb)₄ polymerisation. By varying the amount of solvent from 0.5:1 to 10:1 (solvent:monomer), the influence of the liquids could be analysed. Both solvents behaved similarly when added to the polymerisation. Up to a ratio of 5:1 (solvent:Ti(Norb)₄), the resulting monoliths were solid but suffered from significant shrinkage upon drying. When the solvent amount was further increased, it was not possible to obtain a disc suitable for further testing. Solvent exchange with acetone, as tested for the pure DCPD-materials, did only mitigate the shrinkage. As the SEM images of the samples carbonised at 1100 °C did not differ significantly regarding the amount of solvent used for the polymerisation, the amount of toluene/CHO was decreased to 0.5:1 or 1:1 (solvent:Ti(Norb)₄). One exemplary image is given in Figure 45, showing the porous structure of the sample.

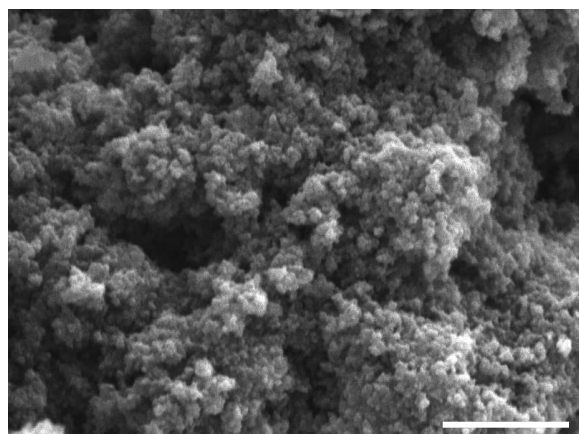


Figure 45: Ti(Norb)₄ and CHO (ratio during polymerisation was 1:1) carbonised at 1100 °C under argon; scale bar corresponds to 20 µm.

The material appears not to have any ordered or defined structure, neither at the surface, where only a little open porosity is visible, nor inside. The carbon content decreases throughout heating the sample to different temperatures under inert conditions, as visible in Table 8. As the absolute amount of titanium should stay constant throughout the whole process, the change in mass or C:O ratio can be calculated using energy dispersive X-ray (EDX) spectroscopy. The values derived by this way suffer

from significant uncertainty, but are important first observations of the sample composition. After polymerisation, the relative composition of C/O/Ti is 80/17/3 atomic percent (a%, cf. Table 8). The subsequent heating step under various atmospheres leads in all cases to a decrease in the carbon content and an increase in the titanium count. When samples are heated under air to 500 °C, the carbon content is approximately at 10% and cannot be detected any more at higher temperatures. Monoliths heated under N₂/Ar usually have more than 50 a% carbon when heated to 500/1100 °C, the exact ratios differ depending on the sample composition, the atmosphere and the heating rate. The decomposition of carbon seems to be quicker under N₂ and therefore all further heating experiments were performed under argon. Here, on the surface sometimes the carbon content is significantly lower than inside the sample, which is also visible by bare eye due to a brownish/grey colour of the sample instead of being completely black. When heating the material to 1400 °C, the whole monolith has a greyish colour and also EDX analysis does not detect a significant carbon content.

Table 8: EDX results (in atomic percent) from polymerised Ti(Norb)₄ carbonised under different conditions.

		C	O	Ti
1	after synthesis	80 a%	17 a%	3 a%
2	500 °C (nitrogen)	61 a%	27 a%	12 a%
3	500 °C (air)	11 a%	71 a%	18 a%
4	1100 °C (air)	-	64 a%	36 a%
5	1100 °C (Ar) – 1:1 toluene:Ti(Norb)₄	65 a%	5 a%	30 a%
6a	1100 °C (Ar) – 0.5:1 toluene:Ti(Norb)₄ inside	62 a%	30 a%	8 a%
6b	1100 °C (Ar) – 0.5:1 toluene:Ti(Norb)₄ surface	40 a%	51 a%	9 a%
7	1300 °C (Ar) – 3:1 CHO:Ti(Norb)₄	-	60 a%	40 a%
8	1320 °C (Ar) – 2:1 CHO:Ti(Norb)₄	-	70 a%	30 a%

When the Ti content is treated as a fixed value, the absolute amounts of both carbon and oxygen decrease during the heating process as the ratio of C or O to Ti changes in favour of the Ti. In inert atmosphere, carbon is released as CO/CO₂, depending on temperature. The gas evolution leads to a mainly open porosity and permeability of the resulting porous polymer. Although the tube furnace is evacuated and flushed with argon three times prior to use, it is still possible that traces of air/O₂ remain in the atmosphere. This, and possible leakage during the heating period, could be reasons for the partly high oxygen content in the samples. Why similar materials still result in significantly different C/O/Ti ratios, like samples 5 and 6a in Table 8, remains unclear with this analysis method.

In addition to the composition, also the chemical structure is important. Although samples 5 and 6 were treated similarly during the carbonisation step, the chemical structure of the resulting material varies a lot. Only the amount of toluene present during polymerisation differed. As visible in Figure 46, sample 6 only consists of rutile TiO₂, while material 5 contains both TiO₂ and TiC. However, also here the high TiO₂ content is inadequate for battery application. Furthermore, the TiC reflexes of sample 5 are considerably broader than the TiO₂ ones. This implies a rather low crystallinity of the TiC phases in the final material. When heated to 1400 °C, again, only TiO₂ is visible in the XRD diffraction pattern. It seems that too much carbon is removed during the carbonisation step, which then prevents the formation of a crystalline TiC phase. Here, the change of solvent to monomer ratio does to seem to have a significant influence in the resulting material, as both contain no TiC and also when measured using EDX only oxygen and titanium are visible. At temperatures below 1000 °C no TiC can be detected. In the representative diffraction pattern of the Ti(Norb)₄ polymer heated to 500 °C, a mixture of TiO₂ in the rutile (reference in blue) and the anatase form is visible. The crystallinity of the titanium dioxide is significantly lower in that sample than for the reference pattern and both materials heated to temperatures above 1000 °C.

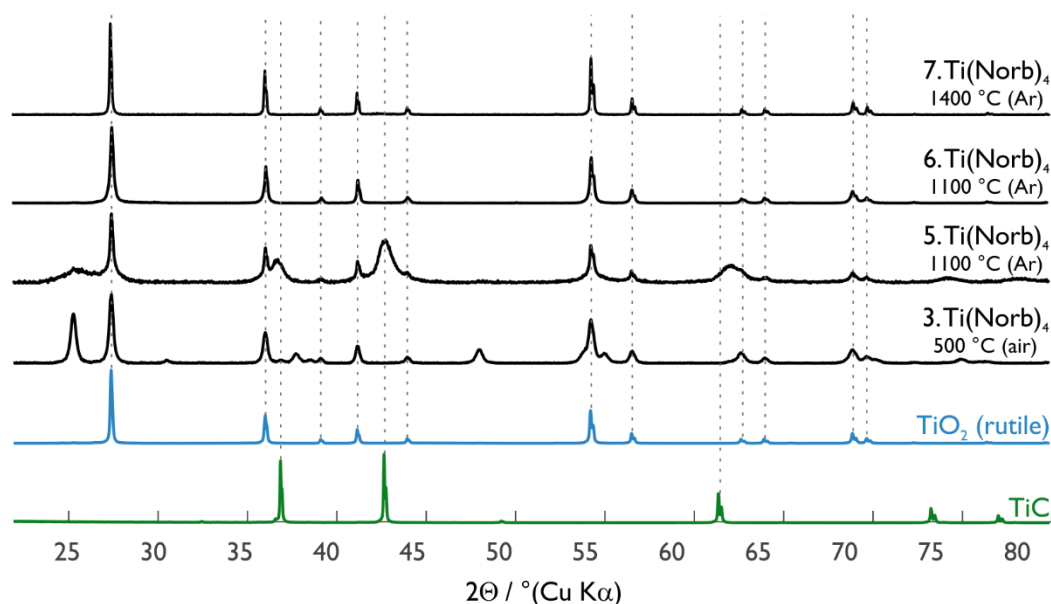


Figure 46: X-ray diffractions of different polymerised and carbonised $\text{Ti}(\text{Norb})_4$ samples compared to TiC and TiO_2 (rutile) reference patterns.

Altogether it can be said, that although $\text{Ti}(\text{Norb})_4$ can be easily polymerised in different solvents, the C:Ti ratio seems to be too low to guarantee a TiC formation during the heating step.

Different Copolymerisation Tests using Ti-Norbornene

With the addition of a co-monomer containing carbon, the carbon yield after the carbonisation step could be increased. During the carbonisation the additional organic material is partly burned away and forms pure carbon; thus it acts as a carbon source for forming TiC at temperatures above $1000\text{ }^\circ\text{C}$. To that end, both DCPD and norbornene were tested, as these materials can be co-polymerised using ROMP. The resulting materials were first analysed *via* thermogravimetric analysis to determine the change in total mass after a heating step. The results are depicted in Figure 47. The green and black curves are pure $\text{Ti}(\text{Norb})_4$ and were already discussed on page 48, whereas the others are copolymers with DCPD

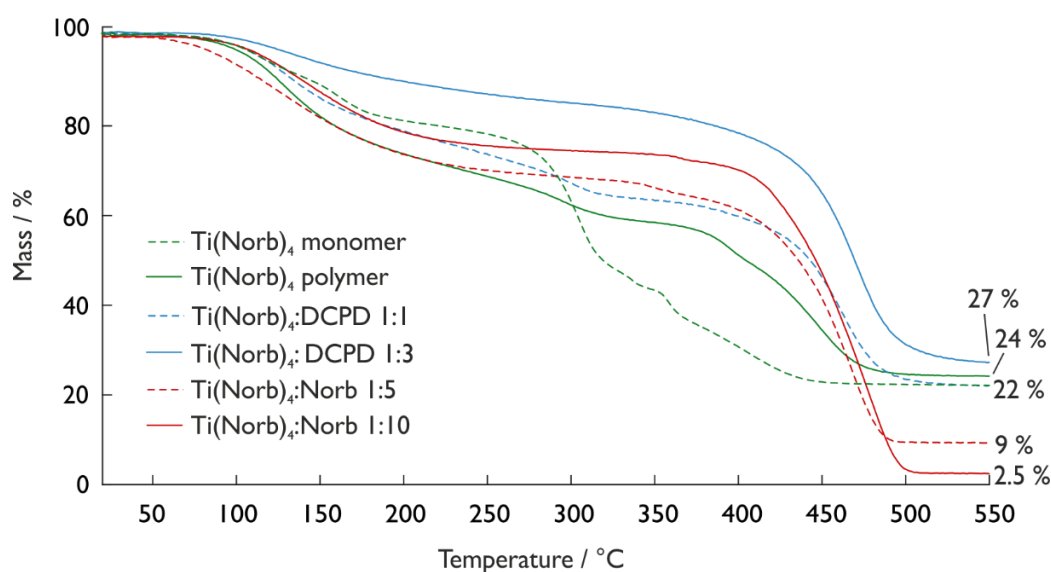


Figure 47: Thermogravimetric curves of both pure $\text{Ti}(\text{Norb})_4$ polymers and different copolymers heated under inert conditions (except ' $\text{Ti}(\text{Norb})_4$ polymer (air)' which was heated under air) with 10 K/min . Ratios are mass ratios.

Before carbonisation, for all co-polymerisations the absolute amount of titanium is much lower than for the pure $\text{Ti}(\text{Norb})_4$ polymer. The addition of DCPD seems overall to result in a similar residual mass after the heating to $500\text{ }^\circ\text{C}$ under inert conditions. In those samples, the total carbon yield is significantly higher than for the pure $\text{Ti}(\text{Norb})_4$ polymer as the Ti only accounts for 4.5% or 2% instead of 9% of the total polymer mass (blue curves) or norbornene (Norb; red curves). The copolymer with Norb, on the other hand, loses a lot of its mass during heating to $550\text{ }^\circ\text{C}$ and the remaining mass corresponds to pure TiO_2 without remaining carbon. A high amount of carbon still present after the heating step is, however, crucial to allow TiC formation above $1000\text{ }^\circ\text{C}$. Therefore, only the copolymer consisting of $\text{Ti}(\text{Norb})_4$ and DCPD was analysed further.

The monomers were mixed in different ratios and co-polymerised in the bulk. $100\text{ }\mu\text{L}$ toluene were added to dissolve both monomers. The resulting polymer discs, depicted in Figure 48 were carbonised at $1380\text{ }^\circ\text{C}$ under argon, as a TiC formation was observed at that temperature range for similar materials discussed in this work.

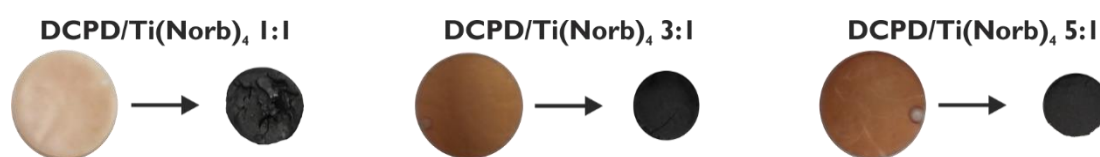


Figure 48: Copolymerisation of $\text{Ti}(\text{Norb})_4$ with DCPD using different monomer ratios; pictures before and after carbonisation at $1380\text{ }^\circ\text{C}$ for two hours under argon.

Before the carbonisation, all discs had an orange colour and could not be broken due to the still unoxidised pDCPD. The slightly opaque appearance of the sample with the ratio of 1:1 (DCPD: $\text{Ti}(\text{Norb})_4$) results from $\text{Ti}(\text{Norb})_4$ particles, which were not fully soluble in the amount DCPD used. Higher DCPD ratios led to a complete dissolution of the $\text{Ti}(\text{Norb})_4$ and transparent discs. As the polymerisation was performed with hardly any solvent, the resulting polymers were rather dense and lacked significant porosity. Therefore, the carbonisation step was performed without prior oxidation of the samples, which changed the former smooth surface to a cracked one. The discs shrank significantly, turned black and became brittle during the carbonisation step. All three samples, looking quite similar at first glance, have a completely different morphology and molecular composition, see Figure 49 and Table 9. For the intended application, a porous material consisting of carbon and TiC, without the presence of TiO_2 , is needed. The sample with the highest ratio of DCPD (SEM image on the right side of Figure 49) has no visible macro porosity.

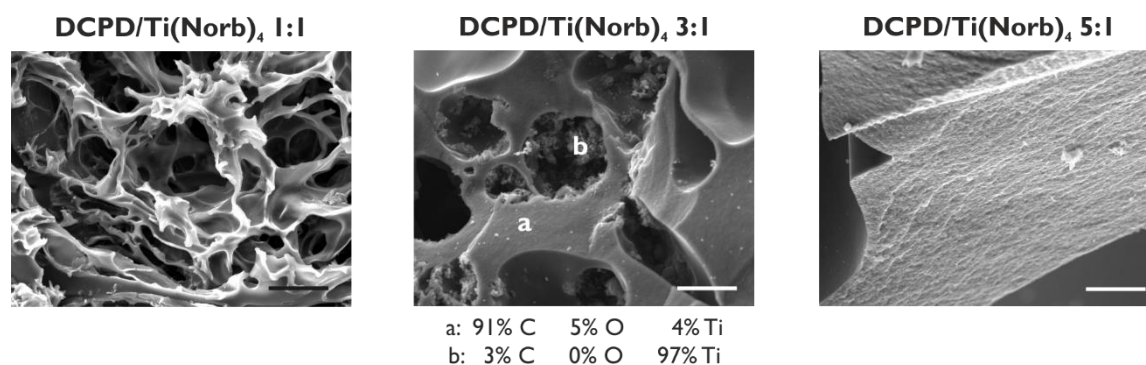


Figure 49: SEM images of the three different copolymers after carbonisation at $1380\text{ }^\circ\text{C}$ for 2 hours, for the sample depicted in the middle, for two positions an EDX was taken; scale bars correspond to $10\text{ }\mu\text{m}$.

It is unclear if the roughness on the cracks surface resulted from the sample breaking or from meso- or microporosity. By increasing the $\text{Ti}(\text{Norb})_4$ amount during polymerisation, a macroporosity becomes visible *via* SEM imaging. While the sample with the same amount of DCPD and $\text{Ti}(\text{Norb})_4$ has

interconnected pores with a stable polymer network, the material with DCPD/Ti(Norb)₄ in the ratio of 3:1 combines both morphologies. Here, walls with thicknesses of a few μm have the same rough surface as visible in the right handed image. Additionally, also some macropores are visible with precipitated solid inside. Comparing the EDX results at the two different morphologies, it is clear that this sample consists of two completely different materials. The walls are mainly carbon with only small amounts of oxygen and titanium, while the small particles in the holes mainly consist of titanium with little carbon.

Additionally to the site-selective EDX analysis, an overview over larger areas was performed, with the results summarised in Table 9. For all materials, EDX analysis shows the presence of the three expected elements, carbon, oxygen and titanium. While carbon and titanium content behave as expected for the samples with the 1:1 and 1:5 ratios, the material with three times as much DCPD as Ti(Norb)₄ has a significantly higher Ti content of 45%. This is roughly the mean value of punctual measurements and could be a promising result. The XRD results, however, show that only the material with similar amounts of Ti(Norb)₄ and DCPD contains crystalline TiC and lacks TiO₂. With increasing DCPD amount, both the crystallinity and the TiC content decrease significantly.

Table 9: XRD and EDX results obtained from the three polymerised and carbonised DCPD/Ti(Norb)₄ copolymers.

DCPD/ Ti(Norb) ₄ ratio	XRD		EDX			comment
	TiO ₂	TiC	C	O	Ti	
1:1	0.5%	99.5%	83%	2%	15%	good crystallinity
3:1	6% ^{a)}	94% ^{a)}	48%	7%	45%	poor crystallinity
5:1	99.5% ^{a)}	0.5% ^{a)}	92%	6%	2%	hardly any crystallinity visible

^{a)}only approximate results due to low crystallinity.

The discussed results show the possibility to synthesise a TiC containing material using bulk polymerisation of Ti(Norb)₄ with DCPD. However, the chosen Ti(Norb)₄ to DCPD ratio seems to be important for obtaining a high Ti content combined with crystalline TiC.

3.3.4 pDCPD HIPE Modification with Titanium based Materials

A combination of the previously mentioned carbon sources and the HIPE setup was investigated to increase the carbon content in the sample before the heating step and to vary the morphology of the material.

Modification with Titanium-Isopropoxide

While Ti(i-Pr)₄ cannot be used for the preparation of Ti-containing polymers *via* ROMP, it is suitable for impregnating previously prepared pDCPD HIPEs. For the modification with Ti(i-Pr)₄, the liquid was impregnated into the pDCPD HIPEs in an ultrasonic bath to replace the air in as many voids as possible. The ultrasonification was done under nitrogen atmosphere to prevent the sol-gel process of the Ti(i-Pr)₄. Subsequently, a few droplets of water were added to start the precipitation of TiO₂ in the HIPE voids. After drying and removing the excess TiO₂ on the surface, the discs looked virtually identical before and after modification (as visible in Figure 50). The SEM images of both samples, however, vary significantly. Before modification, the pDCPD backbone forming voids connected through windows is clearly visible; after modification, those holes are filled with another substance. This other substance is TiO₂, which is not only on the surface of the HIPE structure but also fills the majority of the void volume.

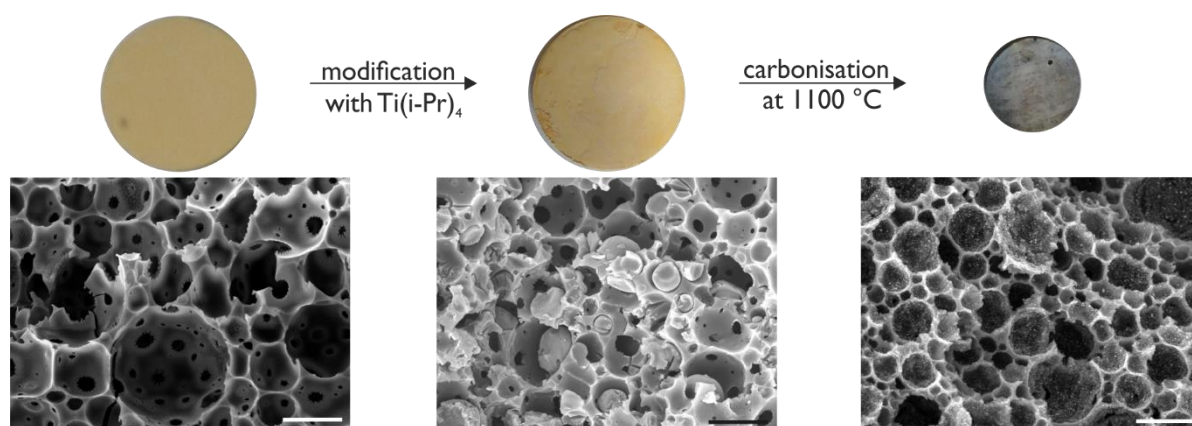


Figure 50: Modification of a pDCPD-HIPE with $\text{Ti}(\text{i-Pr})_4$ and subsequent carbonisation under argon; scale bars correspond to 10 μm .

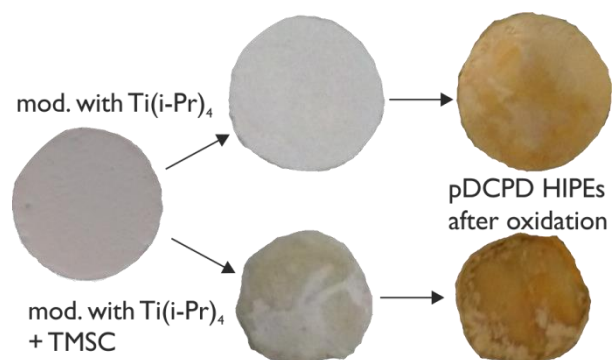
Similar to the materials already discussed in this work, the conductive properties, as well as the desired chemical composition, are obtained by a heat treatment under inert atmosphere. First, a temperature of 1100 $^\circ\text{C}$ was held for four hours. This treatment, however, resulted in shrunken, greyish/black monoliths. The corresponding SEM image shows that the big TiO_2 particles vanished, but a second layer seems to have formed on the surface. Many of the previously visible windows cannot be seen any more and the material seems to be rougher than before the heat treatment. EDX results show a high amount of Ti, but only a small amount of carbon on the modified surface. XRD further confirms these findings, as the prepared material mainly consists of TiO_2 and only 28% of the crystalline parts correspond to TiC.

One possible explanation for the high content of TiO_2 is the size of the pure TiO_2 particles prior to the heating process. Here, maybe the carbon content close enough to the particles was too low to successfully form TiC during carbonisation. This problem could be solved by impregnating the material with a carbon source in addition to the TiO_2 precursor. Therefore, trimethyl-silyl-cellulose (TMSC) was filled into the pDCPD voids too. The TMSC, toluene, $\text{Ti}(\text{i-Pr})_4$ mixture was filled into the pores using an ultrasonic bath. In contrast to the other setup, we here used diluted HCl instead of distilled water which caused TiO_2 and cellulose to precipitate. That way, both, titanium and additional carbon, were present in the HIPE, but it was important to obtain a uniform distribution in the disc. Again, the appearance of the discs did not differ visibly before and after the modification. After drying and oxidising, the material was carbonised using the same conditions as before. The resulting disc looked similarly to the one depicted in Figure 50 and also the SEM image did not differ significantly. Additionally, this material almost exclusively consists of TiO_2 with only approximately 0.5% TiC present in the sample. This unexpected result can be explained considering that TMSC is a solid and needs to be dissolved prior to the impregnation step. This leads to a much lower concentration of the $\text{Ti}(\text{i-Pr})_4$ in the impregnation mixture and in the resulting monolith and therefore also to a higher mass loss during the heating process while the loss in diameter and height of the disc were similar in both setups. Altogether, the addition of TMSC did not result in any improvements but decreased the overall Ti-content. This does not have to be a negative aspect, as a high mass loss in combination with a maintained morphology should result in materials having a high surface area.

Before discussing the change in heating temperature to higher values, the focus is on the oxidation of the pDCPD discs. As mentioned before, the oxidation of the discs lead to stability against organic solvents like toluene and elevated temperatures (under inert atmosphere). When un-oxidised samples are immersed in, for instance, toluene, the material swells drastically and loses its shape.¹⁵⁵ This could also help to fill even the smallest pores during the modification step. Therefore, un-oxidised discs were modified with only $\text{Ti}(\text{i-Pr})_4$ and both $\text{Ti}(\text{i-Pr})_4$ and TMSC. While the dimensions of the material

modified with only $\text{Ti}(\text{i-Pr})_4$ did not change a lot during the impregnation, the disc swelled significantly in the toluene based solution which was used for the modification with $\text{Ti}(\text{i-Pr})_4$ and TMSC. The disc then shrank a lot during drying and to some degree lost its disc-like shape. It did not remain flat but bent and the colour changed to a light beige (visible in Figure 51).

Figure 51: Modification of un-oxidised pDCPD HIPEs with subsequent oxidation.



As a carbonisation of un-oxidised DCPD polyHIPEs is not possible if the morphology should be maintained, the discs were oxidised subsequent to the modification but prior to the heating process. The change in colour to yellow/orange/light brown happened overnight instead of a period of four to five days, which means that the TiO_2 present seems to accelerate the oxidation. The reason for this is unclear, but the excess oxygen in the sample may result in a faster colouring of the disc. However, due to the larger deformation of the sample immersed in toluene, this procedure is only really practical for the modification with pure $\text{Ti}(\text{i-Pr})_4$.

Then it was investigated how the carbonisation at $1400\text{ }^\circ\text{C}$ affects the TiO_2 content and if pure TiC can be obtained. In Figure 52, SEM images of modified pDCPD samples are depicted, both impregnated with only $\text{Ti}(\text{i-Pr})_4$ (blue frame) and with a combination of $\text{Ti}(\text{i-Pr})_4$ and TMSC (green frame). For a good comparison, in the middle an image from a modified sample is depicted, containing cavities and connecting windows. The 4 h duration of the heating step was kept with the higher temperature. While the time period obviously was too long for the sample modified with pure $\text{Ti}(\text{i-Pr})_4$, some carbon and also TiC was retained in the resulting material modified with $\text{Ti}(\text{i-Pr})_4$ and TMSC.

The influence of the varied modification is also visible in the structure in both images. On the right hand side, smaller, but HIPE-like morphology is visible, whereas the left handed images only show a molten structure consisting of pure TiO_2 . Also EDX analysis (values for all discs given on page 90ff) did not show a carbon signal. As TiC starts to form at $1100\text{ }^\circ\text{C}$ (as already investigated), the plateau time was minimised to two hours to result in a higher content of carbon. Here, discs oxidised both prior and after modification were carbonised and analysed. While the two materials oxidised before modification maintained the HIPE-like morphology, the bulk of the ones oxidised after the modification changed significantly. Here, additionally to the visible, but significantly smaller cavities, also ‘inverse’ cavities were formed, which looked like hollowed spheres. The difference in both structures, alternating irregularly, is nicely visible in the bottom right image of Figure 52.

The amount of Ti-source added to the pDCPD HIPE disc influences the shrinkage and mass loss to some degree, as those parameters significantly increased when both $\text{Ti}(\text{i-Pr})_4$ and TMSC are added. However, the additional carbon source normally also leads to a higher carbon and TiC content in the final product (save the modification of the un-oxidised sample). Generally speaking, the most promising results were obtained by modifying the previously oxidised samples and heating them to $1400\text{ }^\circ\text{C}$ for two hours. Nonetheless, also discs heated to $1100\text{ }^\circ\text{C}$ and the later oxidised samples were compared in first electrochemical tests.

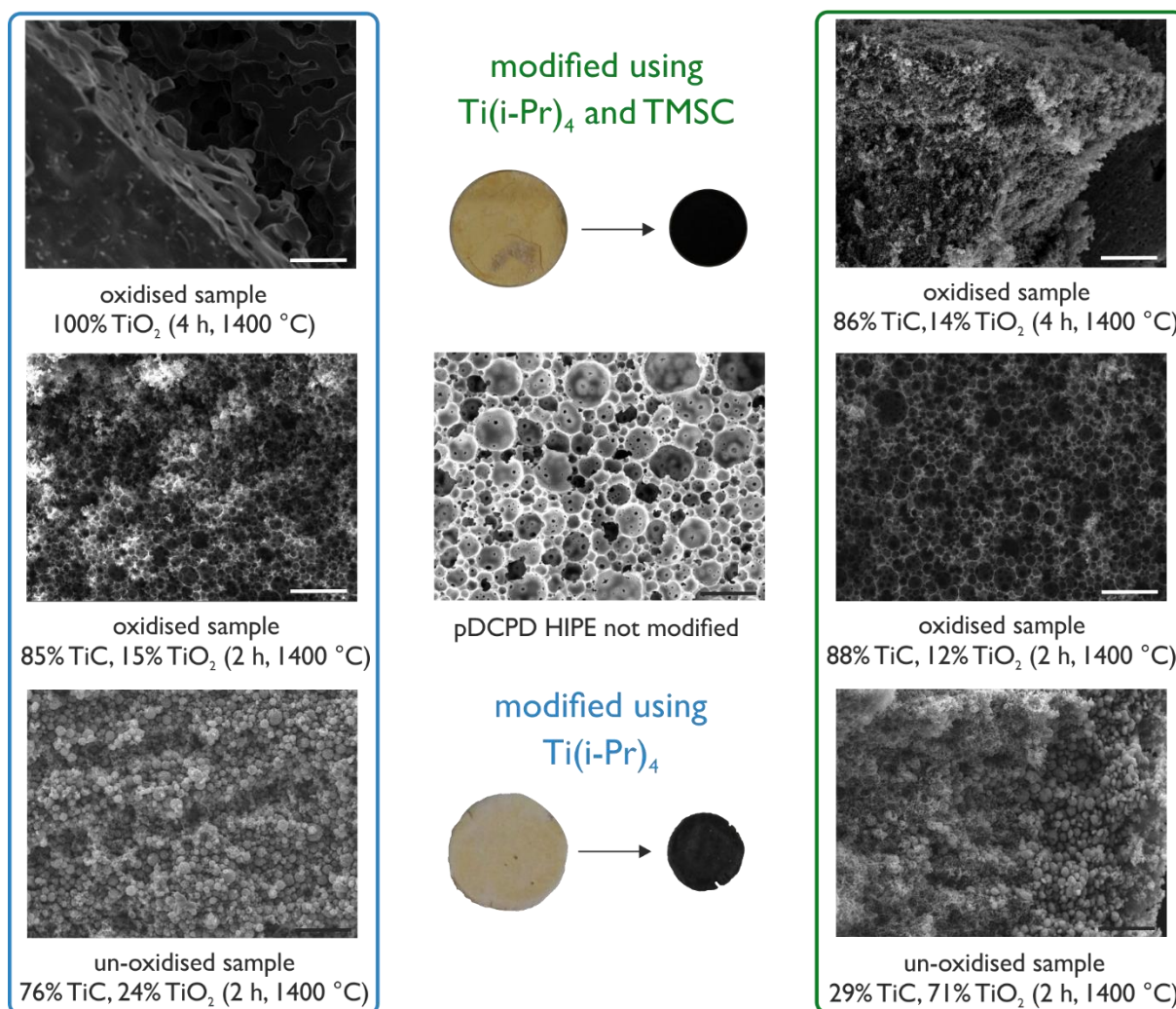


Figure 52: Carbonisation at 1400 °C for two/four h of the different modified pDPCPD HIPEs; scale bars correspond to 20 μm.

The cyclic voltammetry measurements are again compared to a KB reference material, coloured in black in Figure 52. While all curves corresponding to materials modified with $\text{Ti}(\text{i-Pr})_4$ and TMSC again are coloured in green, the other only modified with $\text{Ti}(\text{i-Pr})_4$ are depicted in blue. All green curves have their current maximum at a discharge potential of Li_2O_2 formation in the range of 2.6 V *vs.* Li/Li^+ . While the material heated to 1400 °C has a similar performance as the reference material, both other green curves, 1100 °C and the un-oxidised HIPE, reach much lower current densities, which corresponds well to the much lower TiC content of those samples, with 0.5% and 29%, respectively. The blue curves, on the other hand, show a different result. Here, the material heated to 1100 °C (dashed blue line) on the one hand has the highest current density, but on the other hand the obtained maximum is well below the discharge potential of Li_2O_2 . The oxidised pDPCPD HIPE heated to 1400 °C has its maximum current at approximately 2.6 V *vs.* Li/Li^+ , but its current density is rather small. In both cases, the discs which were modified prior to the oxidation, did reach low current densities and no current maximum in the range of Li_2O_2 formation was visible.

Taken together, modifying the pDPCPD HIPE did work with both, pure $\text{Ti}(\text{i-Pr})_4$ and a $\text{Ti}(\text{i-Pr})_4$ /TMSC/toluene mixture. Carbonisation programs at 1100 °C and 1400 °C were performed, and the materials impregnated with TMSC and $\text{Ti}(\text{i-Pr})_4$ and treated with the higher temperatures, resulted in a higher TiC to TiO_2 ratio and better CV results. Overall, some good results were obtained, but a pure TiC/carbon composite remained elusive.

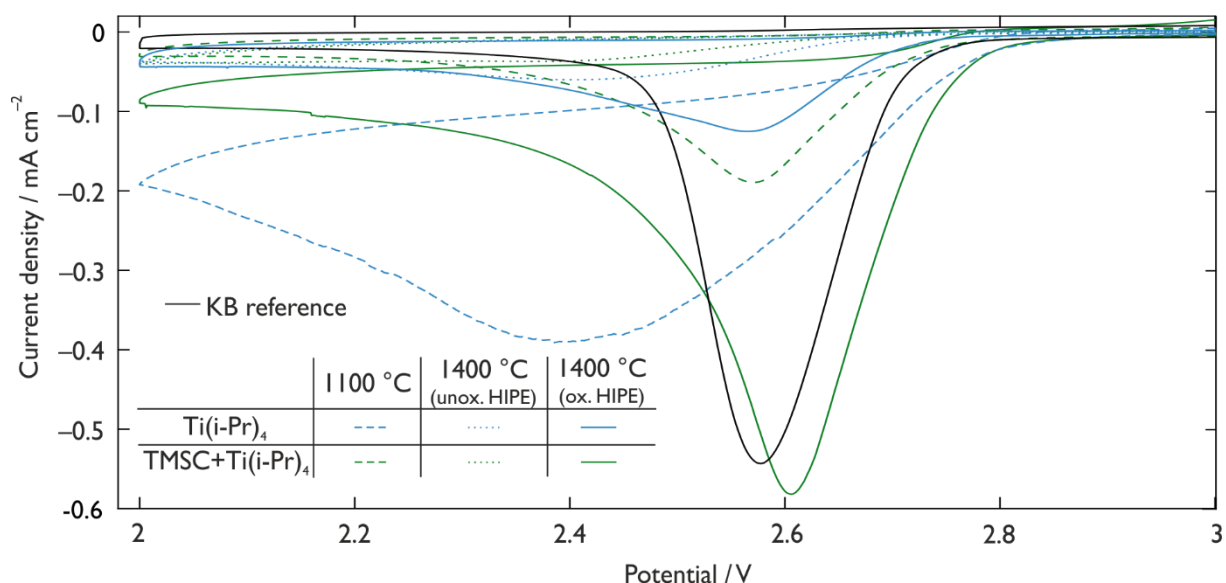


Figure 53: Cyclic voltammety results of the with Ti(i-Pr)₄ or TMSC and Ti(i-Pr)₄ modified and subsequently carbonised pDCPD HIPEs compared to a porous carbon black electrode; the CV was recorded with 50 $\mu\text{V s}^{-1}$ and as electrolyte 0.1 M LiClO₄ in TEGDME was used.

Modification with Titanium-Norbornene

Ti(Norb)₄ was used for the synthesis of homo- and copolymers as precursors for the TiC formation. But those polymers had different drawbacks ranging from a disadvantageous TiO₂-to-TiC ratio to insufficient porosity. The pDCPD HIPE discs modified with Ti(i-Pr)₄ and TMSC already resulted in materials with the 'HIPE' morphology with a significant percentage of TiC in the material. Therefore also Ti(Norb)₄ was tested as impregnation material.

In contrast to the Ti(i-Pr)₄ modification, Ti(Norb)₄ is a solid and therefore first had to be dissolved in toluene under inert conditions to prevent decomposition of the monomer with moisture. The discs were impregnated as in the previous attempts, using an ultrasonic bath. Instead of inducing a sol-gel process with water, the polymerisation of the norbornene moieties was started using M2 catalyst and curing the sample at 80 °C for two hours. The curing was carried out in a Teflon[®] mould as the Ti(Norb)₄ polymer is strongly sticking on glass surfaces. Again, after drying, no difference is visible when comparing pristine and impregnated HIPE (cf. Figure 54). Ti(Norb)₄ is easily visible *via* SEM image; it deposits as a layer on the holes. The lower Ti content and the better distribution on the surface of the pDCPD should hopefully result in the formation of pure TiC on carbon after the carbonisation.

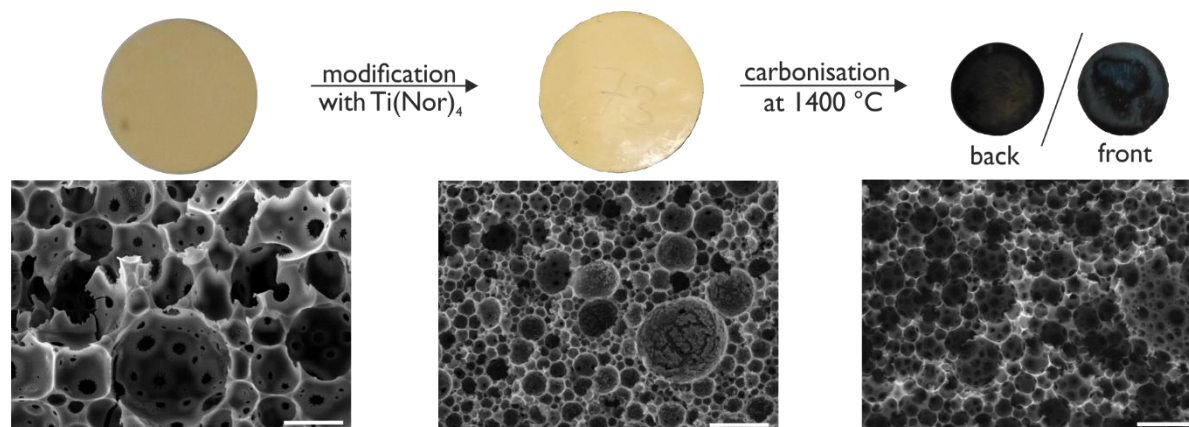


Figure 54: Modification of the pDCPD HIPE with the Ti(Norb)₄; scale bars correspond to 10 μm .

Taking the results from the already discussed attempts into account, these modified HIPEs were in most cases carbonised at 1400 °C, which resulted in black, shrunken discs in the following called Ti(Norb)₄@HIPE. The morphology was maintained throughout the heating process in all attempts, but the walls separating the holes are significantly thinner than before the carbonisation. The surface of the material, visible in Figure 55, left hand side, also consists of pores; the HIPE structure of the material is visible through holes. For many characterisation techniques, like battery testing or XRD analysis, manually ground material was used, Figure 55, right hand side. The main characteristic structure then can only be assumed, but is still visible when looking closely. Larger pieces of a few microns still can be identified as hole-walls that most probably broke at the interconnected windows, where the material is thinnest and least stable. Albeit smaller particles partly fill the cavity of bigger ones, there still is a lot of space to store discharge products.

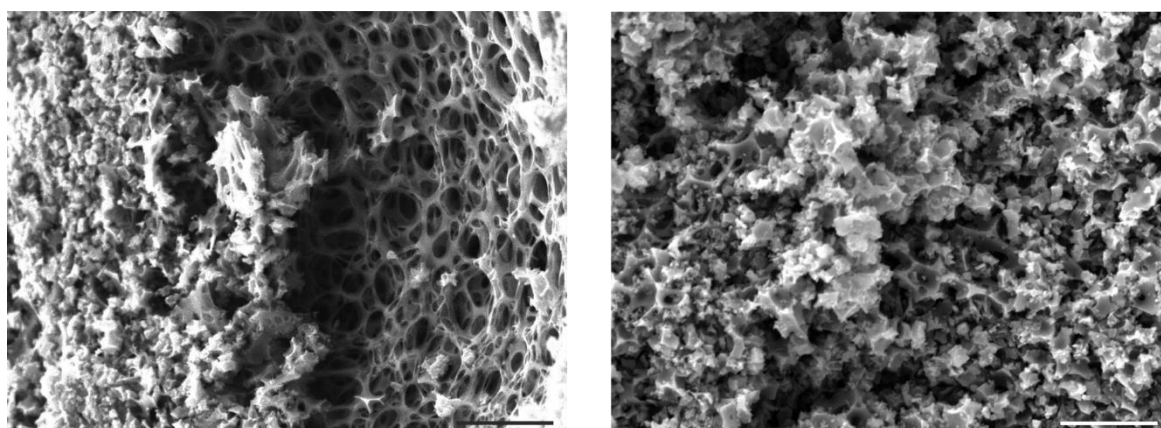


Figure 55: SEM images of a Ti(Norb)₄@HIPE sample carbonised at 1400 °C; left side: open porous surface of the material; right side: ground material used for cathode preparation. Scale bars correspond to 10 μm.

Although many experiments were performed with heating plateaus at 1400 °C, also 1100 °C, 1250 °C and 1350 °C were tested as carbonisation temperatures. The results of the different heating profiles together with EDX and XRD measurements are summarised in Table 10. Again, 1100 °C are too low for a high TiC content in the resulting material, see sample 1n. While a low amount of TiC was expected, interestingly the overall carbon content decreased from 85% to 93% to 70%. By increasing the heating temperature and sticking to a plateau time of two hours, the TiC to TiO₂ ratio shifted towards the TiC.

Table 10: Summary of differently carbonised HIPE-Ti(Norb)₄ materials, comparing carbonisation temperature/period, EDX and XRD results (numbers correspond the ones used in the experimental section for additional information).

	heating program		colour	EDX			XRD	
	temp.	time		C	O	Ti	TiC	TiO ₂
1n	1100 °C	4 h	black with greyish/blue parts	69%	14%	17%	5.5%	94.5%
5n	1250 °C	2 h	black and yellow parts; inside black	85%	11.5%	3.5%	70% ^{a)}	30% ^{a)}
16n	1350 °C	2 h	black discs	92%	2%	6%	100%	-
4n	1400 °C	2 h	black discs	93%	2%	5%	98.5%	1.5%
8n	1400 °C	2 h	black discs, sample scoop yellow	91%	5.5%	3.5%	87%	13%
13n	1400 °C	8 h	black and brown parts	43%	13%	44%	20%	80%

^{a)} low crystallinity; ratio of TiO₂ to TiC could only be estimated.

Above 1300 °C it was possible to obtain pure TiC-carbon composites with a high carbon content and only 2 a% of oxygen (16n and 4n). This synthesis was repeated a few times with similar results for the elemental and the TiC-to-TiO₂ ratios. In all cases, the Ti(Norb)₄ amount was about 30% to 50% of the mass of the polymer disc before modification. The TiO₂ content of the resulting material increases with increasing Ti(Norb)₄ content. Exemplary, the results from sample 8n are given in Table 10 and Figure 56. Here, the TiO₂ content is 13% and the disc was only modified with 13.5% Ti(Norb)₄. Small differences

were already visible directly after carbonisation as the discs were black, but the sample scoop was yellow instead of grey. The yellow colour suggests TiO₂ in the sample. In addition to a suitable Ti(Norb)₄-to-pDCPD ratio, the heating time is crucial. Sample 13n was kept for eight hours at 1400 °C, which resulted in mostly black discs with small brown parts and a low carbon content of only 43%. The diffraction pattern (see Figure 56) shows a high TiO₂ content of 80%. The crystallinity of this sample, however, is very high when comparing 13n to 1n. The TiO₂ reflex at approximately 27° is very pronounced and easily visible even if only small amounts are present.

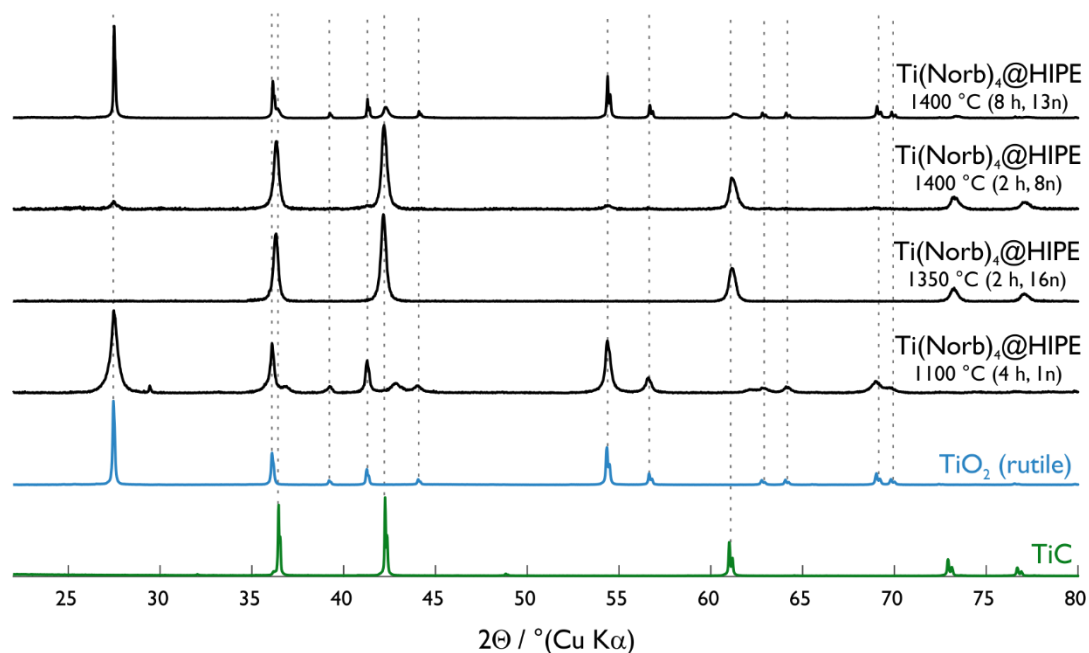


Figure 56: Powder XRD patterns of TiO₂ and TiC reference materials compared to four different pDCPD HIEPs modified with Ti(Norb)₄ and carbonised under argon but for different periods and at various temperatures.

The TiC-to-carbon ratio in the material can only be estimated using EDX analysis. One possibility to gain more information about that ratio would be an activation of the carbonised powder using a CO₂ atmosphere. This should burn away additional carbon in the sample, leaving the pure TiC material. Similarly to the activation of the unmodified HIEPs, the powder was again heated to 900 °C, kept at the elevated temperature for two hours under CO₂ and cooled to room temperature naturally under argon. We hoped to combust all residual carbon left in the material and maintain the crystalline TiC present to obtain a highly porous pure TiC material. The resulting grey powder, however, consisted of pure, highly crystalline, TiO₂. As hardly any carbon was left in the material, the Ti-content of the pristine powder could be estimated to be around 15 a%.

The promising results of the already discussed analysis methods motivated a closer investigation of the synthesised materials. The porosity of the material, one of the key requirements for a Li-O₂ cathode material, was analysed by nitrogen adsorption measurements, Figure 57. The depicted curve from sample 4n, which was heated to 1400 °C, shows porosity in all three regions. The adsorbed volume below $p/p_0 = 0.5$ gives information about the microporosity whereas the volume close to $p/p_0 = 1$ corresponds to macroporosity. The hysteresis between adsorption and desorption relates to the mesoporosity.

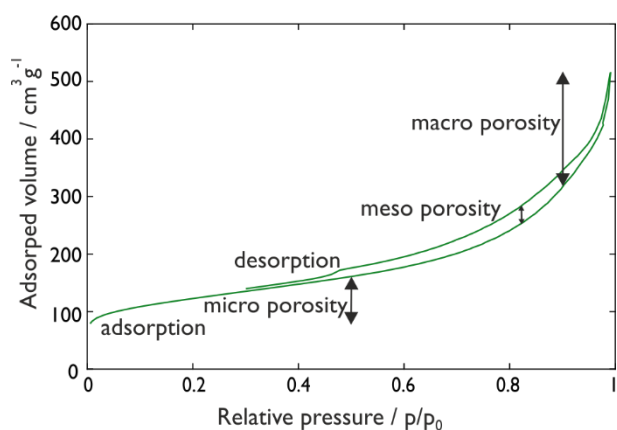


Figure 57: Nitrogen adsorption measurement of sample 4n. The graph can be analysed regarding present porosity in the micro- (below $p/p_0 = 0.5$), meso- (difference between adsorption and desorption) and macroporous (increase close to $p/p_0 = 1$) range.

Results for all measured samples are summarised in Table 11, together with the reference materials used in the electrochemical tests. The surface area can be calculated using the BET or the BJH method. The former considers all pore sizes, which normally results in a higher surface area. The latter only includes the slope increase between 0.5 and 1 (p/p_0), which corresponds to meso- and macroporosity. For all synthesised materials, the BET surface area is about double the BJH surface. This means that a high amount of micropores is present in the samples. While samples 4n and 8n, both carbonised at 1400 °C, have surface areas of approximately 400 $\text{m}^2 \text{g}^{-1}$, 16n, which was only heated to 1350 °C, has a surface area of 280 $\text{m}^2 \text{g}^{-1}$. All three results are more than ten times the surface area of the TiC nanoparticles. Ketjen black, the black carbon reference, has a more than three times higher surface area than the synthesised materials and hardly any micro porosity, whereas SuperP (SP) is more or less in the range of the TiC nanoparticles.

Table 11: Results obtained by nitrogen adsorption measurements and by measuring the bulk density. Surface area calculated by BET gives the entire porosity, calculation by BJH only takes pores larger than 2 nm into account. Bulk density was measured using the density of graphite ($\rho = 2.26 \text{ g cm}^{-3}$) as value for not porous carbon.

	surface area		pore diameter	bulk density	porosity
	BET	BJH			
16n	285 $\text{m}^2 \text{g}^{-1}$	153 $\text{m}^2 \text{g}^{-1}$	3.83 nm	0.238 g cm^{-3}	89%
4n	432 $\text{m}^2 \text{g}^{-1}$	225 $\text{m}^2 \text{g}^{-1}$	3.84 nm	-	-
8n	404 $\text{m}^2 \text{g}^{-1}$	206 $\text{m}^2 \text{g}^{-1}$	3.85 nm	-	-
TiC	19 $\text{m}^2 \text{g}^{-1}$	13 $\text{m}^2 \text{g}^{-1}$	2.75 nm	-	-
KB	1397 $\text{m}^2 \text{g}^{-1}$	1219 $\text{m}^2 \text{g}^{-1}$	3.86 nm	0.138 g cm^{-3}	94%
SP	54.5 $\text{m}^2 \text{g}^{-1}$	42 $\text{m}^2 \text{g}^{-1}$	2.73 nm	0.098 g cm^{-3}	96%

Additionally to the surface area, with BJH the average pore diameter (in the mesoporous range of 2 to 50 nm) can be determined. An average curve for that determination is depicted in Figure 58. The average pore diameter of all three synthesised materials is at approximately 3.8 nm and similar to the one of KB, whereas TiC and SuperP have significantly smaller pores.

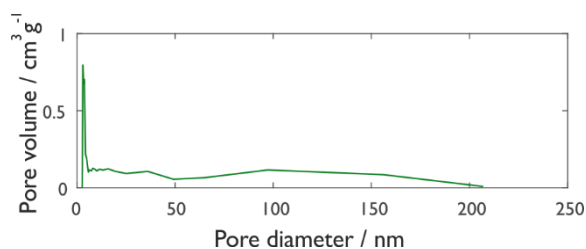


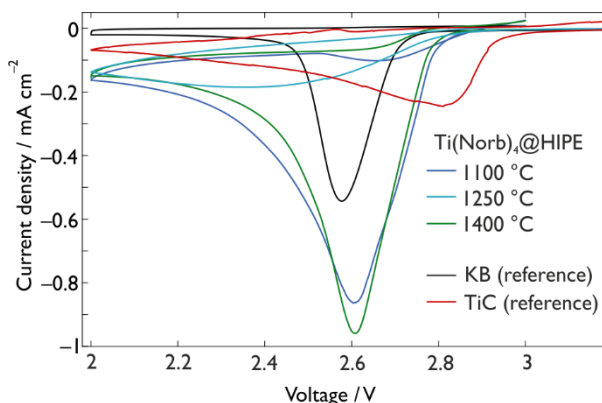
Figure 58: Exemplary pore volume graph of a $\text{Ti}(\text{Norb})_4@HIPE$ material measured using nitrogen adsorption measurement.

Bulk density and porosity of the $\text{Ti}(\text{Norb})_4@HIPE$ material are with 0.238 g cm^{-3} and 89% in the same range as the activated pDCPD polyHIPE samples. Here, the calculation of porosity is only an approximation, as the density of graphite is used as the not porous value in the formula. At least part of the material however consists of TiC, which has a density of 4.93 g cm^{-3} . Using this density would

give a porosity of 95%. The true porosity will lie somewhere in between and therefore be close to the one measured for both carbon reference materials but slightly lower.

Compared to the TiC nanoparticles, porous TiC shows a promisingly high surface area for the battery application of the material. Electrochemical and chemical stability as other key requirements, as well as the overall cell performance are discussed in the following. A first overview of the electrochemical performance can be obtained by cyclic voltammetry measurements, Figure 59. Here, the obtained current as well as the position of the peak current can be investigated.

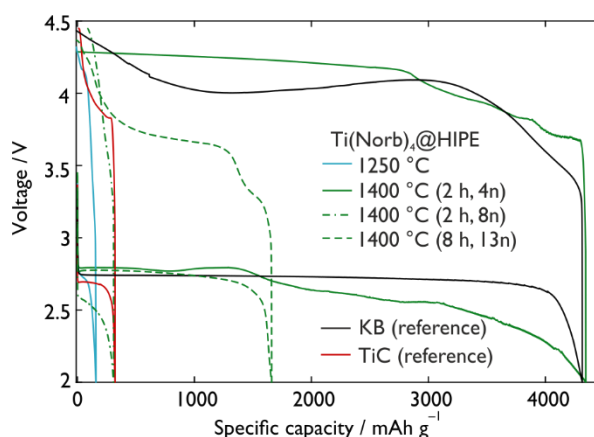
Figure 59: Cyclic voltammetry measurement of three $\text{Ti}(\text{Norb})_4@ \text{HIPE}$ materials compared to a porous carbon and TiC nanoparticles as reference compounds; measurement was done in 1.0 M LiNO_3 in DMAc and the CV was recorded with $50 \mu\text{V s}^{-1}$.



Comparing the synthesised materials, the samples heated to 1400 °C (dark green) and to 1100 °C (dark blue) result in high current densities of approximately 0.9 mA cm^{-2} . The cell with the carbon reference material (black curve) results in a similarly shaped curve with a significantly smaller current density. The sample heated to 1250 °C (light blue curve) does not have any visible peak current and is only in the current density range of the TiC (red curve) reference, a material known for small capacities.⁴⁰ In this figure, the amount of active material present during cycling is not taken into account, which favours the $\text{Ti}(\text{Norb})_4@ \text{HIPE}$ materials, especially the one heated to 1100 °C, as they contain approximately 6 and 2 mg, instead of 1 mg which was used for the KB electrodes.

This difference in active material weight is influencing the specific capacity attained *via* galvanostatic cycling, depicted in Figure 60. Again, TiC and KB are shown as reference materials, with capacities of 250 mAh g^{-1} and 4300 mAh g^{-1} , respectively. For the $\text{Ti}(\text{Norb})_4@ \text{HIPE}$ materials depicted in this figure, a correlation exists between crystallinity, the amount of TiC and specific capacity.

Figure 60: Galvanostatic cycling of four $\text{Ti}(\text{Norb})_4@ \text{HIPE}$ materials compared to a porous carbon and TiC nanoparticles as reference compounds; measurement was done in 1.0 M LiNO_3 in DMAc applying a current of 70 mA g^{-1} .



The $\text{Ti}(\text{Norb})_4@ \text{HIPE}$, carbonised at 1250 °C (light blue curve), with hardly any crystallinity and a high amount of TiO_2 , has a very low capacity and no plateau forms during discharge. The materials carbonised at 1400 °C show various capacities ranging from 250 to 4300 mAh g^{-1} . By increasing the amount of TiC relatively to TiO_2 , we gain higher specific capacities. While the sample heated to 1400 °C for eight hours (80% TiO_2) has a capacity in the range of the TiC reference, the specific capacity of sample

4n is similar to the one of the carbon black reference. Li_2O_2 is also visible in the SEM images of Figure 61. On the left hand side, an overview of a discharged and washed cathode is given. The main part of the surface is filled with Li_2O_2 and only small parts of the steel grid (current collector) and the HIPE structure are still visible. Zooming into the part of the visible HIPE structure, Li_2O_2 toroids of approximately 500 nm in diameter are visible on the surface of the HIPEs voids.

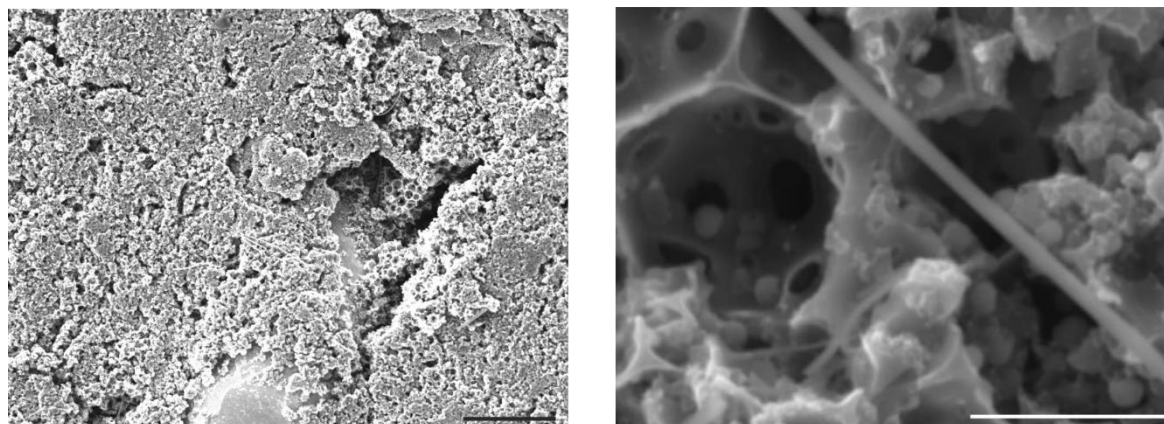


Figure 61: SEM images of a cathode after discharge in 1.0 M LiNO_3 in DMAc; left side: overview of the washed electrode (scale bar corresponds to 50 μm); right side: zoomed into a HIPE structure with Li_2O_2 toroid growth on the surface, fibres are leftovers of the separator (scale bar corresponds to 5 μm).

The requirement of a high storage capability of the discharge product – which directly correlates to the discharge capacity – is therefore fulfilled for the $\text{Ti}(\text{Nor})_4@$ HIPE materials heated to at least 1350 $^\circ\text{C}$ for two hours (4n and, not depicted, 16n). The material is further characterised for electrochemical and chemical stability by analysing the amount of oxygen consumed/evolved during cycling and the amounts of formed Li_2CO_3 (following the method described in Chapter 3 and Schafzahl *et al.*⁶³). The pressure change correlates with the oxygen consumption/evolution during cycling. This is correlated to the flow of e^- defined by the current. In Figure 62a, the molar flux of oxygen and electrons are shown. Theoretically, two electrons are needed for the reduction of one oxygen molecule resulting in a ratio of two to one. Practically, this ratio differs, and is related to the amount of Li_2O_2 and side products formed during cycling. Another visualisation is shown in Figure 62b, with the change in oxygen pressure related to the expected value based on capacity.

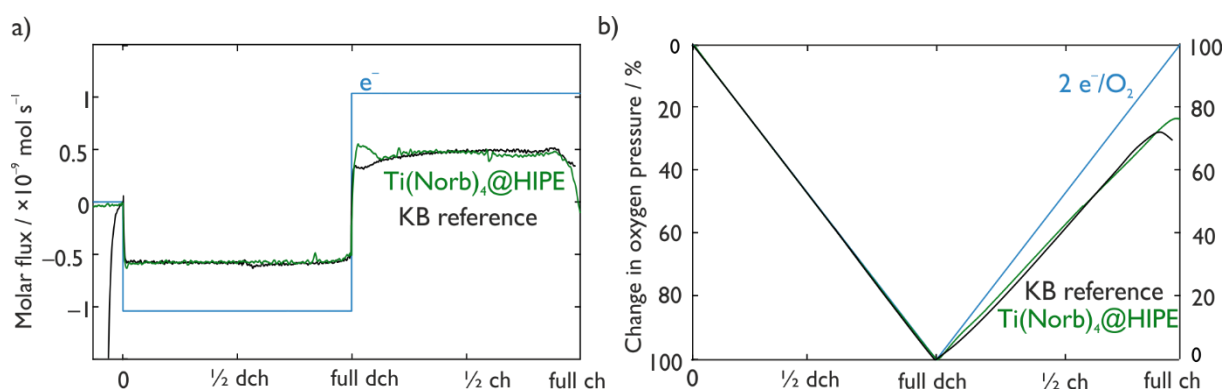
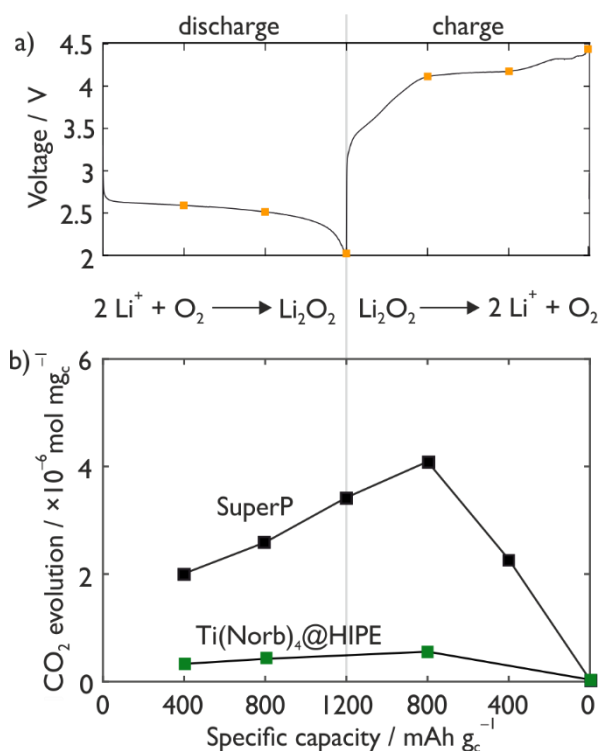


Figure 62: Change in oxygen pressure during battery cycling; tests were performed with 1.0 M LiNO_3 in DMAc applying a current of 100 μA ; a) molar flux of the gaseous oxygen, calculated through the pressure change; b) deviation of the oxygen consumption/evolution from the theoretical value of two during discharge and charge; given in percent.

The amount of oxygen consumed/evolved closely matches the theoretical value during discharge, but significantly differs on charge. The carbon black reference shows steadily oxygen release at a rate that results overall in approximately 70% oxygen evolution at full recharge. $\text{Ti}(\text{Nor})_4@$ HIPE (16n) has a

significantly higher oxygen release at the beginning of charge, but soon decreases to the same evolution rate as the carbon reference material. After charge, the amount of released oxygen is slightly below 80%. This result hints at a better stability during cycling, which is further supported by evaluating the carbonaceous side products formed during the first cycle, Figure 63. The reduction of inorganic side products is evident for the newly synthesised TiC/carbon composite material. Comparing the amount of CO₂ evolution of the Ti(Norb)₄@HIPE material (carbonised at 1400 °C for 2 hours, 4n) with a SuperP carbon reference, the values are significantly lower during all stages of discharge and charge.

Figure 63: Analysis of Li-O₂ cathodes (SuperP and Ti(Norb)₄@HIPE) cycled containing 0.1 M LiClO₄ in TEGDME; a) typical voltage profile of the Ti(Norb)₄@HIPE cell applying a cell current of 70 mA g⁻¹; b) amount of carbonaceous side products formed during cycling.



Altogether, the combination of Ti(Norb)₄ as titanium precursor and pDCPD as carbon source resulted in a TiC/carbon composite with the typical 'HIPE' structure, fulfilling all key requirements necessary for the application as cathode material for the Li-O₂ cell.

3.4 Summary

A cathode material suitable for the application in Li-O₂ batteries needs to fulfil several key requirements: The material needs to be electrically conductive, highly porous to store the discharge products and electrochemically and chemically stable in the cell environment. Traditionally used carbon materials normally fulfil the first two, but lack stability. Thus the possibility to form highly porous TiC materials was investigated, which were shown to offer the desired stability, based on various routes.

Starting with pure carbon materials, the HIPE approach as well as the use of a porogenic solvent were tested to obtain highly porous materials. Best porosity and surface areas were obtained by additionally activating pDCPD HIPEs at elevated temperatures using CO₂. With surface areas of approximately 1000 m² g⁻¹ and capacities of 10 000 mAh g⁻¹, a true alternative to KB and SuperP as cathode materials was found. However, the problem of (electro)chemical stability during cycling remained. Simultaneously, TiO₂, TiN and electrospun fibres containing TiO₂ were investigated as precursors for TiC or TiO_{2-x} containing materials. These attempts failed to provide the desired properties and were thus abandoned.

The knowledge obtained through all these experiments was used to investigate two organometallic compounds, Ti-isopropoxide (Ti(i-Pr)₄) and Ti-norbornene (Ti(Norb)₄). The latter was first investigated, but the carbon content in the precursor polymer was too low to obtain a high TiC content in the final material. Finally, a combination of the pDCPD HIPE setup with the organometallic titanium sources was tested. Ti(i-Pr)₄, Ti(i-Pr)₄ + TMSC and Ti(Norb)₄ were all filled into the large pores of pDCPD HIPE discs, which were then carbonised at temperatures above 1000 °C. From those three attempts, Ti(Norb)₄ showed by far the best morphologies, TiC contents and electrochemical characteristics. Impregnating pDCPD HIPEs with 30% to 50% Ti(Norb)₄ and carbonisation above 1300 °C for two hours under argon led to a TiC/carbon composite material. The surface area was increased tenfold with respect to TiC nanoparticles and the material had sufficient porosity to store Li₂O₂ for large specific capacities. The electrochemical performance is comparable to classical porous carbon materials – the second key requirement is therefore fulfilled. Last but not least, the increased (electro)chemical stability could be shown by pressure measurements and greatly reduced side products during cycling.

4 Singlet Oxygen as Major Cause for Parasitic Chemistry in Metal-O₂ Batteries

As already discussed in the introduction, parasitic chemistry has to be minimised to reduce high overpotentials on charge, increase cycle life and efficiency of Li-O₂ and Na-O₂ batteries. Up to date, the strong nucleophile and base, O₂⁻, as intermediate during cycling, was most widely mentioned as the main cause for side products.^{7,45,53,156} Also Li₂O₂ can be the reason for the decomposition of electrolyte and/or cathode material.^{7,45,47,62} But also at charging potentials below 3.5 V vs. Li/Li⁺ and therefore within the stability range of the carbon cathode, and without Li₂O₂ present, side products were formed.^{44,45,47} This leads to the assumption that something else present in the battery must significantly contribute to parasitic chemistry.

4.1 Theoretical Background

Ground state molecular oxygen, consisting of two oxygen atoms with six electrons each, consists mainly of doubly occupied molecular orbitals. Only the π^* orbital contains solely two unpaired electrons which results in the paramagnetic character (term symbol $^3\Sigma_g^-$) of this molecule, Figure 64 left. Consequently oxygen is a stable di-radical in its ground state. Both low excited states have singlet spin ($^1\Delta_g$ and $^1\Sigma_g^+$, see Figure 64 centre and right), and only differ from ground state oxygen regarding the spin and occupancy of the two electrons in the π^* orbital. The energetical closeness of the ground and both excited states (94 kJ mol⁻¹ and 157 kJ mol⁻¹, respectively^{157,158}) was already predicted in 1928 by Mullikan.¹⁵⁹

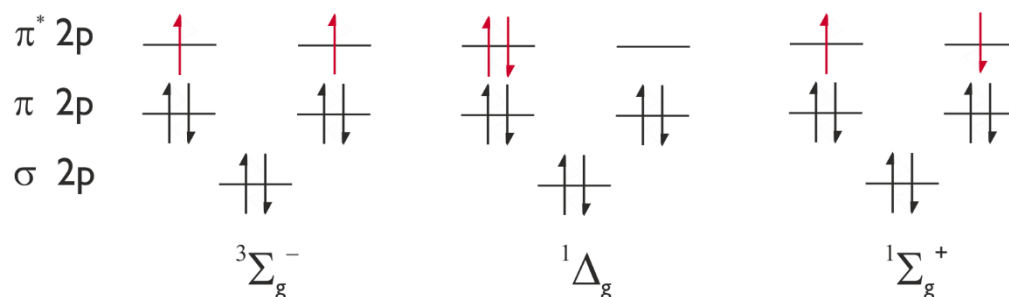


Figure 64: The molecular orbitals of oxygen in the ground ($^3\Sigma_g^-$) and first two excited states ($^1\Delta_g$ and $^1\Sigma_g^+$).

4.1.1 Properties and Synthesis of Singlet Oxygen

The electron configuration endows singlet oxygen with typically much higher reactivity towards organic substrates in comparison to ground state dioxygen; its chemical reactions with other molecules compete kinetically with possible physical deactivation processes.¹⁵⁸ Generally, the fate of $^1\text{O}_2$ is to decay into the ground state or to react with the environment. There is both spontaneous decay from the dimeric aggregate ($[^1\text{O}_3]_2$, dimol) and the single molecule ($^1\text{O}_3$, monomol) with emissions at 668 nm/703 nm and 1270 nm, respectively.¹⁵⁷ Quenching of $^1\text{O}_2$ by the environment may either be a physical process leading to $^3\text{O}_2$ or a chemical process leading to covalently bound oxygen atoms. The rate constants are in literature expressed as k_p and k_c , respectively.¹⁶⁰

Frequently, $^1\text{O}_2$ reacts with molecules of the solution or the environment and due to their varying reactivity, the lifetime of singlet oxygen in solution ranges from one to several hundred microseconds.^{157,161,162,60} In contrast, in a 'collision-free' environment, the lifetime of $^1\text{O}_2$ is theoretically in

the range of 10^4 seconds.^{161,160} The long theoretical lifetime results from the fact that the transition from singlet to triplet oxygen is forbidden based on symmetry, spin and parity reasons and is maybe the most forbidden molecular electronic transition in nature.^{160,161} If it still takes place, different radiation emissions are possible but only the one at about 1270 nm is usually used to measure the ${}^1\Delta_g \rightarrow {}^3\Sigma_g^-$ transition.^{157,158,162,163} The exact wavelength differs depending on the solvent, but in all cases the radiation is very weak. In contrast to that, the transition from ${}^1\Sigma_g^+ \rightarrow {}^1\Delta_g$ is spin allowed and the lifetime of ${}^1\Sigma_g^+$ is smaller by several orders of magnitude.^{157,160} It is therefore assumed that all singlet oxygen is normally ${}^1\Delta_g$, so this excited state will be called singlet oxygen or ${}^1\text{O}_2$.

An often used method to generate singlet oxygen is the photo-oxygenation with a sensitizer (cf. Figure 65) that is excited by radiation in a specific wavelength region and partially undergoes intersystem crossing.

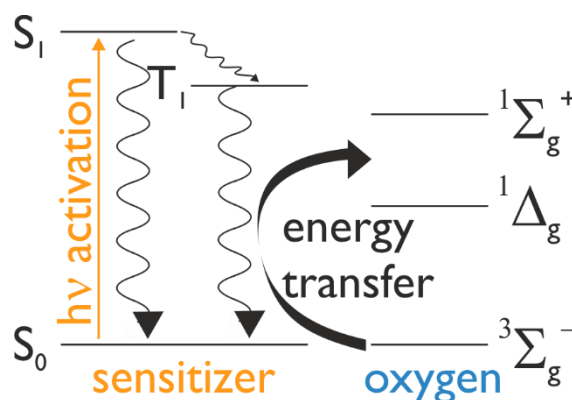
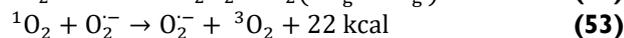
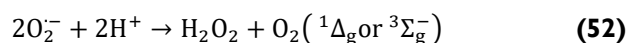


Figure 65: Generation of ${}^1\text{O}_2$ via photo oxygenation using a sensitizer; depicted energy levels should only be considered as relative and not absolute values/gaps.

Subsequently the energy is transferred to oxygen and ${}^1\text{O}_2$ is formed.¹⁵⁸ Another method to generate singlet oxygen is by the reaction of metal or hydrogen peroxide with chlorine or strong acids like hydrochloric acid. Sodium and lithium peroxide, in particular, seem to have a high reactivity for the ${}^1\text{O}_2$ production.¹⁶⁴ Adam *et al.* even stated, that these peroxide reactions are the main chemical source for singlet oxygen.¹⁵⁷ ${}^1\text{O}_2$ can also be generated from superoxide when for instance protons are present. However, superoxide can also react with ${}^1\text{O}_2$ back to the triplet ground state (Equations (52) and (53)).^{165,166}



4.1.2 Quenching and Trapping of Singlet Oxygen

There are many competing pathways to deactivate ${}^1\text{O}_2$ like radiative decay and reaction with solvents or other compounds in the solution.¹⁵⁸ Due to the high reactivity of ${}^1\text{O}_2$, it is often desirable to deactivate it in a controlled way with a quencher or a trap. The deactivation first leads to a transition state, as depicted in Figure 66, where both molecules are close enough to each other to interact. If a trap is used, the oxygen is covalently bound to the other molecule and forms for example an endoperoxide. When a physical quencher is used, the quencher undergoes an intersystem crossing with the oxygen still slightly connected to it. The oxygen is subsequently released as triplet oxygen and the quencher is regenerated.

By using a quencher, the oxygen is deactivated by a physical process and both O_2 and quencher are still present after the process.¹⁶⁷ A variety of options, like aliphatic amines and quinones, are discussed in literature as sufficient quenchers.¹⁶⁸ One of the possibilities is 1,4-diazabicyclo [2.2.2] octane (DABCO),

which has high quenching rates (k_q in the range of 10^6 to $10^8 \text{ M}^{-1} \text{ s}^{-1}$ in various solvents) and works especially well in protic solvents.¹⁶² Additionally, it is stable against superoxide and in a potential range from about 2 to 3.6 V vs. Li/Li⁺ (see Figure 79 on page 81).

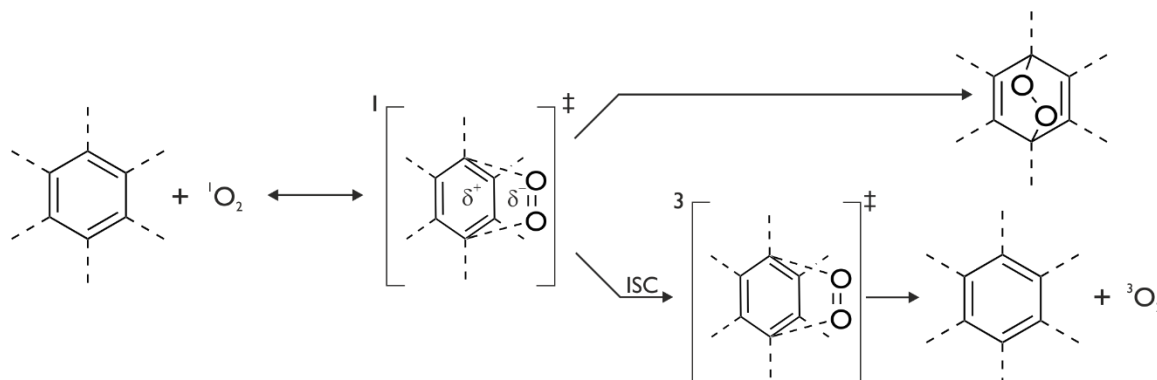


Figure 66: Deactivation of singlet oxygen with a trap (upper reaction) or a quencher (lower reaction).¹⁶⁹

In contrast to quenchers, traps react chemically with singlet oxygen. With different aromatic compounds $^1\text{O}_2$ readily reacts by a [4+2] cycloaddition to the electron-rich carbon. By adding electron donating groups to the substrate, the reactivity can be increased.¹⁶⁹ Also the size and energy of the π -delocalised system (= amount of aromatic rings), steric effects and bonding strain influence the reactivity of the trap.¹⁷⁰ Additionally, the used solvent can influence the rate constant in the range of two orders of magnitude.¹⁶⁹ In the process of endoperoxide formation, however, both, trap and oxygen, are consumed to form a new molecule. Often, these molecules are bond to a fluorescent backbone and can thus be used to quantify the amount of $^1\text{O}_2$ present in the system.^{158,60} By measuring the intensity and the wavelength of the fluorescence signals, information about the ratio between trap and endoperoxide can be obtained. For the use in LOB it is additionally important that the aromatic compound is stable in the electrochemical window between 2 and 4 V vs. Li/Li⁺. Taking all those considerations into account, we used anthracene based compounds with different substituents on the 9th and 10th position, namely 9,10-dimethyl and 9,10-diphenylanthracene as traps.

4.2 Singlet Oxygen in Li-O₂ and Na-O₂ Batteries

One way to obtain singlet oxygen is by mixing metal peroxides and superoxides, the discharge products of metal-oxygen batteries with strong acids.¹⁶⁴ Although that has been known for many years, ¹O₂ has been discussed as an intermediate in LiO₂ batteries, but considered not likely.⁴⁷ It was only mentioned as a side product in a polymer electrolyte solid state cell, where the oxidation of H₂O₂ lead to ¹O₂, which was then deactivated rapidly in the battery.¹⁵⁶ In this publication, the authors also proposed that this oxidation only leads to ¹O₂ above 4 V *vs.* Li/Li⁺, but triplet oxygen is produced when H₂O₂ is decomposed slowly at approximately 3.1 V *vs.* Li/Li⁺.

In Li-O₂ batteries, ¹O₂ was first detected in 2016.⁶⁰ Wandt *et al.* charged Li₂O₂ in the presence of a spin trap and found ¹O₂ between 3.5 V and 3.75 V, which they explained on thermodynamic grounds to stem directly from two electron oxidation of Li₂O₂. 2,2,6,6-Tetramethyl-4-piperidone (4-Oxo-TEMP) was used as a ¹O₂ trap, yielding in a stable radical. The presence and quantity of the radical was analysed using *in-operando* electron paramagnetic resonance (EPR) spectroscopy. The results were used to explain accelerated carbon degradation above 3.5 V.¹⁷¹ Equally occurring electrolyte and carbon decomposition from the start of charge at ~3 V could, however, not be explained.^{17,62,171} The used trap was not able to pick up formed ¹O₂ at lower charge voltages and failed above 3.75 V, where it was decomposed *via* self-oxidation. It further could not be used to probe the discharge reaction, because it is instable in contact with superoxide. Removing ¹O₂ was concluded to be needed but possible solutions like quenchers or traps were not discussed.

When setting out to investigate ¹O₂ in non-aqueous battery chemistry, the requirements on the method need to be fully compatible with the cell environment during discharge and charge. The main criteria were:

- stability of chemical ¹O₂ probes with other reactive O₂ species such as MO₂ and M₂O₂
- electrochemical stability in the relevant voltage windows between ~2 V and 4 V *vs.* Li/Li⁺ / ~2 V and 3.6 V *vs.* Na/Na⁺

The direct detection of ¹O₂ with the characteristic emission at 1270 nm would fulfill the wanted criteria, but is insensitive due to extremely low quantum yields. To sensitively detect ¹O₂, methods rely on chemical probes which selectively react with ¹O₂. These materials include spin traps, which become EPR active or fluorophores, which change their fluorescing behaviour due to reaction with ¹O₂ (on-off systems).^{60,158} However, these probes are not electrochemically inert in the relevant potential range and may react with O-containing intermediates.

4.2.1 Summary of the Published Work

Recently, we have investigated the ¹O₂ formation in Li-O₂ and Na-O₂ batteries in detail.^{17,172} This work involved several complementary techniques including near infrared (NIR) detection, probing ¹O₂ *via* a chemical trap by means of high performance liquid chromatography (HPLC) and fluorescence as well as probing the impact of ¹O₂ quenchers and traps on reversibility and side products *via* mass spectrometry (MS) and UV methods. Naturally, a large team was involved, which only in collaboration could obtain the comprehensive picture of ¹O₂ generation both during discharge and charge in non-aqueous metal-O₂ batteries. I mainly contributed the online electrochemical mass spectrometry (OEMS) and determined the reversibility and side products *via* a combined MS/UV-Vis method, which was newly developed for this purpose (separately published in Schafzahl *et al.*⁶³ and discussed in Chapter 2). In the following, a summary of the publications on Li-O₂ and Na-O₂ batteries is given, before the work

obtained in the course of this work concerning the Li-O₂ battery is discussed in more detail combined with some unpublished results. For completeness, it contains also results obtained by colleagues but mainly focuses on own work.

In both publications, we could show that 9,10-dimethylantracene (DMA) fulfills all requirements for a ¹O₂ probe; it is stable in contact with peroxide/superoxide, reacts rapidly with ¹O₂ to its endoperoxide (DMA-O₂) and has a sufficiently wide potential window (see Figure 79 on page 81). The detection can be performed by either monitoring the DMA consumption *via* its absorbance or fluorescence between 300 nm and 500 nm or by indirect detection of DMA and DMA-O₂ *via* HPLC.

Lithium-oxygen Battery

Complementary methods were combined to identify ¹O₂ formation during discharge and charge of the Li-O₂ battery. Using DMA, we found that ¹O₂ accounts for the majority of parasitic reaction products. The amount of ¹O₂ increases during cycling when higher potentials are reached and is further enhanced by the presence of trace water. *Operando* fluorescence detection of the DMA trap in the Li-O₂ containing trace water cell shows small amounts of ¹O₂ during discharge and significantly ¹O₂ formation on charge (starting from ~3 V *vs.* Li/Li⁺), Figure 67a. ¹O₂ formation on discharge is also significant, as shown by the ratio of DMA to DMA-O₂ measured by HPLC, depicted in Figure 67b.

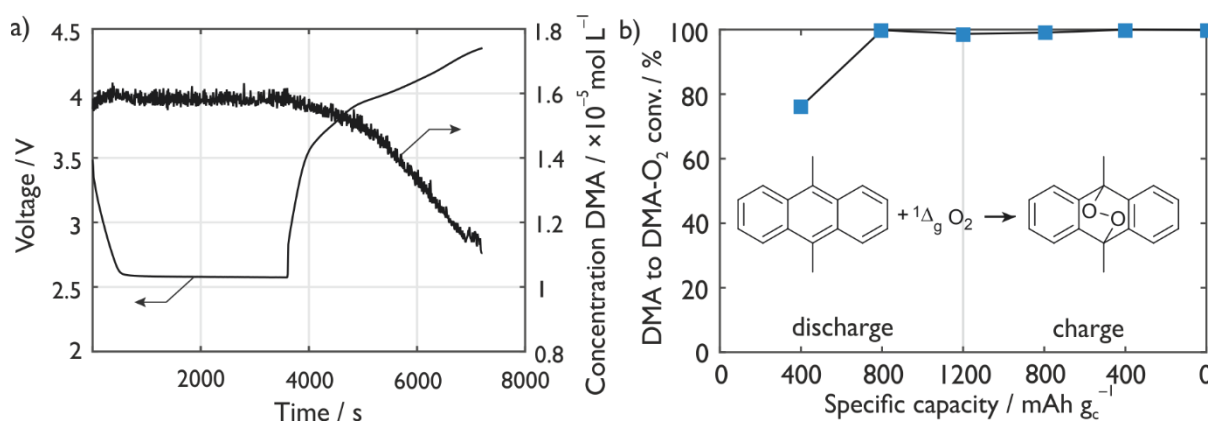


Figure 67: ¹O₂ formation and suppression during cycling of the Li-O₂ cathode; a) operando fluorescence spectroscopy during galvanostatic discharge and charge of a carbon black electrode in O₂ saturated 0.1 M LiClO₄ in TEGDME containing 1.6 × 10⁻⁵ M DMA as singlet oxygen trap; b) fraction of the initial DMA to DMA-O₂ ratio in the cells containing DMA as additive.

Additionally to the trap, also DABCO as quencher was tested. Both additives effectively reduce side reactions during discharge and charge. Due to the significant amount of ¹O₂ forming during cycling, future work should focus on the development of a sufficient quencher fulfilling all requirements.

Sodium-oxygen Battery

In Na-O₂ cells, the discharge product NaO₂, as strong nucleophile and base, was often accounted for poor cycle life and side product formation. With this publication, however, we found ¹O₂ as one main source for side products, as it forms during discharge, rest and all stages of charge. Trace water, needed for high capacities, again proves to be the main driver for ¹O₂ formation. Operando fluorescence of a previously discharged cathode was performed to proof ¹O₂ formation during all stages of charge, see Figure 68a. While the DMA signal decreases slowly below 3.3 V *vs.* Na/Na⁺, the decrease accelerates at higher charge potentials. Different to the publication about ¹O₂ formation in Li-O₂ cells, here also the storage of NaO₂ was investigated more closely, Figure 68b. The degradation of NaO₂ to Na₂O₂ was already known and our results show that also this process goes hand in hand with ¹O₂ formation.

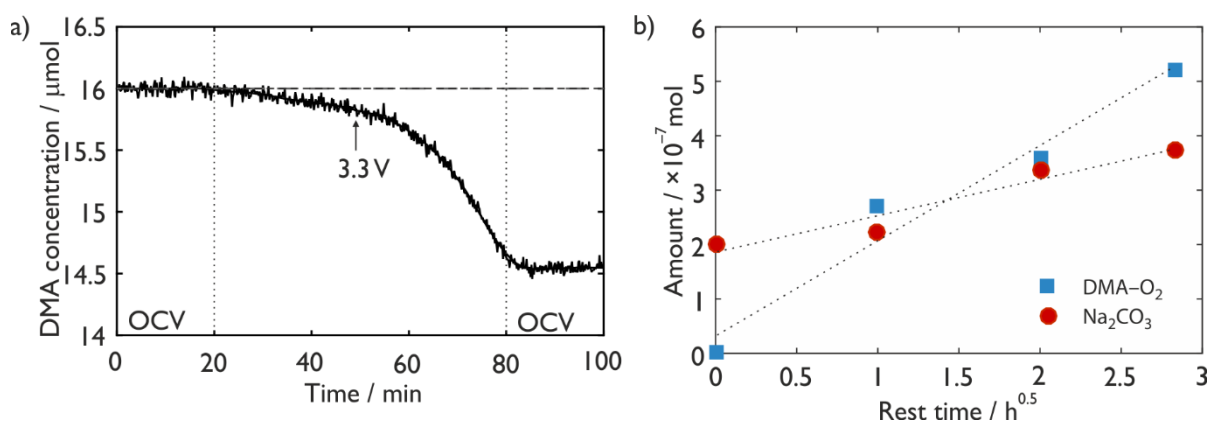


Figure 68: $^1\text{O}_2$ detection via the DMA trap in the Na- O_2 battery; a) operando fluorescence spectroscopy during galvanostatic charge of a carbon paper-cathode in 0.5 M NaOTf in diglyme containing 40 ppm H_2O and 1.6×10^{-5} M DMA (cathode was first discharged in a Swagelok[®] type cell to 75 mA cm^{-2}); b) storage experiment of discharged Na- O_2 cathodes in an electrolyte containing 30 mM DMA. DMA- O_2 content was measured via HPLC, Na_2CO_3 amount was analysed using the MS method (c.f. Chapter 2.2).

Overall, $^1\text{O}_2$ also is a big problem in Na- O_2 cells and the reason for a significant fraction of formed side products. Therefore, $^1\text{O}_2$ needs to be trapped or quenched in the cycling process before a reversible formation/decomposition of NaO_2 can be achieved.

4.2.2 Search for the Right Setup

The above results show that $^1\text{O}_2$ forms in significant quantities from the start of charging, and suggest a smaller abundance during discharge. To estimate the fraction of parasitic products originating from $^1\text{O}_2$ during discharge and charge, we examined the effect on $^1\text{O}_2$ trapping and quenching. Additionally, it was investigated whether removing the $^1\text{O}_2$ before it can react with cell components would effectively reduce these parasitic reactions. Traps remove $^1\text{O}_2$ in a chemical reaction, while quenchers deactivate it by physical quenching, for example, via a temporary charge transfer complex.¹⁶⁷ Trapping is, however, irreversible and physical quenching is therefore preferred since neither quencher nor O_2 is consumed. The literature suggests a variety of quenchers, including aliphatic amines and quinones.¹⁶⁸ We have chosen to test fluorescent anthracene based traps and DABCO as quencher. Additionally, different ether based solvents and carbon based electrodes (graphene and SuperP) were investigated. The goal was to find a stable, reproducible setup with capacities above 1000 mAh g^{-1} for further experiments concerning the $^1\text{O}_2$ formation in Li- O_2 batteries.

Figure 69 shows representative discharge/charge curves of all tested materials, electrolytes and additives. Graphene, which was chosen due to possibly high discharge capacities, was unpredictable regarding discharge capacities. Additionally to the shown curve with a capacity of about 1700 mAh g^{-1} , also capacities well below 1000 mAh g^{-1} and above 2000 mAh g^{-1} were experienced. Therefore it was decided to use SuperP, a broadly used cathode material with lower, but reproducible discharge capacities in the range of 1200 to 1400 mAh g^{-1} (red curve). Cells with 30 mM DMA in the electrolyte (blue curves) were in the same capacity range as batteries without any additive, but when diphenylanthracene (DPA, yellow curve) was used, the performance was significantly lowered to about 700 mAh g^{-1} . Additionally, DMA should have a higher reactivity towards $^1\text{O}_2$ due to the methyl substituents.¹⁶⁹

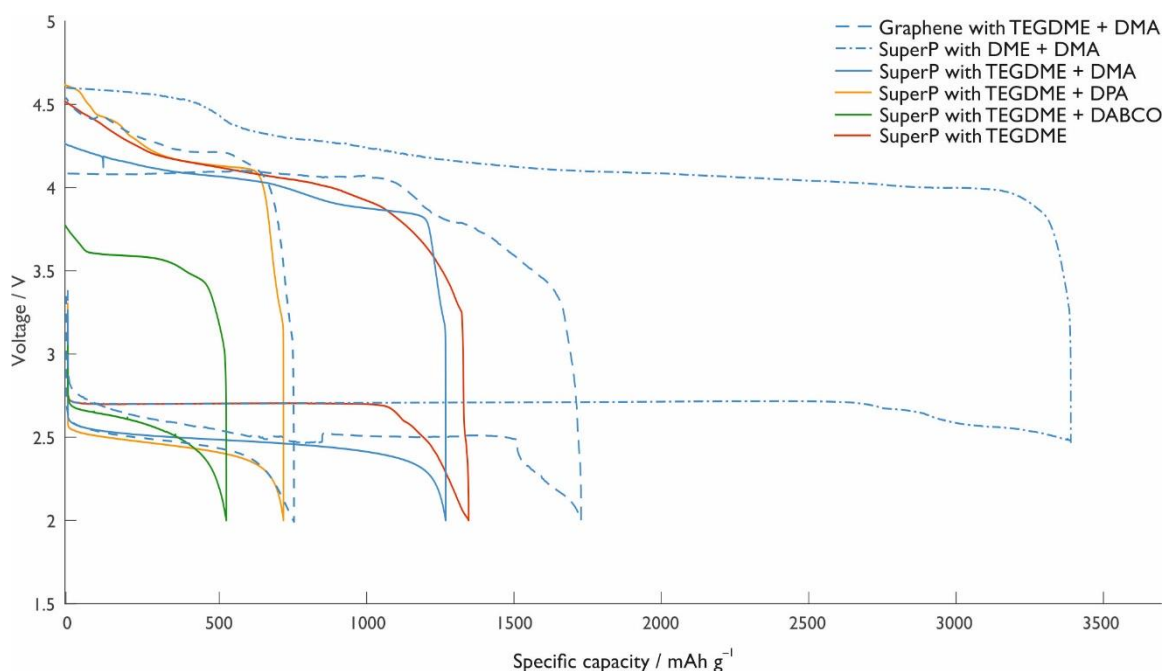


Figure 69: Galvanostatic cycling at 70 mA g^{-1} with different cathodes, electrolytes and additives; solid lines of different colors correspond to the variation of additive with SuperP as cathode material and 0.1 M LiClO_4 in TEGDME as electrolyte, cells depicted in blue were varied regarding solvent and cathode material but all contained 30 mM DMA and 0.1 M LiClO_4 .

Traps are consumed during cycling and the concentration is limited to several 10 mM by the solubility and is at the level of $^1\text{O}_2$ abundance within a cycle. Thus, we also tested DABCO as quencher. For the first tests, DABCO was used without recrystallizing it prior to use, which could be one reason for the capacity decrease to about 550 mAh g^{-1} . The same cell (green curve) shows a charge potential of $\sim 3.6 \text{ V}$, which coincides with the oxidation potential of DABCO. For further measurements recrystallized, pure, DABCO was used and the charge potential limited to $3.5 \text{ V vs. Li/Li}^+$. The tested ether electrolytes were dimethoxyethane (DME) and tetraethylene glycol dimethyl ether (TEGDME), both containing 0.1 M LiClO_4 , and yielding capacities between 3300 mAh g^{-1} and 1300 mAh g^{-1} . Although the capacity in DME seems to be significantly higher than in TEGDME, the relatively low boiling point of $84 \text{ }^\circ\text{C}$ is a major drawback. Due to the oxygen reservoir, the electrolyte can easily evaporate over time and diminish the conductivity between the electrodes.

Taking all those results into account, the effect of trap and quencher on side products was tested using a SuperP cathode, a lithium iron phosphate (LFP) anode and reference electrode, and a TEGDME electrolyte containing either no additive, 30 mM DMA or 10 mM DABCO . Both additives have been chosen, as they were reported to be effective in a non-aqueous environment and are chemically (with superoxide) and electrochemically stable (see Figure 79 on page 81).

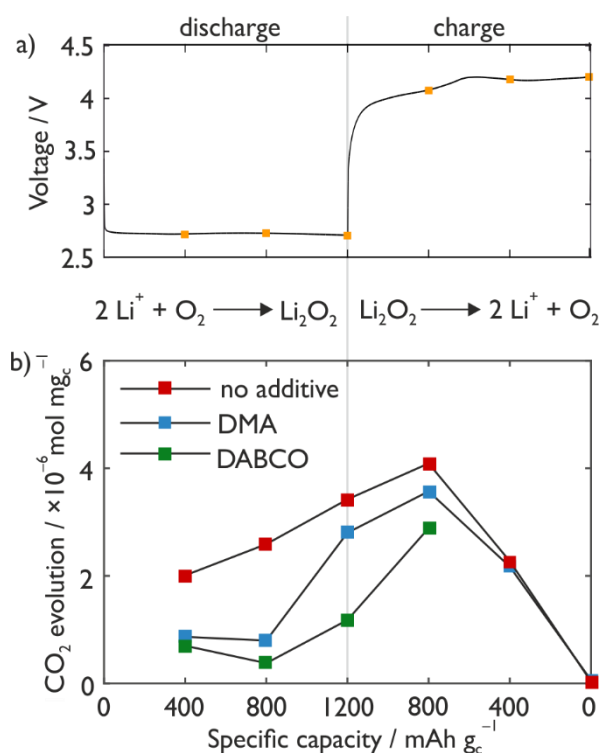
4.2.3 Cathode Analysis

The amounts of side products, $^1\text{O}_2$ and Li_2O_2 were analysed and compared to investigate correlations regarding $^1\text{O}_2$ reactivity during battery cycling. Cells were cycled to three different positions on discharge and charge (positions marked in orange in Figure 70a), then stopped and disassembled in an argon filled glove box. Cathode and electrolyte were further analysed using a technique combining mass spectrometry and UV-Vis spectroscopy (for the exact method, see Chapter 2.3) and HPLC⁽¹⁾.

⁽¹⁾High performance liquid chromatography measurements were performed by Nika Mahne.

Inorganic carbonates are measured analysing the CO₂ evolution subsequent to addition and are depicted per g electrode weight in Figure 70b.

Figure 70: Analysis of Li-O₂ cathodes cycled containing 0.1 M LiClO₄ in TEGDME without additive, with 30 mM DMA or 10 mM DABCO; a) typical voltage profile during galvanostatic cycling at 70 mA g⁻¹; b) amount of carbonaceous side products formed during cycling.



A significant reduction of side products during discharge is evident for both additives. Considering the cell with DMA first, the amount of side products is between half and one third of those without additive up to the second sampling point. The subsequent alignment to the level without DMA can be explained by consideration of the conversion of DMA to DMA-O₂, measured using HPLC and depicted in the paper summary, Figure 67b on page 68. At 400 mAh g⁻¹, 76% of the initially present DMA was consumed and none could be detected at 800 mAh g⁻¹. Thereafter, no effect on the side product formation can be expected, as is seen in the carbonate data. By considering the charge passed at the first sampling point and the DMA conversion, a ratio of ~1 mol DMA consumed per 10 mol of reduced O₂ can be determined. In the cells containing DABCO, consistently less side product formation occurred than when DMA was added and only one tenth to one third of the amount of the additive free cell was measured. At 800 mAh g⁻¹, the absolute values of inorganic carbonates are at approximately 27% (DABCO) and 37% (DMA) compared to the cells without additive. Regarding these values, at least 70% of the side products formed on discharge originate from ¹O₂. The ¹O₂ formation on charge is assumed to be much higher (when regarding the fluorescence measurements shown in Figure 67a on page 68) but with DABCO the cell could only be charged to 3.5 V due to the electrochemical stability of the quencher (*c.f.* Figure 79 on page 81). For all compositions, the amount of measureable inorganic side products decreases again on charging above 4 V, due to the decomposition of the previously formed Li₂CO₃ to CO₂.

The amount of side products formed can be expected to inversely correlate with the Li₂O₂ yield since reactive O₂ species divert electrons from Li₂O₂ into side products. Since all DMA has been consumed before 800 mAh g⁻¹ (Figure 67b on page 68), cells were only discharged to 200 mA g⁻¹ to ensure a significant concentration of additive. In a threefold determination, cathodes, discharged with different electrolytes (w/o additive, with DMA/DABCO), were analysed using the aqueous Ti^{IV}oxysulfate complex and the UV-Vis spectrometry (*c.f.* Chapter 2.1.2). After cycling, the cells were disassembled in an argon filled glovebox. For half of the cells, the electrodes and separators were mixed with the Ti-

solution right away to capture both solid peroxide and dissolved H₂O₂. The remaining electrodes were first washed with MeCN, dried under vacuum and thereafter analysed, yielding only solid Li₂O₂. Thus, it was possible to distinguish between solid Li₂O₂ (washed samples) and the total peroxide content and the exact values and peroxide/Li₂O₂ yields are given in Table 12.

Table 12: Measured Li₂O₂ and total peroxide of cells discharged to 200 mAh g_c⁻¹ using an electrolyte containing no additive, DMA or DABCO.

	TEGDME		TEGDME + DMA		TEGDME + DABCO	
	measured value	yield	measured value	yield	measured value	yield
wet samples	3.54×10 ⁻⁵ mol	86.9%	3.81×10 ⁻⁵ mol	96%	3.94×10 ⁻⁵ mol	85.1%
washed samples	2.97×10 ⁻⁵ mol	70.8%	3.93×10 ⁻⁵ mol	86.7%	3.36×10 ⁻⁵ mol	81.4%

In Figure 71, the fraction of the theoretical amount of Li₂O₂ based on capacity divided by the measured amount using UV-Vis spectroscopy is shown for the three different electrolytes. The total yield of peroxide for the samples with pure TEGDME electrolyte and with the quencher are in the same range at about 85%, whereas the pure electrolyte has a significantly higher fraction of soluble peroxide. With DMA the total yield increases to 95% and the solid yield to > 85%. The difference is much smaller for the electrolyte containing DABCO and still significantly smaller for the electrolyte with DMA than for the basic electrolyte. The smaller H₂O₂ fraction with quencher or trap could be explained by decomposition reactions that are initiated by ¹O₂ resulting in H₂O₂ instead of Li₂O₂ and more closely explained in Chapter 4.2.5.

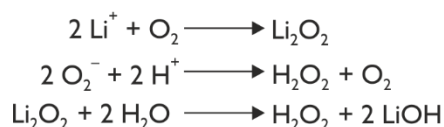
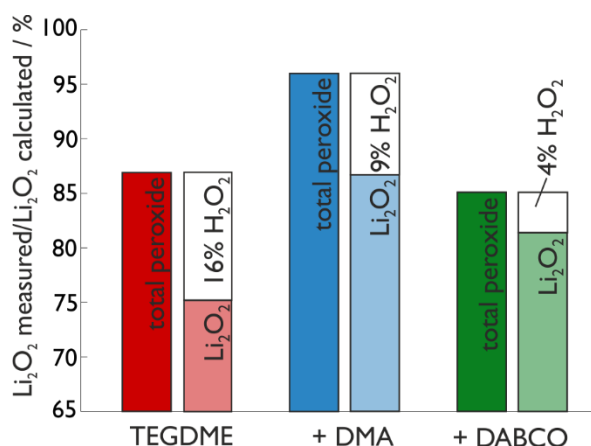


Figure 71: Percentage of Li₂O₂/H₂O₂ measured using UV-Vis spectroscopy; batteries were discharged to 200 mAh g_c⁻¹ using 0.1 M LiClO₄ in TEGDME without an additive (red), with 30 mM DMA (blue) or 10 mM DABCO (green) to form Li₂O₂ and H₂O₂. Cathodes were analysed without washing the electrodes (left columns) or subsequent to washing them with MeCN (right columns).



In summary, reactions of ¹O₂ with different cell components can result in the formation of protic products, like H₂O, which then react with Li₂O₂ and form H₂O₂. With less ¹O₂ present in the cell, a significantly higher ratio of the formed peroxide occurs as Li₂O₂.

Stability of Li₂O₂ in the cell environment

To gain information about the storage stability of Li₂O₂ after electrochemically forming in a Swagelok[®] cell, the peroxide yield of cathodes was measured, which were stored under argon for different periods of time. In all cases, the electrolyte was not removed prior to storing by washing or drying the cathodes under vacuum. In many cases, the yields were far from where to expect them. In Figure 72a, the peroxide yield in relation with the storage time is depicted. Even though there are some aberrations, there is still a trend visible. The maximum yield is decreasing over a period of a few days up to a month. Different components of the battery environment were tested to identify the reason for the decomposition of Li₂O₂ (cf. Figure 72b). In all cases, the same amount of chemically synthesised Li₂O₂ was used and the mixture was stored under argon atmosphere for six days before the peroxide content was determined. For the

mixtures containing electrolyte, the amount was significantly higher than for the regularly stored cathode discussed in Figure 72a.

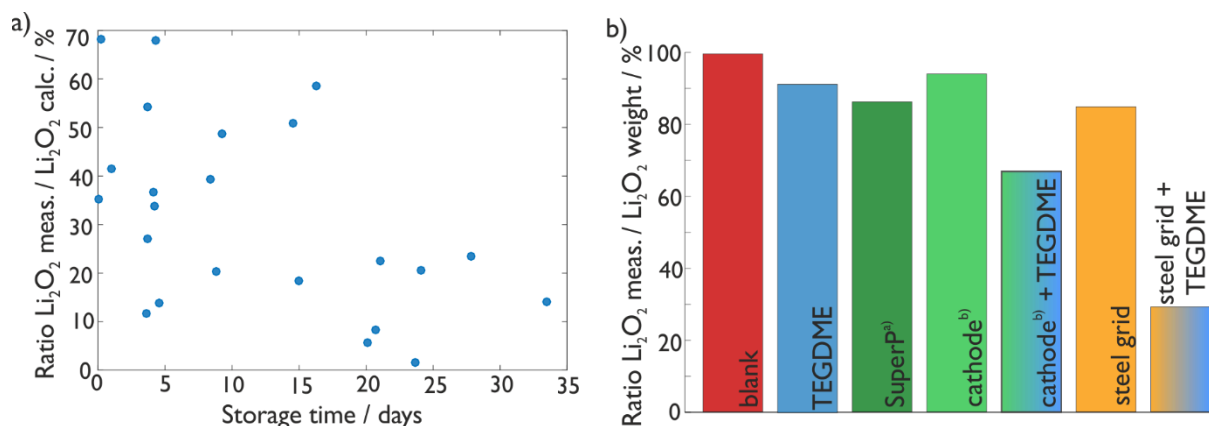


Figure 72: Decomposition of Li_2O_2 over time; a) relation between the storage time of $\text{Li}-\text{O}_2$ cathodes and the resulting Li_2O_2 yield; b) Percentage of Li_2O_2 yield for different samples after being stored for 6 days. ^{a)}the ratio of Li_2O_2 to SuperP was 3:1; ^{b)}cathodes consisting of 9:1 SuperP:PTFE binder on steel grid were used.

Compared to the blank measurement, the addition of a dry cathode or solely the electrolyte did not change the decomposition of Li_2O_2 a lot. However, SuperP and the steel grid, both main cathode components, decreased the peroxide yield from nearly 100% to below 90%. The combination of the whole electrode or only the steel grid and the TEGDME based electrolyte significantly increased the decomposition process. The higher amount of electrolyte used for this experiments in contrast to the stored electrodes used for the plot depicted in Figure 72a has led to an even more pronounced decrease of the Li_2O_2 content. Although weighting inaccuracies could influence the results, the main trend is easily visible. Both the steel and the electrolyte are the main sources for the decomposition taking place but also the carbon present plays an important role in this process. All steel types, also the stainless steel used as current collector for these experiments, contain iron atoms, which are known to decompose peroxides and are also discussed as a possible way to quantify the peroxide yield in Chapter 2.1.2. Therefore, it is important to immediately analyse cycled electrodes or to remove the solvent for storage, as it accelerates the decomposition process. Also washed and dried electrodes should be measured within 24 h to diminish errors. Additionally, alternative current collectors like aluminium, nickel or copper should be investigated regarding their influence in Li_2O_2 decomposition.

4.2.4 Online Electrochemical Mass Spectrometry (OEMS)

OEMS cells allow quantifying the consumption and evolution of oxygen during electrochemical cycling as well as the evolution of CO_2 during charging. First, cyclic voltammetry was performed to gauge the current needed to consume/evolve oxygen at a rate that is accurately quantifiable by the OEMS setup. In Figure 73, the cyclic voltammogram (CV) of the OEMS cell together with the gases measured using mass spectrometry is visible. Argon (light green, masses 20 and 40), nitrogen (dark green, masses 28 and 14), oxygen (dark blue, mass 32), water (light blue, mass 18) and carbon dioxide (masses 12, 44 and 45) are depicted with their corresponding gas flow ranging from below 10^{-12} to nearly 10^{-7} mol per minute. The purge gas mixture was 5% Ar in O_2 and the difference in the ratio of Ar to O_2 can be used to calculate the oxygen consumption/evolution during cycling. The slight increase in the Ar signal is marked with a dotted black line and takes place at a current of approximately 1 mA.

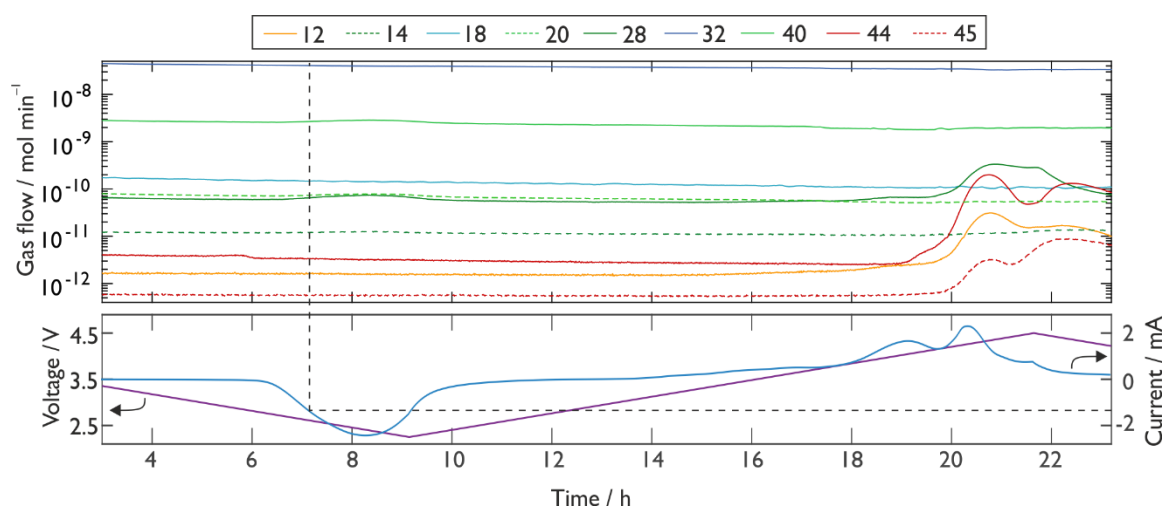


Figure 73: Online electrochemical mass spectrometry during cyclic voltammetry with TEGDME electrolyte containing 30 mM DMA. The working electrode was SuperP; the cell was cycled at $50 \mu\text{V s}^{-1}$.

For the in the following discussed galvanostatically cycled OEMS cells, the ratio of electrolyte and active material was in a similar range as for the Swagelok[®] cell and the discharge was limited to a capacity of 200 mAh g^{-1} . Both aspects were important, to guarantee a high amount of DMA still being present at the end of discharge and could act on charge. Additionally, the absolute current was at approximately 1 mA and therefore well in the detection limit of the mass spectrometer. A short open-circuit voltage (OCV) period between discharge and charge was introduced to be able to distinguish between oxygen consumption and evolution in the mass spectrometry data.

With DMA, the overpotential is significantly reduced throughout the battery cycling. The difference is significant during discharge as well as charge, comparing Figure 74a and Figure 74b. Especially interesting is also the charge potential, which is at about 4 V for the cell containing DMA and ranging from 4.2 to 4.4 V without additive. This voltage difference will be also important analysing the evolved gases, depicted in Figure 75 and discussed in the following.

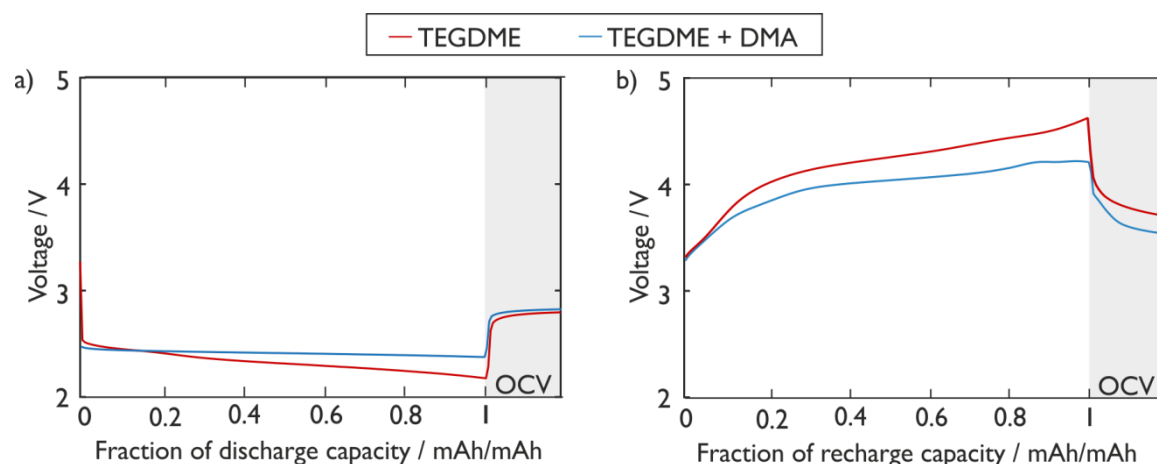


Figure 74: Discharge a) and charge b) curve of the OEMS cells; cycled with SuperP as working electrode and 0.1 M LiClO_4 in TEGDME without additive or containing 30 mM DMA with a current of 100 mA g^{-1} .

On discharge, for both cells the O_2 flow was close to the expected amount and no CO_2 evolution could be detected. When charging the cells, however, the cell containing DMA reaches an oxygen evolution of approximately 93% of the theoretical value in the beginning of charge. It fades to $\sim 2/3$ towards the end of charge. Without the trap, the O_2 evolution only reaches a maximum of $2/3$ of the theoretical value (see Figure 75b). Regarding the amount of side products, formed quantities are difficult to estimate, as

not 100% of the discharge product is Li_2O_2 ; additionally, although still present in a high concentration at the beginning of charge, DMA will be consumed rapidly. The best way to analyse side product formation using an OEMS cell is the CO_2 evolution during charge. Here, a significant difference can be observed comparing both measurements. The amount of CO_2 formed by both cells differs by a factor of 30 (calculated by integration of the CO_2 signals depicted in Figure 75b). To some degree, the lower charge potential of $\sim 4\text{--}4.1\text{ V vs. Li/Li}^+$ compared to $4.2\text{--}4.4\text{ V vs. Li/Li}^+$, visible in Figure 74b of the cell containing DMA is the reason for the high difference. But mainly the amount of side products formed during cycling has to be taken into account for comparing the CO_2 evolution of both cells.

For better understanding, the fraction of O_2 theoretically consumed/evolved compared to the real change in the oxygen flow is compared in Figure 75, c and d. For these graphs, the oxygen and electron flow depicted in Figure 75a/b were cumulated and are given in percent. During discharge, the ratio of e^- passed to O_2 was with 98% (DMA) and 95% (without additive) close 100%. In other words, $2.04 e^-$ and $2.11 e^-$ were necessary per consumed oxygen molecule, which is close to the theoretical value of two for all measurements, Figure 75c. This is, however, also the case when side products are forming *via* reactions from the already formed Li_2O_2 or intermediates and the electrolyte.⁶² Therefore, this value can only give hints about the cell performance, like the fact, that Li_2O_2 will be formed during discharge due to the two electron process.

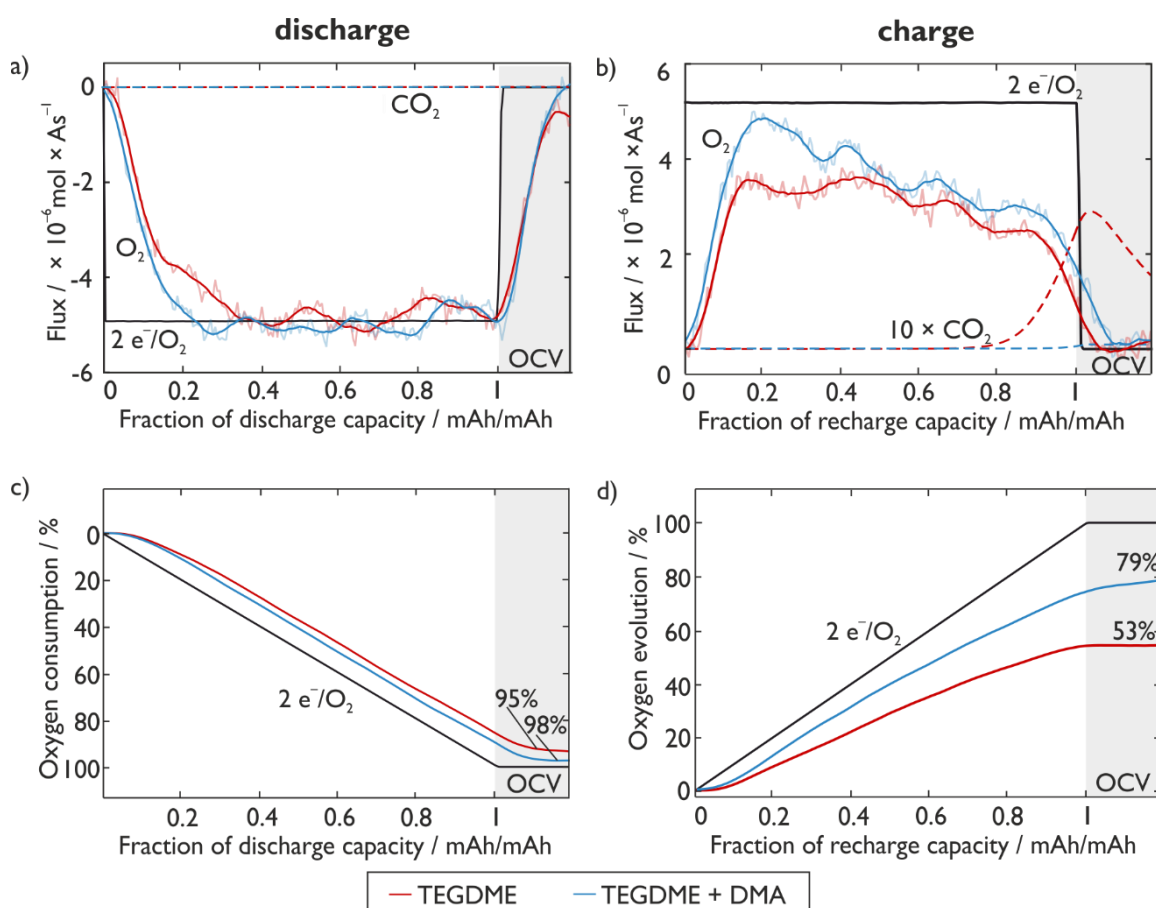


Figure 75: OEMS analysis of a Li-O_2 cell during discharge (left) and charge (right) using 0.1 M LiClO_4 in TEGDME containing no additive (red curves) or 30 mM DMA (blue curves); a)/b) oxygen and CO_2 flux compared to the amount of e^- need for discharge/charge; c)/d) change in the oxygen flux during the measurement in percent compared to the theoretical consumption/evolution following $2e^- + \text{O}_2 \leftrightarrow 2\text{O}^-$.

During charge, Figure 75d, the ratios differ more significantly from 100% and the influence of the $^1\text{O}_2$ is more pronounced. The cumulated released oxygen corresponds only to 53% of the expected value for the additive-free cell, while the battery containing DMA evolves 79% of the expected oxygen. This

corresponds to 3.76 e⁻ and 2.54 e⁻, respectively. Another difference is the slope during charging. While the blue curve (corresponding to the cell containing DMA) is roughly parallel to the black line for the first half of charge, the slope of the red curve is significantly smaller. This, in combination with the higher CO₂ evolution suggests that the majority of side products formed during charge below the oxidation limits of electrolyte and electrode can be blamed on ¹O₂.

4.2.5 Pathways to Singlet Oxygen

On both discharge and charge, a broad range of solid by-products are formed, which cannot be completely explained by the reactivity of peroxides and superoxide. In this chapter, it was shown with different methods that ¹O₂ is the main reason for side product formation in metal-O₂ batteries. But still the question arises, how ¹O₂ is formed during battery operation?

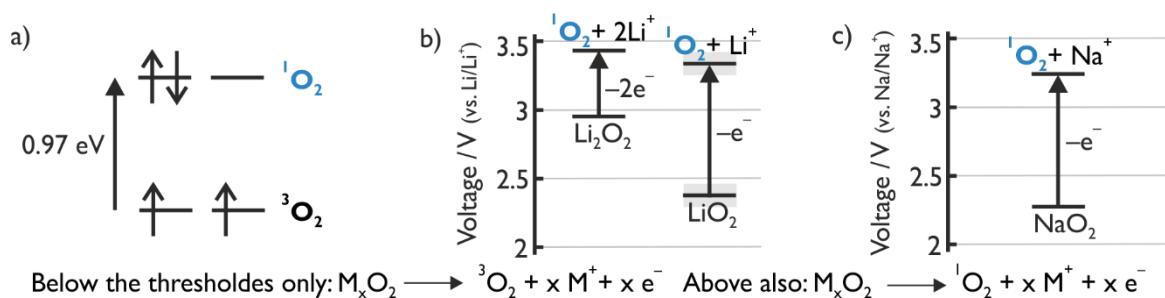
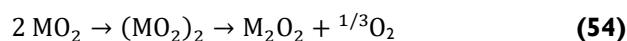


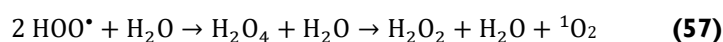
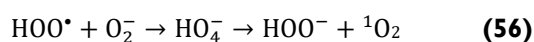
Figure 76: Energy levels of singlet and triplet oxygen and potential limits for the generation of ¹O₂ in metal-O₂ batteries; a) energy level difference between ground state triplet and excited state singlet oxygen; b) energy thresholds for superoxide and peroxide oxidation in the Li-O₂ battery; for E_{O_2/LiO_2}^0 the mean value is depicted; c) energy threshold for the superoxide oxidation in the Na-O₂ battery.

The energy difference of ¹O₂, between the first excited state, and the ground state, is 0.97 eV, as pictured in Figure 76a. This energy threshold is necessary for ¹O₂ to be directly generated from ³O₂ excitation. The potential limit is at approximately 3.24 or 3.44 V for the Na-O₂ or the Li-O₂ battery, respectively (Figure 76b/c). Above these voltages, the ¹O₂ formation has already been verified for the Li-O₂ battery⁶⁰ and our results for the Na-O₂ battery also show a significant increase of ¹O₂ above these potentials. But also during discharge and lower charge potentials the ¹O₂ formation is detectable and will be discussed in the following.

One possible source during discharge is the disproportionation of MO₂, which occurs on the pathway to Li₂O₂ formation. It is not part in the theoretical discharge process for Na-O₂ cells, but a possible reaction for NaO₂ decomposition upon storage of the discharged electrode.



For the LiO₂, using theoretical calculations, Bryantsev *et al.* found low lying isomers in both the triplet and singlet state.¹⁷³ They only analysed the reaction for the triplet state, which resulted in the evolution of ³O₂. Therefore, it can be assumed that the reaction of a singlet dimer would result in the evolution of ¹O₂. Another way to generate ¹O₂ during discharge is the reaction of proton sources with the superoxide, which is possible in Li-O₂ and Na-O₂ batteries. After HOO• is formed (Equation (55)), ¹O₂ is generated either by reduction (Equation (56)) or disproportionation (Equation (57)).



In all discussed cases, superoxide, either bound to Li or H, is the main $^1\text{O}_2$ source during discharge. During all stages of charge, the already discussed mechanisms leading to $^1\text{O}_2$ can take place. Additionally, for Li- O_2 cells, the 1 e^- oxidation of LiO_2 or the 2 e^- oxidation of Li_2O_2 can lead to the formation of $^1\text{O}_2$ also above the thresholds depicted in Figure 76, adding ways of $^1\text{O}_2$ formation. For the whole discharge/charge process, it is also important to keep in mind that superoxide is not only a source, but also a quencher of $^1\text{O}_2$ which may be a reason for the much lower amount of $^1\text{O}_2$ observed during discharge. The net-formation of $^1\text{O}_2$ depends on the relative kinetics of all superoxide sources and sinks and will change with discharge and charge, electrolyte, current and potential. Keeping charge voltages below 3.5 V / 3.3 V (for Li- O_2 and Na- O_2 batteries), however, will significantly reduce $^1\text{O}_2$ formation in metal- O_2 batteries.

4.3 Summary

Singlet oxygen is generated in the nonaqueous Li-O₂ and Na-O₂ battery throughout the whole cycling process. It is formed by Li⁺ or H⁺ induced disproportionation of superoxide or when NaO₂, LiO₂ or Li₂O₂ are oxidised at voltages beyond the thermodynamic threshold of 3.3 V, 3.26 to 3.45 V or 3.55 V *vs.* Li/Li⁺. ¹O₂ is more reactive than superoxide or peroxide and the main cause for parasitic reactions. As a result, it decomposes electrolyte and carbon electrode, resulting in lithium carbonate or organic carboxylates. Quenchers or traps can effectively reduce the side reactions. The amount of side products on discharge suggests that about 70% of the parasitic chemistry results from ¹O₂. In line with this, the yield of Li₂O₂ during discharge increases significantly when ¹O₂ is removed by a quencher or trap. The e⁻/O₂ ratio on charge as a key measure for reversibility improves from 3.8 to 2.9 e⁻/O₂ in presence of DMA as ¹O₂ trap and the amount of CO₂ evolved decreases by a factor of 30. Thus, parasitic chemistry on charge appears to nearly fully result from ¹O₂. A main factor for controlling and prevent ¹O₂ from occurring during cell cycling is a thorough understanding of the pathways leading to its formation. Although we have already discovered a broad range of reactions leading to ¹O₂ in the cell environment, especially the role of gaseous oxygen present throughout cycling has not been investigated. Here, further experiments focusing on this topic by using labeled oxygen would be necessary to gain more, important information. Altogether it can be said, that controlling the highly reactive ¹O₂, by for instance adding quenchers or optimizing charge conditions, is crucial for achieving highly reversible cell operation.

5 Methods and Preparation

5.1 General

5.1.1 Chemicals

All chemicals used were purchased from Sigma Aldrich, ABCR, Alfa Aesar, Fluka, VWR, TCI, Imerys, Messer, Merck, Roth and used as received. Only DABCO was recrystallized before usage. Solvents used as electrolytes were dried, distilled before usage and stored over molecular sieves in an inert atmosphere. The moisture content was measured using Karl Fischer titration (TitroLine KF trace). Salts were dried at 100 °C under reduced pressure and also stored in an argon filled glove box.

5.1.2 Analytical Methods

Silica-gel plates on aluminium from Merck (TLC silicagel 60 F₂₅₄) were used for thin layer chromatography. The samples were analysed using a UV-lamp or a potassium permanganate solution (1 wt% KMnO₄ dissolved in water). For column chromatography, silica gel was used as a stationary phase and different mixtures of cyclohexane and ethylacetate as the mobile phase.

Nuclear magnetic resonance (NMR) spectroscopy was performed on an Avance III 300 spectrometer with an auto sampler. ¹H spectra were measured at 300 MHz and ¹³C spectra at 75 MHz. The spectra were normally acquired in deuterated chloroform (CDCl₃) and the corresponding chemical shifts at $\delta = 7.26$ ppm (¹H) and $\delta = 77.16$ ppm (¹³C) were used to reference the spectrum.

Scanning electron microscopy (SEM) was performed on a Vega 3 SBU SEM equipped with a tungsten hair-pin cathode. Samples without significant conductivity were sputtered with gold before imaging. Information about the composition of the materials was obtained by using an INCA x-act energy dispersive X-ray (EDX) from Oxford Instruments.

BET was measured at AIT using a Quantachrome® ASiQwin™ instrument. As adsorbate nitrogen was used at a bath temperature of 77.35 K using a cell diameter of 9 mm. The obtained data was analysed by multipoint BET and BJH. The used sample weight was between 50 and 100 mg.

For TGA measurements, a Netzsch STA 449 C was used. For all measurements the sample chamber was heated with a rate of 10 °C/min in a temperature range from 20 °C to 550 °C. As purge gases He or O₂ were used with a flow rate of 50 mL/min. For one experiment, 3-5 mg of the analysed material were used.

The mass spectroscopy (MS) setup was built in-house, containing a quadrupole mass spectrometer from Balzer with a turbomolecular pump from Pfeiffer which is backed by a membrane pump. It is equipped with a leak inlet which samples from the purge gas stream. All measurements were performed with pure Ar or an Ar/O₂ mixture (5:95) as background gas. The gas flow was regulated using two digital mass flow controllers from Bronkhorst (0.014-0.7 mL/min and 0.1-5.0 mL/min) and stainless steel or PEEK tubing. For qualitative and quantitative analysis, the mass spectrometer was calibrated with different ratios of Ar, O₂, H₂ and CO₂. For the background measurement, pure argon was used, the fragmentation of the different gases was evaluated from the calibration measurement with the highest percentage of the corresponding gas. Different calibration mixtures with either oxygen or argon as base gas were done in the anticipated concentration ranges (0-10000 ppm). The resulting data was used to

identify nonlinearities and cross-sensitivities. All data was evaluated using an in-house Matlab based software.

5.1.3 Battery Setup

Cathode materials were prepared by mixing the active material first with isopropanol and then with a polytetrafluoroethylene (PTFE) binder in a ratio of 9:1. This mixture was applied on a stainless steel or aluminium mesh current collector. The electrodes were washed with H₂O/acetone 1:1 for 15 minutes and subsequently dried overnight under reduced pressure at 80 °C. Typical cathodes contained about 1 to 5 mg cm⁻¹ active material. As purchased cathode materials, KB and SuperP (C-Energy Super C65 from Imerys), were used. Glass fibre separators (Whatman, GF/F grade) were washed with ethanol and acetone and dried at 160 °C overnight prior to use. For counter electrodes, lithium iron phosphate (P198-S21 from PI-KEM, LFP) was mixed with SuperP and PTFE in a ratio of 7.8: 0.9: 1.3. The freestanding electrodes with a total mass of about 20 mg were washed with a mixture of acetone/H₂O (ratio 1:1) and dried at 80 °C overnight under reduced pressure. As reference electrodes, delithiated LFP was used instead of lithiated one and the electrodes were prepared equally to the counter electrodes. All electrodes and separators were transferred to and stored in an argon filled glove box without exposure to air.

During the course of this work, different lithium salts and organic solvents were used as electrolytes. In all cases, the electrolytes were prepared in an argon filled glovebox and were never exposed to air. For each Swagelok® cell about 140 µL electrolyte were used. For pressure cells about 250 µL and for DEMS measurements 400 µL electrolyte were needed. The mainly used electrolytes were 0.1 M lithium perchlorate (LiClO₄) in tetraethylene glycol dimethyl ether (TEGDME) and 1.0 M lithium nitrate (LiNO₃) in dimethylacetamide (DMAc). Sometimes also 0.1 M LiClO₄ in ethylene glycol dimethyl ether (DME) was used.

For electrochemical testing, three electrode cells were built using Swagelok® parts and stainless steel of the type 1.3964 from Remystahl, see Figure 77. The cells were assembled in an argon filled glove box and tested on either a SP-300 (Biologic) or BT-2000 (Arbin Instruments).

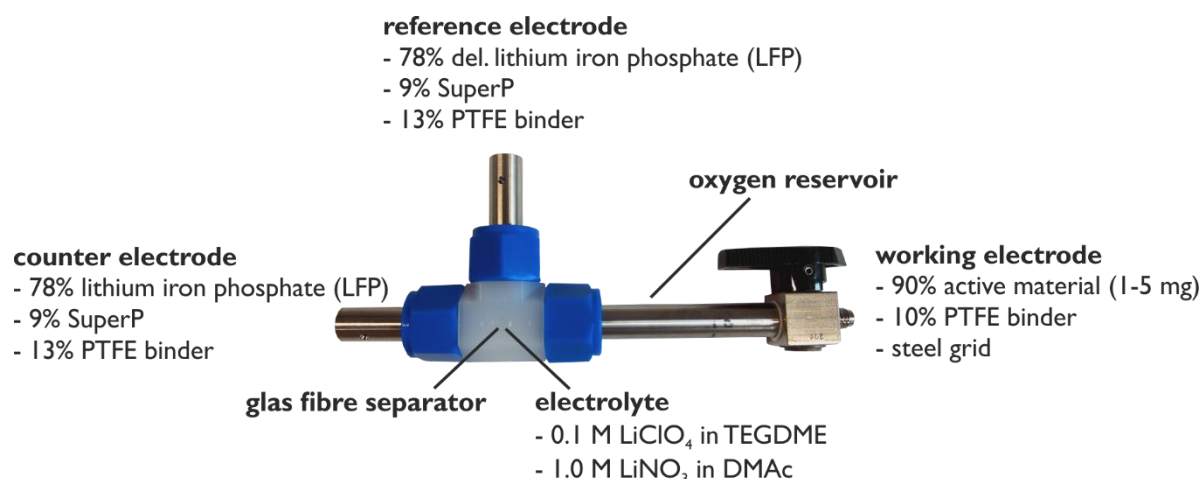


Figure 77: Setup of a Swagelok® cell with the components used in this work.

Online Electrochemical Mass Spectrometry (OEMS)

OEMS was performed in an in-house built cell based on a Swagelok® design. Both current collectors consist of polished stainless steel and double PTFE ferrules were used to ensure tightness. The gas flow

in- and outlet are integrated in the cathode current collector with two PEEK capillary tubes connected to a four-way valve. The whole cell volume is about 4.4 mL with a headspace volume of about 400 μL and a diameter of 38 mm (see Figure 78).

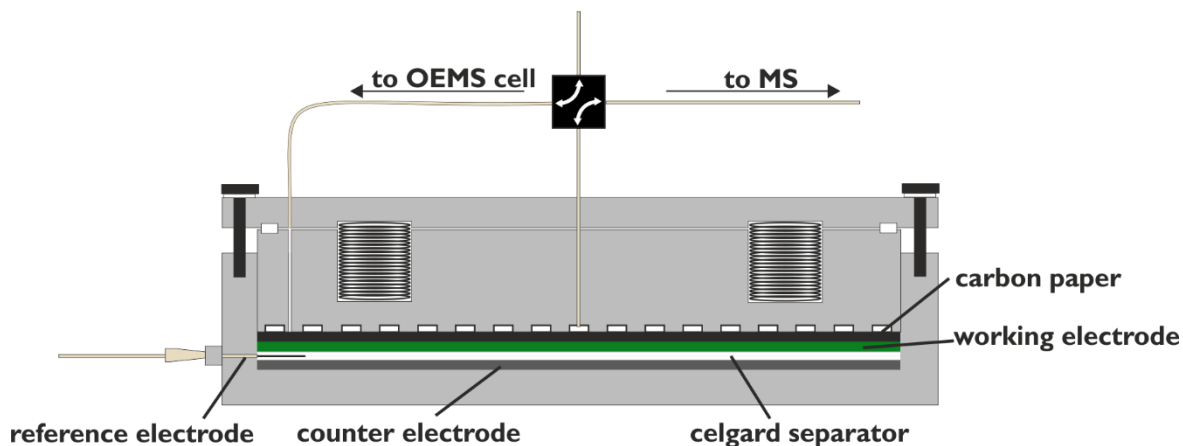


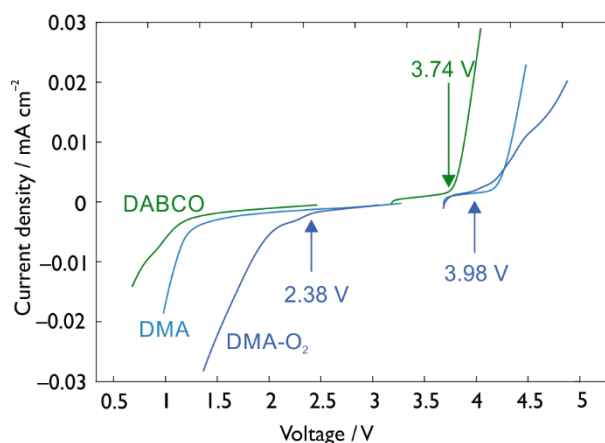
Figure 78: Schematic drawing of an OEMS setup. As counter and reference electrode LFP was used. The active material was applied on a stainless steel grid.

The cell was assembled in an argon filled glove box and purged with an oxygen/argon gas mix (ratio 95:5) with a gas flow of 70 $\mu\text{L}/\text{min}$. The consumption/evolution of O_2 during cycling is quantified with the change in the ratio of $\text{O}_2:\text{Ar}$. The flux of argon is known to be invariable and therefore the concentrations of the other gases measured can be calculated. In typical measurements, gas evolutions relative to $<0.1\%$ O_2 evolved/consumed can be detected. The amount of oxygen consumed/evolved can then be correlated to the amount of e^- used during discharge/charge. These results were visualised using a matlab scriptum.

Electrochemical Stability of DMA and DABCO

The electrochemical stability of 9,10-dimethylantracene (DMA), 9,10-dimethylantracene-endoperoxide (DMA- O_2) and 1,4-diazabicyclo[2.2.2]octane (DABCO) was investigated *via* cyclic voltammetry. All measurements were performed under argon atmosphere using 0.1 M LiClO_4 in TEGDME and 2 mM of the additive as electrolyte. A 3 mm glassy carbon disc electrode and a silver wire were used as counter and reference electrode. The measurements were calibrated using ferrocene. DMA- O_2 was generated photochemically using palladium(II) meso-tetra(4-fluorophenyl) tetrabenzoporphyrin as sensitizer. The resulting measurements are depicted in Figure 79.

Figure 79: Electrochemical stability of DMA, DMA- O_2 and DABCO. CV was performed at a sweep rate of 100 mV s^{-1} using a 3 mm glassy carbon disc electrode. As solutions 0.1 M LiClO_4 and 2 mM DMA or 2 mM DABCO in TEGDME were measured. DMA- O_2 was photochemically generated using palladium(II) meso-tetra(4-fluorophenyl) tetrabenzoporphyrin as sensitizer.



Photochemical Generation of $^1\text{O}_2$

$^1\text{O}_2$ was generated *via* photochemical generation. The sensitizer palladium(II) meso-tetra(4-fluorophenyl)tetrabenzoporphyrin was dissolved in the electrolyte and the solution bubbled with oxygen for 10 minutes. The sensitizer was irradiated for 30 minutes with a red LED light source (643 nm, 7 W) to form $^1\text{O}_2$, Figure 80.

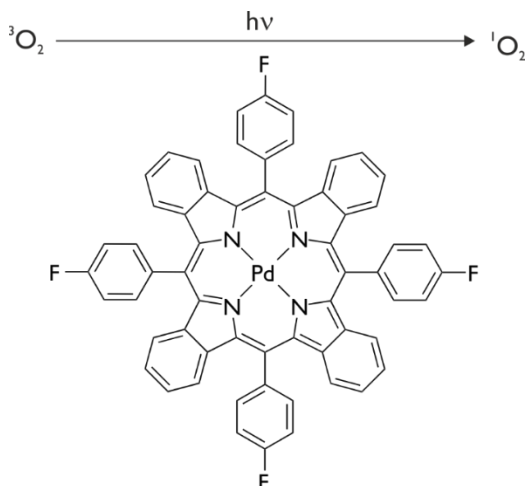


Figure 80: $^1\text{O}_2$ generation using a palladium(II) based sensitizer, which was irradiated at a wavelength of 643 nm.

5.2 Method for Electrode Analysis

5.2.1 Sample Preparation

For the characterisation of electrodes with the mass spectrometer, batteries were disassembled after cycling in an argon filled glove box without exposure to air. If not noted otherwise, all electrodes were washed and dried before measuring them. For that purpose, dimethyl carbonate (DMC, metal-ion batteries) or DME (metal air batteries), were used, respectively. The washing/drying step was done approximately one to two hours after the cells were finished and the measurement took place within one to two days. For the development of the analysis method, often chemically synthesised reagents were used. Air sensitive materials like peroxides and superoxides, were stored and prepared insight the glove box, different carbonates were weight and poured into the setup on air.

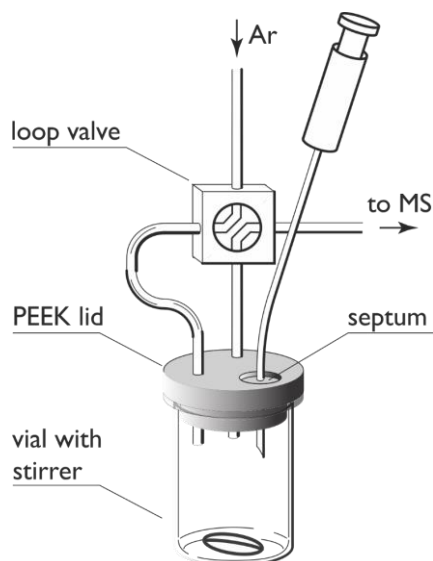


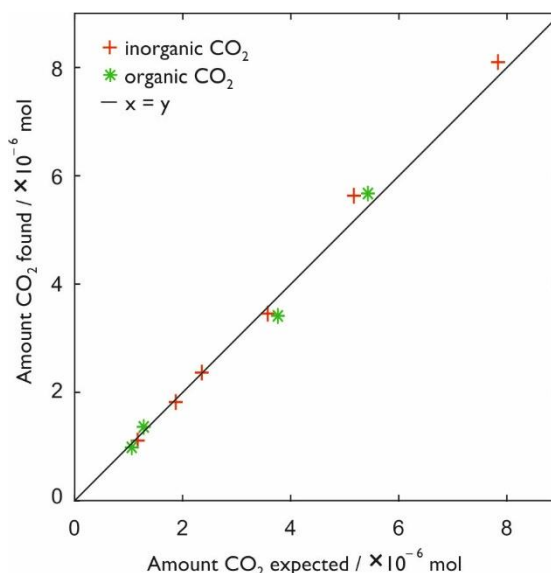
Figure 81: Schematic of the sample setup consisting of vial with stirrer, PEEK lid with septum, purge tubing with a loop valve and a syringe.

5.2.2 Calibration

Carbonaceous Compounds

Different amounts of Li_2CO_3 were analysed by adding 400 μL of a 0.1 M H_2SO_4 solution to investigate the evolution of inorganic CO_2 . For organic carbonates, sodium acetate (NaAc) was decomposed by adding first 0.5 mL 0.5 M FeSO_4 in 0.1 M H_2SO_4 and then dropwise adding 0.1 mL 10% H_2O_2 in 0.1 M H_2SO_4 . In Figure 82 the measured values are compared to the theoretical ones.

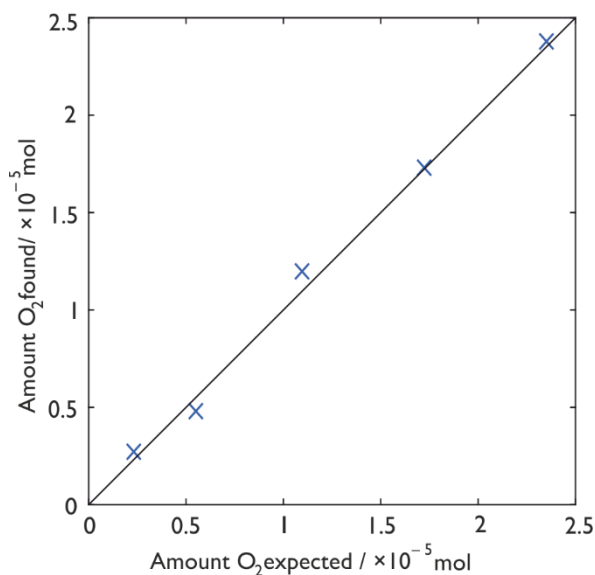
Figure 82: Calibration curve of inorganic (red crosses) and organic (green stars) CO_2 measured using $\text{Li}_2\text{CO}_3/\text{NaAc}$ mixtures. Linear regression gives for the inorganic CO_2 $n_{\text{CO}_2,\text{found}} = 1.033 \cdot n_{\text{CO}_2,\text{expected}}$ with $R^2 = 0.9954$ and for the organic CO_2 $n_{\text{CO}_2,\text{found}} = 0.999 \cdot n_{\text{CO}_2,\text{expected}}$ with $R^2 = 0.986$.



Peroxides and Superoxides via O₂ Evolution

Different amounts of Li_2O_2 were decomposed to O_2 using 500 μL of a 0.1 M FeCl_3 solution in distilled water. The peroxide samples were prepared under argon in the MS setup and measured with a gas flow of 5 mL/min. In Figure 83 the measured values are compared to the theoretical ones.

Figure 83: Comparison of the amount of Li_2O_2 used and O_2 evolved using 0.1 M FeCl_3 dissolved in distilled H_2O . Linear regression gives $n_{\text{O}_2,\text{found}} = 1.015 \cdot n_{\text{O}_2,\text{expected}}$ with $R^2 = 0.9948$.



Peroxides and Superoxides via a $[\text{Ti}(\text{O}_2)\text{OH}]^+$ Complex

The yellow/orange complex was quantified using UV-Vis spectrometry. For the calibration, a H_2O_2 solution (30 wt%), diluting it with 0.1 M H_2SO_4 to suitable values was used. As complexing agent a

2 wt% Ti(IV)-oxysulfate solution was used. Normally, about 500 μL of the solution were added to the in 100-200 μL 0.1 M H_2SO_4 dissolved peroxide. Following dilution steps were applied depending on the concentration of peroxide in the initial solution to obtain a mixture well in the linear absorption region. The absorption maximum at 405 nm was chosen for all measurements. The calibration curve is given in Figure 84a and an exemplary UV-Vis spectrum in Figure 84b.

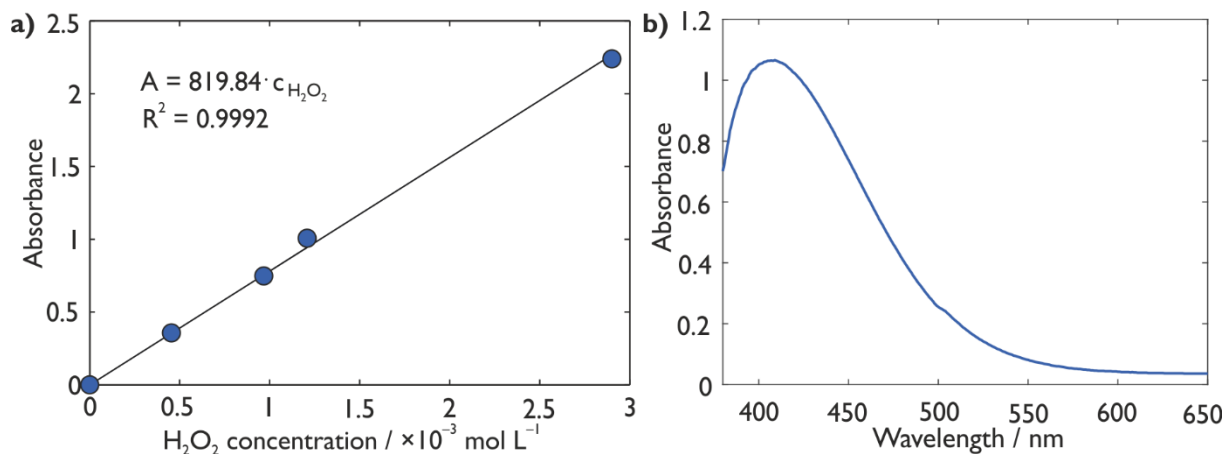
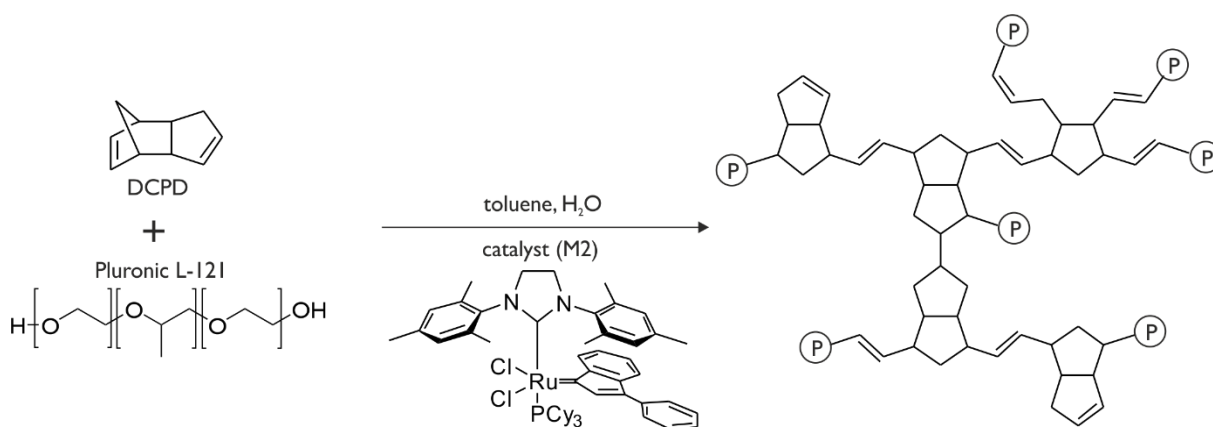


Figure 84: Calibration of the $\text{Ti}(\text{O}_2)\text{SO}_4$ complex using UV/Vis spectroscopy; a) calibration curve: absorption at 403 nm was correlated to the concentration of H_2O_2 weight in; b) typical UV-Vis curve.

5.3 Preparative Work

5.3.1 High Internal Phase Emulsion Polymerisation of Dicyclopentadiene



The amount of water can be calculated using following formula:

$$\text{porosity} = \frac{m_{\text{H}_2\text{O}}}{m_{\text{H}_2\text{O}} + m_{\text{DCPD}} + m_{\text{toluene}}} \quad (58)$$

In a typical batch, about 6 g (45 mmol) melted dicyclopentadiene (DCPD) and 420 mg Pluronic L-121 (7 wt% regarding the DCPD) were mixed in a 100 mL three necked round bottom flask. About 100 μL toluene were added to keep the DCPD liquid. The clear solution was mixed with a mechanical stirrer and 24.5 mL distilled water (when a porosity of 80% should be achieved) were added using a dropping funnel. The solution immediately turned opaque and the stirring was continued for about one hour after the water addition was completed. 3 mg (molar ratio was 1:15 000) [1,3 -Bis(2,4,6-trimethylphenyl) -2-imidazolidinylidene]dichloro(3 -phenyl -1H-inden -1-ylidene)(tricyclo- hexyl-phosphine) ruthenium(II) (M2) dissolved in 50 mL toluene were added to the opaque, foamy and gel-like mixture.

The now slightly pink blend was filled in moulds and cured at 80 °C for two hours. The now colourless, opaque discs were oxidised at 40 °C overnight or at ambient conditions over a week and consequently turned yellow.

Carbonisation with CO₂ Activation of the pDCPD-HIPEs

The oxidised HIPEs were heated to 900 °C/1100 °C under argon/CO₂ for varying amounts of time.

Table 13: Carbonisation experiments of pDCPD-HIPEs with an initial porosity of 80%. The abbreviations correspond to mass (m), diameter (d) and height (h).

T / °C	time / h		before heating			after Ar			after CO ₂		
	Ar	CO ₂	m / mg	h / mm	d / mm	m / mg	h / mm	d / mm	m / mg	h / mm	d / mm
900	2 h	2 h ^a	240.1	1.07	24.74	40.1	0.69	16.15	- ^b	-	-
900	2 h	2 h ^a	379.8	2.09	31.02	116.0	1.41	20.24	68.3	1.31	17.97
900	2 h	2 h ^a	4975	26.42	25.47	582.1 ^c	11.3	15.60	286.1	10.5	14.41
		1 h ^a				932.9 ^c	17.66	16.70	630.6	16.97	16.13
900	2 h	1 h ^a	171.6	1.05	30.83	48.6	0.82	19.24	38.5	0.69	18.16
900	2 h	1 h ^a	209.0	1.04	30.85	60.3	0.73	19.35		0.81	6.4
900	2 h	2 h	154.5	1.05	26.93	- ^d	-	-	24.6	0.69	16.34
900	2 h	2 h	143.5	1.06	27.14	- ^d	-	-	37	0.88	16.46
900	2 h	2 h	4683	24.17	25.5	- ^d	-	-	1237	15.93	16.97
1100	2 h	1 h	3961	22.15	25.78	- ^d	-	-	610.5	13.67	16.62
1100	2 h	1 h	121.3	1.08	24.76	- ^d	-	-	- ^b	-	-
1100	2 h	1 h	116.8	0.99	29.19	- ^d	-	-	- ^b	-	-

^a) cooling to room temperature before heating up again for the activation with CO₂; ^b) sample was consumed during the heating step; ^c) big monolith was split before the next activation step; ^d) no values given as the material was directly activated in the same heating step.

Table 14: Characteristics of the activated and carbonised samples; the open porosity was obtained by filling the sample with TEGDME, the surface area was calculated using BET and the pore diameter obtained by BJH analysis.

temp.	heating		mass loss	bulk density	porosity	open porosity	surface area	pore diameter
	carb.	act.						
900 °C	2 h	2 h	77%	0.273 g cm ⁻³	88%	65%	668 m ² g ⁻¹	3.42 nm
900 °C	2 h	1 h	71%	0.234 g cm ⁻³	90%	88%	734 m ² g ⁻¹	5.45 nm
900 °C	2 h	2 h	84%	0.175 g cm ⁻³	93%	61%	1065 m ² g ⁻¹	5.46 nm
1100 °C	2 h	1 h	85%	0.223 g cm ⁻³	90%	72%	814 m ² g ⁻¹	4.01 nm

Determination of the Density and Porosity

A small volume of 0.2-0.5 mL was defined in a vial using distilled water. Then, the bulk density was measured by weighting the amount of carbonised, ground material fitting in that volume. The open porosity was calculated by adding as much organic solvent (toluene and TEGDME were used) as possible to fill all the pores of the powder. The porosity could be calculated following Equation (59).

$$\Phi = \left(1 - \frac{\rho_{bulk}}{\rho_{particle}}\right) \times 100 \quad (59)$$

Here, Φ is the total porosity, while ρ_{bulk} is the density measured with the ground material and $\rho_{particle}$ is the density of pure carbon in the graphite modification (= 2.26 g cm⁻³).

HIPE with DCPD and Cyclohexane

The general DCPD-HIPE did not change, except the addition of different amounts of cyclohexane to the mixture and the curing at 40 °C instead of 80 °C. The cyclohexane was added to the round bottom flask together with the DCPD and the surfactant.

Table 15: Amounts used for the use of a porogenic solvent in the HIPE-setup.

ratio	DCPD / g	CH / g	Pluronic / g	water / mL	M2 / mg
1:0	6.007	-	0.428	24	4.8
1:0.2	5.996	1.20	0.500	22.8	4.7
1:0.5	6.009	3	0.620	21	4.8
1:1	6.011	6	0.841	18	4.9
1:1.5	6.050	9.08	1.058	15.2	4.9
1:2	6.006	12	1.260	12	4.7

After the curing, the samples were dried under ambient conditions or using freeze drying.

5.3.2 TiO₂ based Materials

TiO₂ Nanoparticles

The used as received colourless nanoparticles were heated to different temperatures under air/argon. For all experiments the heating rate was 5 K/min and left at the wanted temperature for two hours. All samples were cooled down to room temperature.

Table 16: XRD and CV results for the heated TiO₂ samples.

	5 nm			20 nm		
	anatase	rutile	capacity / mAh g ⁻¹	anatase	rutile	capacity / mAh g ⁻¹
20 °C	100%	-	-	83%	17%	-
400 °C (air)	100%	-	-	83%	17%	234
400 °C (Ar)	100%	-	86	83%	17%	123
800 °C (air)	21%	80%	3.4	99%	1%	2.8
800 °C (Ar)	29%	71%	2.7	99%	1%	6.5

TiO_{2-x} nanorods¹⁵²



Different TiO₂ nanorods were synthesised following Sun *et al.* with the goal to obtain a varying oxygen content. For all synthesis, 0.5 g TiN was dispersed in 30 mL of a 4.0 M HCl/HNO₃ for 30 minutes and subsequently heated to 180 °C in an autoclave for different periods of time. After cooling down to room temperature, the mixture was centrifuged and washed with distilled water until the mixture had a pH of 7. The obtained solid was dried at 80 °C overnight and analysed using XRD, SEM, EDX and electrochemical testing.

Table 17: Exact synthesis conditions for the different TiO₂/TiN nanorod mixtures.

acid	heating time	comments	composition		capacity
			TiN	TiO ₂ (rutile)	
-	-	reactant; brown solid	100%	-	-
HCl	2 h	dark grey solid in yellow solution	47%	53%	-
HCl	4 h	grey solid in green solution	63%	37%	67 mAh g ⁻¹
HCl	12 h	blue/grey solid in green solution	45%	55%	198 mAh g ⁻¹
HNO ₃	24 h	yellow solid in colourless solution	-	100%	-

5.3.3 Electrospinning of Ti Containing Materials

Self-Made Fibres¹⁵³

To 300 mL DMF, first 34.2 mL titanium(IV)n-butoxide (10 wt%), then 30.1 mL furfuryl alcohol (10 wt%) and finally 8.55 g acetic acid (2.5 wt%) were added. Subsequently, 34.2 g polyvinylpyrrolidone (PVP, $M_w = 1\,300\,000$, 10 wt%) were slowly dissolved over a time period of four hours. The now dark orange solution was stirred overnight and stored in the fridge prior to use.

The spinning was performed with a Nanospider NS LAB 500 in Maribor. For all tests, approximately 50 mL of the previously prepared solution were used and the applied parameters were changed for the different tests (cf. Table 18).

Table 18: Used parameters for the different electro spinning approaches.

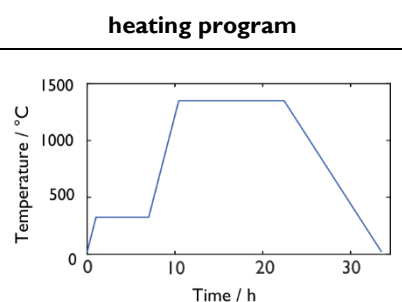
	solution	potential	rotation	distance	comments
f_1	50 mL	15 → 75 kV	3.8 rpm	160 mm	potential was slowly increased until a fibre formation was visible; gelation observed
f_2	50 mL	50 kV	3.8 rpm	160 mm	decrease of potential did not result in less/late gelation
f_3	40 mL	75 kV	5 rpm	160 mm	fast gelation but a few fibres visible
f_4	50 mL	75 kV	6 rpm	160 mm	roller setup did not result in a fibre formation
f_5	50+50 mL	75 kV	6 rpm	160 mm	a few fibres could be obtained but the solution still jellified after a short time period
f_6	50 mL	75 kV	7.5 rpm	160 mm	

After the electrospinning process, both the obtained fibres and the formed gel were dried for a few days. The gelled material was vacuum dried to remove the DMF before further steps. Subsequently the different test materials were carbonised following the procedure published by Fong *et al.* and resulting in white (fibres) and dark grey (gel) materials.

Table 19: Results of the electro spun fibres carbonised with the mentioned heating program.

	before heating	after heating	mass loss	XRD	
				TiC	TiO₂
f_1	337 mg	33.6 mg	90%	-	100%
f_5	685 mg	82 mg	88%	-	100%
f_6	1013 mg	133.7 mg	87%	-	100%
g_1	4.30 g	841 mg	80%	80% ^a	20%
g_2	5.80 g	1.30 g	78%	80% ^a	20%

^aconsisting of TiC and TiCN in a ratio of 1:1.



Carbonisation of Purchased Fibres

Two materials from Pardam nanotechnology, which electro spun containing a TiO₂ material, are carbonised using different heating programs. The material called ELSP consists of TiO₂ in the spider modification, has a fibre diameter of 300-700 nm and looks like yellow paper. FCSP contains TiO₂ in the rutile modification, has a beige, cotton like appearance and the fibres have a size of 400–1000 nm. Both materials were carbonised under argon with three different heating programs and analysed with SEM, XRD and EDX.

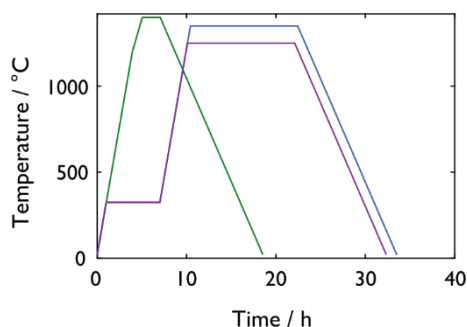


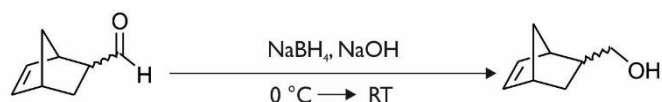
Figure 85: Different heating programs used for the carbonisation of the electrospun fibres.

Table 20: Heating programs and carbonisation results of the professionally prepared fibres.

		before heating	after heating	XRD		EDX ^a			comment
				TiO ₂	TiC	C	O	Ti	
1250 °C	ELSP	325 mg	79.9 mg	100%	-	-	86	14	colourless, hard, slightly grey solid
	FCSP	324 mg	81.7 mg	100%	-	4	56	40	colourless, soft solid
1350 °C	ELSP	236 mg	61 mg	100%	-	-	82	18	hard colourless solid
	FCSP	201.4 mg	48 mg	100%	-	-	89	11	hard colourless solid
1400 °C	ELSP	542 mg	117.6 mg	24%	76%	4	27	69	soft, brittle grey/black solid
	FCSP	226.3 mg	53 mg	99%	1%	-	68	32	greyish colourless solid

^aEDX results in atomic%.

5.3.4 5-Norbornene-2-methanol¹⁷⁴



0.81 g (21.4 mmol, 1.0 eq) sodium borohydride were dispersed in 10 mL of a 2 M sodium hydroxide solution in a 100 mL three necked round bottom flask equipped with a drying tube and a dropping funnel. The mixture was cooled to 0 °C with an ice bath. Subsequently, 5.4 g (44.3 mmol, 2 eq) 5-norbornene-2 carboxaldehyde dissolved in 30 mL methanol were added over an hour using the dropping funnel. After complete addition, the ice bath was removed and the mixture was stirred overnight. The conversion was monitored *via* TLC.

After complete conversion, the solution was neutralised to pH 6 using diluted H₂SO₄. The methanol was removed under reduced pressure and the now aqueous solution was extracted three times with 50 mL Et₂O each. The combined organic phases were washed with saturated NaHCO₃-solution (3 times 100 mL), dried over Na₂SO₄ and the solvent was removed under reduced pressure. The crude product was purified using column chromatography (CH/EA 10+1 → 5+1).

C₈H₁₂O [124.8]

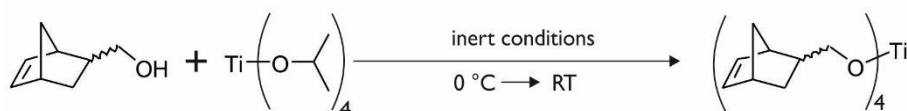
Yield 3.27 g yellow solution (59.2%)

R_f (CH/EA 5+1) 0.23

¹H-NMR (CDCl₃, 25 °C, δ (ppm) = 6.12-6.06 (m, 1H, 5-endo), 6.06-6.00 (m, 0.6H, 5,6-exo), 5.94-5.88 (m, 1H, 6-endo), 3.63 (dd, 0.3H, ³J_{HH} = 6.45 Hz, ⁴J_{HH} = 4.05 Hz, c-exo), 3.46 (dd, 0.3 H, ³J_{HH} = 8.85 Hz, ⁴J_{HH} = 1.2 Hz, c-exo), 3.32 (dd, 1 H, ³J_{HH} = 6.6 Hz, ⁴J_{HH} = 3,75 Hz, c-endo), 3.18 (dd, 1H, ³J_{HH} = 9.12 Hz, ⁴J_{HH} = 1.08 Hz, c-endo), 2.88 (s, 1H, 1,4-endo), 2.76 (s, 1.3H, 1,4-endo, 1,4-exo), 2.71 (s, 0.3H, 1,4-exo), 2.24 (m, 1H, 2-endo), 1.76 (m, 1H, 3-endo), 1.56 (m, 0.3H, 2-exo), 1.43-1.36 (m, 1.4H, b-exo, b-endo), 1.29-1.24 (m, 0.4H, 3-exo), 1.24-1.15 (m, 1.4H, b-endo, b-exo), 1.09-1.02 (m, 0.3H, 3-exo), 0.46 (m, 1H, 3-endo).

$^{13}\text{C}\{^1\text{H}\}$ -NMR (CDCl_3 , 25 °C, δ (ppm) = 137.4, 132.2 (2C, 5-endo, 6-endo), 136.8, 136.5 (2C, 5-exo, 6-exo), 67.3 (1C, C-exo), 66.30 (1C, C-endo), 49.5 (1C, b-endo), 45.0 (1C, b-exo), 43.6 (1C, 4-endo), 43.2 (1C, 4-exo), 42.24 (1C, 1-endo), 41.8 (1C, 1-exo), 41.6 (1C, 2-endo), 41.6 (1C, 2-exo), 29.6 (1C, 3-exo), 28.9 (1C, 3-endo).

5.3.5 Tetra(5-norbornene-2-methoxy)titanate¹⁵⁴



A 50 mL three necked round bottom flask was evacuated, heated and flushed with nitrogen three times to perform the reaction under inert conditions. 2 mL (6.8 mmol, 1.0 eq) tetraisopropyltitanate were cooled to 0 °C using an ice bath. 3.4 mL (28 mmol, 4.1 eq) 5-norbornene-2-methanol were slowly added with a syringe. The clear, yellow solution was stirred over night at room temperature. On the next morning, the side product (isopropanol) was removed under reduced pressure without exposing the mixture to air. A slightly yellow solid was obtained which was stored in an argon filled glovebox and used without further purification.

$\text{C}_{32}\text{H}_{44}\text{O}_4\text{Ti}$ [540.27]

Yield 3.014 g slightly yellow solid (82%)

Melting range 160-190 °C

Homo-polymerisation of the Ti-Norbornene

For a typical $\text{Ti}(\text{Norb})_4$ polymerisation, the monomer was weighed in an argon filled glovebox (between 300 and 400 mg were used for one polymerisation) and the dry solvent (toluene or cyclohexanone) was added without exposure to air. After the monomer was dispersed (toluene) or dissolved (cyclohexanone) in the solvent using an ultrasonic bath, the initiator (M2) was added in a ratio of 1:5000 mol%. The monomer/catalyst mixture was polymerised at 80 °C overnight using either a glass vial or a Teflon[®] mould. Subsequently, a solvent exchange in acetone was performed and the material was dried before it was carbonised at 1100 °C/1400 °C under argon.

Table 21: Different polymerisation setups and characteristics of the carbonised polymers.

	Ti-Norb	solvent	disc	temperature	mass loss	characterisation
5	328 mg	300 μL	327 mg	1100 °C	83%	grey, metallic, broken
6	406 mg	200 μL	160 mg	1100 °C	82%	brittle, grey
7	306 mg	1 mL	155 mg	1300 °C	79%	brittle, greyish black
8	401 mg	1 mL	61.1 mg	1320 °C	80%	light grey

Co-polymerisation of the Ti-Norbornene

Dicyclopentadiene was dissolved in 100 μL toluene and subsequently $\text{Ti}(\text{Norb})_4$ was dispersed using the ultrasonic bath. After the initiator (1:7000 mol%) was added, the mixture was filled in Teflon[®] moulds and cured at 80 °C for two hours. The solid and strong discs were dried overnight and carbonised at 1380 °C for two hours under argon.

Table 22: Polymerisation and carbonisation results of the performed co-polymerisations.

	DCPD	Ti-Norb	mass before	mass loss	volume loss	height loss	XRD	
							TiO ₂	TiC
1	0.8 g	0.8 g	1.418 g	85%	32.5%	28%	0.5%	99.5%
2	1.2 g	0.4 g	1.365 g	80%	45.5%	27.5%	94% ^a	6% ^a
3	1.5 g	0.3 g	1.2939 g	80%	46%	32%	- ^a	100% ^a

^a)hardly any crystallinity visible using XRD analysis.

5.3.6 Modification of a DCPD-HIPE with a Ti-source

Ti-Isopropoxide + pDCPD-HIPE

(Un-)oxidised pDCPD discs are soaked with Ti-isopropoxide using an ultrasonic bath. This process is performed under nitrogen to prevent the sol-gel process happening ahead of time. After a soaking time of half an hour, a few drops of distilled water are added and a colourless solid starts precipitating. The discs are dried under ambient conditions and excess TiO₂ on the surface is removed. Subsequently, the samples are heated to different plateaus under argon atmosphere applying a heating rate of 2 °C min⁻¹ and staying at the heating plateau for four hours.

Table 23: Modification of oxidised pDCPD discs with Ti(i-Pr)₄ and subsequent carbonisation.

	mass before	mass TiO ₂	heating	mass loss	diameter loss	height loss	XRD	
							TiO ₂	TiC
1i	56.8 mg	88 mg	1100 °C	26%	22%	26%	72%	28 %
2i	94.9 mg	99.4 mg	1400 °C	64%	48%	57%	100%	-
3i	68.1 mg	66.9 mg	1400 °C	65%	51%	52%	100%	-
4i	97.1 mg	93.6 mg	1400 °C	65%	47%	52%	100%	-
5i	77.9 mg	81.9 mg	1400 °C	64%	51%	49%	100%	-
6i	92.1 mg	97.3 mg	1400 °C	68%	29%	37%	15%	85%
7i	76.6 mg	87.7 mg	1400 °C	70%	33%	28%	15%	85%
8i	92.1 mg	95.2 mg	1400 °C	69%	30%	32%	15%	85%
9i	73.4 mg	91.6 mg	1400 °C	68%	-	-	36%	64%
10i	50.9 mg	49.1 mg	1400 °C	71%	30%	42%	36%	64%
11i	39.7 mg	39.7 mg	1400 °C	69%	-	46%	36%	64%
12i	32.1 mg	38.9 mg	1400 °C	66%	31%	36%	36%	64%
13 ^{ia}	68 mg	86.7 mg	1400 °C	68%	36%	-	24%	76%
14 ^{ia}	54.9 mg	93.1 mg	1400 °C	64%	44%	50%	24%	76%
15 ^{ia}	67.2 mg	85.6 mg	1400 °C	67%	33%	51%	24%	76%
16 ^{ia}	54.9 mg	93.4 mg	1400 °C	63%	47%	49%	24%	76%

^a)un-oxidised pDCPD discs were used.

Ti-Isopropoxide + Trimethylsilylcellulose (TMSC) + pDCPD-HIPE

100-500 mg TMSC were dissolved in 2-5 mL toluene (dry) and mixed with 0.2-1 mL Ti(i-Pr)₄ in a nitrogen flushed vial. (Un)oxidised pDCPD discs are soaked with the solution using an ultrasonic bath. After half an hour a few drops of 5 wt% HCl were added and a colourless solid started to precipitate. The discs were dried under ambient conditions and excess TiO₂ on the surface was removed. Subsequently, the samples are carbonised under argon atmosphere for four hours at different heating plateaus.

Table 24: Modification of oxidised pDCPD discs with Ti(i-Pr)₄ and TMSC and subsequent carbonisation.

	mass before	mass TiO ₂ + cellulose	heating	mass loss	diameter loss	height loss	XRD	
							TiO ₂	TiC
1t ^a	96.7 mg	24.1 mg	1100 °C	72%	26%	24%	99.5%	0.5%
2t ^a	78.6 mg	17.7 mg	1100 °C	73%	28%	27%	99.5%	0.5%
3t ^a	98.9 mg	30.5 mg	1100 °C	78%	30%	29%	99.5%	0.5%
4t ^a	79.7 mg	23.2 mg	1100 °C	80%	30%	35%	99.5%	0.5%
5t ^b	95.9 mg	45.3 mg	1400 °C	85%	-	-	14%	86%
6t ^b	78.5 mg	42.5 mg	1400 °C	87%	-	-	14%	86%
7t ^b	82.4 mg	34.9 mg	1400 °C	89%	-	-	14%	86%
8t ^b	78.1 mg	28.1 mg	1400 °C	90%	-	-	14%	86%
9t ^b	92.6 mg	34.2 mg	1400 °C	85%	59%	61%	99.5%	0.5%
10t ^b	77.4 mg	29.3 mg	1400 °C	86%	68%	74%	99.5%	0.5%
11t ^b	92.2 mg	40 mg	1400 °C	88%	67%	58%	99.5%	0.5%
12t ^b	78.2 mg	24.6 mg	1400 °C	87%	65%	59%	99.5%	0.5%
13t ^b	51 mg	17.6 mg	1400 °C	90%	77%	30%	99.5%	0.5%
14t ^b	40.9 mg	8.4 mg	1400 °C	86%	-	-	99.5%	0.5%
15t ^b	33.5 mg	8.4 mg	1400 °C	88%	-	-	99.5%	0.5%
16t ^{b,e}	68.4 mg	51.1 mg	1400 °C	70%	-	-	71%	29%
17t ^c	192.7 mg	112.5 mg	1400 °C ^d	70%	-	-	12%	88%
18t ^c	380.2 mg	184.8 mg	1400 °C ^d	76%	26%	27%	12%	88%

^a)100 mg TMSC in 1 mL toluene and 200 µL Ti(i-Pr)₄ were used; ^b)200 mg TMSC in 2 mL toluene and 500 µL Ti(i-Pr)₄ were used; ^c)500 mg TMSC in 5 mL toluene and 1 mL Ti(i-Pr)₄ were used; ^d)only left at the plateau for 2 hours; ^e)un-oxidised pDCPD-disc was used.

Ti-Norbornene + pDCPD-HIPE

Ti-Norbornene was dissolved in toluene and the previously oxidised pDCPD – HIPEs are soaked with the mixture using an ultrasonic bath. To prevent hydrolysis, the used vial was flushed with nitrogen beforehand. After half an hour, 1:5000 mol% initiator (M2) dissolved in 50 µL toluene were added and the disc was cured in a Teflon mould at 80 °C for 2 hours. Subsequently the samples were carbonised under argon atmosphere applying heating rate of 2 °C min⁻¹ and staying at the heating plateau for 2/4 hours.

Table 25: Modification of the pDCPD with Ti(Norb)₄ und subsequent carbonisation.

	mass before	mass Ti-Norb	heating	mass loss	diameter loss	height loss	XRD	
							TiO ₂	TiC
1n	96.9 mg	60 mg	1100 °C ^a	84%	26%	29%	94.5%	5.5%
2n	97.4 mg	60 mg	1100 °C ^a	84%	26%	26%	94.5%	5.5%
3n	201.7 mg	61.8 mg	1400 °C	83%	32%	50%	1.5%	98.5%
4n	382 mg	80 mg	1400 °C	81%	-	-	1.5%	98.5%
5n	218.3 mg	12.5 mg	1250 °C	66%	-	27%	30%	70%
6n	95.4 mg	11.6 mg	1250 °C	64%	27%	26%	30%	70%
7n	90.7 mg	14.7 mg	1250 °C	70%	29%	30%	30%	70%
8n	505.5 mg	68.6 mg	1400 °C	80%	-	-	13%	87%
9n	196.8 mg	34.9 mg	1400 °C	78%	-	-	12.5%	87.5%
10n	185.2 mg	61.1 mg	1400 °C	85%	-	-	12.5%	87.5%
11n	71.3 mg	22.7 mg	1400 °C	89%	-	-	12.5%	87.5%
12n	1604.2 mg ^c	978.3 mg	1400 °C	91%	-	-	15%	85%
13n	713.2 mg ^c	288.3 mg	1400 °C ^b	93.5%	-	-	80%	20%
14n	1157.6 mg ^c	257.5 mg	1300 °C	65.5%	-	-	17%	83%
15n	1106.9 mg ^c	475.4 mg	1300 °C	83%	-	-	1%	99%
16n	394.5 mg	187.5 mg	1350 °C	77%	25%	25%	-	100%
17n	396.8 mg	167.2 mg	1350 °C	78%	27%	25%	-	100%
18n	399 mg	154.4 mg	1300 °C	75%	28%	29%	-	100%
19n	387 mg	169.4 mg	1320 °C	72%	27%	26%	7%	93%

^a) temperature held for 4 hours; ^b)temperature held for 8 hours; ^c)masses of more samples summed up.

Abbreviations

abbreviation	explanation
A	ampere
a%	atomic percent
C	Celsius
ch	charge
CH	cyclohexane
CHO	cyclohexanone
cm	centimetre
DABCO	1,4-diazabicyclo [2.2.2] octane
DBBQ	2,5-di-tert-butyl-1,4-benzoquinone
DCE	dichloroethane
dch	discharge
DCPD	dicyclopentadiene
dispr.	disproportionation
DMA	9,10-dimethylanthracene
DMAc	9,10-dimethylacetamide
DMC	dimethyl carbonate
DME	ethylene glycol dimethyl ether
DMF	dimethylformamide
DMSO	dimethylsulfoxide
DN	donor number
DPA	diphenylanthracene
e ⁻	electron
EA	ethyl acetate
EDX	energy dispersive X-ray
Et ₂ O	diethyl ether
FA	furfuryl alcohol
h	hour
HIPE	high internal phase emulsion
ISC	inter system crossing
J	Joule
k	quenching rate
KB	ketjenblack
kg	kilogram
L	litre
LFP	lithium iron phosphate
LiFo	lithium format
Li-O ₂ battery	lithium oxygen batteries
Li-S battery	lithium sulfur battery
M	molar
m	milli
M2	[1,3 -Bis(2,4,6-trimethylphenyl) -2-imidazolidinylidene]dichloro(3 -phenyl -1H-inden -1-ylidene)(tricyclo- hexylphosphine)ruthenium(II)
min	minute
MeCN	acetonitrile
MHz	mega Hertz
MS	mass spectrometry
n	nano
NCA	LiNi _{0.8} Co _{0.15} Al _{0.05} O ₂
NMR	nuclear magnetic resonance
Norb	norbornene
¹ O ₂	singlet oxygen
³ O ₂	triplet oxygen
O ₂ ⁻	superoxide
OEMS	online electrochemical mass spectrometry
OER	oxygen evolution reaction
ORR	oxygen reduction reaction
p	pressure

pDCPD	polymerised dicyclopentadiene
PEEK	polyether ether ketone
ppm	parts per million
PVP	polyvinylpyrrolidone
R&D	research and development
rpm	rounds per minute
RT	room temperature
s	second
S	Siemens
SEI	solid electrolyte interface
SEM	scanning electron microscopy
sol	solvated
SP	SuperP
TEGDME	tetra ethylene glycol dimethyl ether
THF	tetrahydrofuran
TiBO	titanium(IV) n-butoxide
Ti(Norb) ₄	titanium-norbornene
Ti(i-Pr) ₄	titanium-isopropoxide
TMSC	tri-methyl-silyl cellulose
PTFE	polytetrafluoroethylene
TLC	thin layer chromatography
UV	ultraviolet
V	Volts
Vis	visual
vol%	volume percent
vs.	versus
w/o	without
Wh	Watt hour
wt%	weight percent
XRD	X-ray diffraction
μ	mikro
ρ	density

Bibliography

- (1) Bruce, P. G.; Freunberger, S. A.; Hardwick, L. J.; Tarascon, J.-M. *Nat. Mater.* **2011**, *11*, 19.
- (2) Sharon, D.; Hirshberg, D.; Afri, M.; Frimer, A. A.; Noked, M.; Aurbach, D. *J. Solid State Electrochem.* **2017**, *21* (7), 1861–1878.
- (3) Mahne, N.; Fontaine, O.; Thotiyil, M. O.; Wilkening, M.; Freunberger, S. A. *Chem. Sci.* **2017**, *8* (10), 6716–6729.
- (4) Freunberger, S. A. *Nat. Energy* **2017**, *2*, 17091.
- (5) Semkow, K. W. *J. Electrochem. Soc.* **1987**, *134* (8), 2084.
- (6) Abraham, K. M.; Jiang, Z. *J. Electrochem. Soc.* **1996**, *143* (1), 1–5.
- (7) Luntz, A. C.; McCloskey, B. D. *Chem. Rev.* **2014**, *114* (23), 11721–11750.
- (8) Li, F.; Chen, J. *Adv. Energy Mater.* **2017**, 201602934, 1–12.
- (9) Johnson, L.; Li, C.; Liu, Z.; Chen, Y.; Freunberger, S. A.; Ashok, P. C.; Praveen, B. B.; Dholakia, K.; Tarascon, J.-M.; Bruce, P. G. *Nat. Chem.* **2014**, *7* (1), 87–87.
- (10) McCloskey, B. D.; Scheffler, R.; Speidel, A.; Girishkumar, G.; Luntz, A. C. *J. Phys. Chem. C* **2012**, *116* (45), 23897–23905.
- (11) Viswanathan, V.; Thygesen, K. S.; Hummelshøj, J. S.; Nørskov, J. K.; Girishkumar, G.; McCloskey, B. D.; Luntz, A. C. *J. Chem. Phys.* **2011**, *135* (21).
- (12) Adams, B. D.; Radtke, C.; Black, R.; Trudeau, M. L.; Zaghbi, K.; Nazar, L. F. *Energy Environ. Sci.* **2013**, *6* (6), 1772.
- (13) Laoire, C. O.; Mukerjee, S.; Abraham, K. M.; Plichta, E. J.; Hendrickson, M. A. *J. Phys. Chem. C* **2010**, *114* (19), 9178–9186.
- (14) Kwabi, D. G.; Bryantsev, V. S.; Batcho, T. P.; Itkis, D. M.; Thompson, C. V.; Shao-Horn, Y. *Angew. Chemie - Int. Ed.* **2016**, *55* (9), 3129–3134.
- (15) Gutmann, V. *Coord. Chem. Rev.* **1976**, *18* (2), 225–255.
- (16) Burke, C. M.; Pande, V.; Khetan, A.; Viswanathan, V.; McCloskey, B. D. *Proc. Natl. Acad. Sci.* **2015**, *112* (30), 9293–9298.
- (17) Mahne, N.; Schafzahl, B.; Leypold, C.; Leypold, M.; Grumm, S.; Leitgeb, A.; Strohmeier, G. A.; Wilkening, M.; Fontaine, O.; Kramer, D.; Slugovc, C.; Borisov, S. M.; Freunberger, S. A. *Nat. Energy* **2017**, *2*, 17036.
- (18) Kwabi, D. G.; Batcho, T. P.; Feng, S.; Giordano, L.; Thompson, C. V.; Shao-Horn, Y. *Phys. Chem. Chem. Phys.* **2016**, *18* (36), 24944–24953.
- (19) Khetan, A.; Luntz, A.; Viswanathan, V. *J. Phys. Chem. Lett.* **2015**, *6* (7), 1254–1259.
- (20) Gao, X.; Chen, Y.; Johnson, L.; Bruce, P. G. *Nat. Mater.* **2016**, *15* (8), 882–888.
- (21) Radin, M. D.; Siegel, D. J. *Energy Environ. Sci.* **2013**, *6* (8), 2370.
- (22) Lim, H.-D.; Lee, B.; Bae, Y.; Park, H.; Ko, Y.; Kim, H.; Kim, J.; Kang, K. *Chem. Soc. Rev.* **2017**, *46* (10), 2873–2888.
- (23) Kang, S.; Mo, Y.; Ong, S. P.; Ceder, G. *Chem. Mater.* **2013**, *25* (16), 3328–3336.
- (24) Sharon, D.; Hirsberg, D.; Afri, M.; Chesneau, F.; Lavi, R.; Frimer, A. A.; Sun, Y.-K.; Aurbach, D. *ACS Appl. Mater. Interfaces* **2015**, *7* (30), 16590–16600.
- (25) Landa-Medrano, I.; Pinedo, R.; Ortiz-Vitoriano, N.; De Larramendi, I. R.; Rojo, T. *ChemSusChem*

- 2015, 8 (23), 3932–3940.
- (26) Lee, H.; Kim, Y.-J.; Lee, D. J.; Song, J.; Lee, Y. M.; Kim, H.-T.; Park, J.-K. *J. Mater. Chem. A* **2014**, 2 (30), 11891.
- (27) Hu, X.; Han, X.; Hu, Y.; Cheng, F.; Chen, J. *Nanoscale* **2014**, 6 (7), 3522.
- (28) Luo, W.-B.; Gao, X.-W.; Chou, S.-L.; Kang, Y.-M.; Wang, J.-Z.; Liu, H.-K.; Dou, S.-X. *Adv. Energy Mater.* **2017**, 7 (24), 1700234–n/a.
- (29) Kundu, D.; Black, R.; Berg, E. J.; Nazar, L. F. *Energy Environ. Sci.* **2015**, 8 (4), 1292–1298.
- (30) Gowda, S. R.; Brunet, A.; Wallraff, G. M.; McCloskey, B. D. *J. Phys. Chem. Lett.* **2013**, 4 (2), 276–279.
- (31) Shao, Y.; Ding, F.; Xiao, J.; Zhang, J.; Xu, W.; Park, S.; Zhang, J. G.; Wang, Y.; Liu, J. *Adv. Funct. Mater.* **2013**, 23 (8), 987–1004.
- (32) Wood, K. N.; Noked, M.; Dasgupta, N. P. *ACS Energy Lett.* **2017**, 2 (3), 664–672.
- (33) Younesi, R.; Hahlin, M.; Roberts, M.; Edström, K. *J. Power Sources* **2013**, 225, 40–45.
- (34) Ogasawara, T.; Débart, A.; Holzapfel, M.; Novák, P.; Bruce, P. G. *J. Am. Chem. Soc.* **2006**, 128 (4), 1390–1393.
- (35) Feng, N.; He, P.; Zhou, H. *Adv. Energy Mater.* **2016**, 6 (9), 1–24.
- (36) Read, J. J. *Electrochem. Soc.* **2006**, 153 (1), A96.
- (37) Freunberger, S. A.; Chen, Y.; Drewett, N. E.; Hardwick, L. J.; Bardé, F.; Bruce, P. G. *Angew. Chemie - Int. Ed.* **2011**, 50 (37), 8609–8613.
- (38) Sharon, D.; Afri, M.; Noked, M.; Garsuch, A.; Frimer, A. A.; Aurbach, D. *J. Phys. Chem. Lett.* **2013**, 4 (18), 3115–3119.
- (39) Peng, Z.; Freunberger, S. a; Chen, Y.; Bruce, P. G.; Battery, L. *Science (80-.)*. **2012**, 337 (6094), 563–566.
- (40) Ottakam Thotiyl, M. M.; Freunberger, S. A.; Peng, Z.; Chen, Y.; Liu, Z.; Bruce, P. G. *Nat. Mater.* **2013**, 12, 1050.
- (41) Scrosati, B. *Angew. Chemie Int. Ed.* **2015**, 54 (19), 5554.
- (42) Xu, W.; Hu, J.; Engelhard, M. H.; Towne, S. A.; Hardy, J. S.; Xiao, J.; Feng, J.; Hu, M. Y.; Zhang, J.; Ding, F.; Gross, M. E.; Zhang, J. G. *J. Power Sources* **2012**, 215, 240–247.
- (43) Mizuno, F.; Takechi, K.; Higashi, S.; Shiga, T.; Shiotsuki, T.; Takazawa, N.; Sakurabayashi, Y.; Okazaki, S.; Nitta, I.; Kodama, T.; Nakamoto, H.; Nishikoori, H.; Nakanishi, S.; Kotani, Y.; Iba, H. *J. Power Sources* **2013**, 228, 47–56.
- (44) Ottakam Thotiyl, M. M.; Freunberger, S. A.; Peng, Z.; Bruce, P. G. *J. Am. Chem. Soc.* **2013**, 135 (1), 494–500.
- (45) McCloskey, B. D.; Speidel, A.; Scheffler, R.; Miller, D. C.; Viswanathan, V.; Hummelshøj, J. S.; Nørskov, J. K.; Luntz, A. C. *J. Phys. Chem. Lett.* **2012**, 3 (8), 997–1001.
- (46) Adams, B. D.; Black, R.; Radtke, C.; Williams, Z.; Mehdi, B. L.; Browning, N. D.; Nazar, L. F. *ACS Nano* **2014**, 8 (12), 12483–12493.
- (47) McCloskey, B. D.; Bethune, D. S.; Shelby, R. M.; Mori, T.; Scheffler, R.; Speidel, A.; Sherwood, M.; Luntz, A. C. *J Phys Chem Lett* **2012**, 3, 3043–3047.
- (48) Bryantsev, V. S.; Giordani, V.; Walker, W.; Blanco, M.; Zecevic, S.; Sasaki, K.; Uddin, J.; Addison, D.; Chase, G. V. *J. Phys. Chem. A* **2011**, 115 (44), 12399–12409.
- (49) Bryantsev, V. S.; Faglioni, F. *J. Phys. Chem. A* **2012**, 116 (26), 7128–7138.

- (50) Genorio, B.; Staszak-Jirkovský, J.; Assary, R. S.; Connell, J. G.; Strmcnik, D.; Diesendruck, C. E.; Lopes, P. P.; Stamenkovic, V. R.; Moore, J. S.; Curtiss, L. A.; Markovic, N. M. *J. Phys. Chem. C* **2016**, *120* (29), 15909–15914.
- (51) Zhang, Z.; Lu, J.; Assary, R. S.; Du, P.; Wang, H.-H.; Sun, Y.-K.; Qin, Y.; Lau, K. C.; Greeley, J.; Redfern, P. C.; Iddir, H.; Curtiss, L. A.; Amine, K. *J. Phys. Chem. C* **2011**, *115* (51), 25535–25542.
- (52) Liu, B.; Xu, W.; Yan, P.; Sun, X.; Bowden, M. E.; Read, J.; Qian, J.; Mei, D.; Wang, C.-M.; Zhang, J.-G. *Adv. Funct. Mater.* **2016**, *26* (4), 605–613.
- (53) Carboni, M.; Marrani, A. G.; Spezia, R.; Brutti, S. *Chem. – A Eur. J.* **2016**, *22* (48), 17188–17203.
- (54) Bryantsev, V. S. *Chem. Phys. Lett.* **2013**, *558*, 42–47.
- (55) Assary, R. S.; Lau, K. C.; Amine, K.; Sun, Y.-K.; Curtiss, L. A. *J. Phys. Chem. C* **2013**, *117* (16), 8041–8049.
- (56) Aurbach, D.; McCloskey, B. D.; Nazar, L. F.; Bruce, P. G. *Nat. Energy* **2016**, *1*, 16128.
- (57) Assary, R. S.; Lu, J.; Du, P.; Luo, X.; Zhang, X.; Ren, Y.; Curtiss, L. A.; Amine, K. *ChemSusChem* **2013**, *6* (1), 51–55.
- (58) Wang, H. H.; Lee, Y. J.; Assary, R. S.; Zhang, C.; Luo, X.; Redfern, P. C.; Lu, J.; Lee, Y. J.; Kim, D. H.; Kang, T. G.; Indacochea, E.; Lau, K. C.; Amine, K.; Curtiss, L. A. *J. Phys. Chem. C* **2017**, *121* (18), 9657–9661.
- (59) Zhang, Y.; Zhang, X.; Wang, J.; McKee, W. C.; Xu, Y.; Peng, Z. *J. Phys. Chem. C* **2016**, *120* (7), 3690–3698.
- (60) Wandt, J.; Jakes, P.; Granwehr, J.; Gasteiger, H. A.; Eichel, R. A. *Angew. Chemie - Int. Ed.* **2016**, *55*, 6892–6895.
- (61) Chen, Y.; Freunberger, S. a; Peng, Z.; Bardé, F.; Bruce, P. G. *J. Am. Chem. Soc.* **2012**, *134* (18), 7952–7957.
- (62) McCloskey, B. D.; Valery, A.; Luntz, A. C.; Gowda, S. R.; Wallraff, G. M.; Garcia, J. M.; Mori, T.; Krupp, L. E. *J. Phys. Chem. Lett.* **2013**, *4* (17), 2989–2993.
- (63) Schafzahl, B.; Mourad, E.; Schafzahl, L.; Petit, Y. K.; Raju, A. R.; Thotiyl, M. O.; Wilkening, M.; Slugovc, C.; Freunberger, S. A. *ACS Energy Lett.* **2017**, 170–176.
- (64) Holleman, A.F., Wiberg, Egon, Wiberg, N. *Lehrbuch der Anorganischen Chemie*, 102nd ed.; Walter de Gruyter & Co.: Berlin, 2007.
- (65) Kunze, U. R., Schwedt, G. *Grundlagen der Quantitativen Analyse*; WILEY-VCH Verlag: Weinheim, 2009.
- (66) Meini, S.; Piana, M.; Tsiouvaras, N.; Garsuch, A.; Gasteiger, H. A. *Electrochem. Solid-State Lett.* **2012**, *15* (4), A45.
- (67) Hartmann, P.; Bender, C. L.; Sann, J.; Dürr, A. K.; Jansen, M.; Janek, J.; Adelhelm, P. *Phys. Chem. Chem. Phys.* **2013**, *15* (28), 11661.
- (68) Ren, X.; Lau, K. C.; Yu, M.; Bi, X.; Kreidler, E.; Curtiss, L. A.; Wu, Y. *ACS Appl. Mater. Interfaces* **2014**, *6*, 19299–19307.
- (69) Giordani, V.; Freunberger, S. A.; Bruce, P. G.; Tarascon, J.-M.; Larcher, D. *Electrochem. Solid-State Lett.* **2010**, *13* (12), A180.
- (70) De Laat, J.; Gallard, H. *Environ. Sci. Technol.* **1999**, *33* (16), 2726–2732.
- (71) Zhai, D.; Wang, H. H.; Yang, J.; Lau, K. C.; Li, K.; Amine, K.; Curtiss, L. A. *J. Am. Chem. Soc.* **2013**, *135* (41), 15364–15372.
- (72) Lu, J.; Lee, Y. J.; Luo, X.; Lau, K. C.; Asadi, M.; Wang, H. H.; Brombosz, S.; Wen, J.; Zhai, D.; Chen,

- Z.; Miller, D. J.; Jeong, Y. S.; Park, J. B.; Fang, Z. Z.; Kumar, B.; Salehi-Khojin, A.; Sun, Y. K.; Curtiss, L. A.; Amine, K. *Nature* **2016**, 529 (7586), 377–382.
- (73) Kang, J.-H.; Kwak, W.-J.; Aurbach, D.; Sun, Y.-K. *J. Mater. Chem. A* **2017**, 5 (39), 20678–20686.
- (74) Duesterberg, C. K.; Mylon, S. E.; Waite, T. D.; Duesterberg, C. K. **2008**, 42 (October), 8522–8527.
- (75) Duesterberg, C. K.; Cooper, W. J.; Waite, T. D. *Environ. Sci. Technol.* **2005**, 39 (13), 5052–5058.
- (76) Gachot, G.; Grugeon, S.; Armand, M.; Pilard, S.; Guenot, P.; Tarascon, J. M.; Laruelle, S. *J. Power Sources* **2008**, 178 (1), 409–421.
- (77) Gireaud, L.; Grugeon, S.; Laruelle, S.; Pilard, S.; Tarascon, J.-M. *J. Electrochem. Soc.* **2005**, 152 (5), A850.
- (78) Sasaki, T.; Abe, T.; Iriyama, Y.; Inaba, M.; Ogumi, Z. *J. Power Sources* **2005**, 150 (1–2), 208–215.
- (79) Gireaud, L.; Grugeon, S.; Pilard, S.; Guenot, P.; Tarascon, J. M.; Laruelle, S. *Anal. Chem.* **2006**, 78 (11), 3688–3698.
- (80) Bryngelsson, H.; Stjerndahl, M.; Gustafsson, T.; Edström, K. *J. Power Sources* **2007**, 174 (2), 970–975.
- (81) Sing, K. S. W. *Pure Appl. Chem.* **1985**, 57 (4), 603–619.
- (82) Cameron, N. R.; Krajnc, P.; Silverstein, M. S. In *Porous Polymers*; John Wiley & Sons, Inc., 2011; pp 119–172.
- (83) Rose, M.; Klein, N.; Senkovska, I.; Schrage, C.; Wollmann, P.; Böhlmann, W.; Böhringer, B.; Fichtner, S.; Kaskel, S. *J. Mater. Chem.* **2011**, 21 (3), 711–716.
- (84) Svec, F. *J. Chromatogr. A* **2010**, 1217 (6), 902–924.
- (85) Olson, D. A.; Chen, L.; Hillmyer, M. A. *Chem. Mater.* **2008**, 20 (3), 869–890.
- (86) Kim, J. K.; Yang, S. Y.; Lee, Y.; Kim, Y. *Prog. Polym. Sci.* **2010**, 35 (11), 1325–1349.
- (87) Jiang, J.-X.; Trewin, A.; Su, F.; Wood, C. D.; Niu, H.; Jones, J. T. A.; Khimiyak, Y. Z.; Cooper, A. I. *Macromolecules* **2009**, 42 (7), 2658–2666.
- (88) Rzaev, J.; Hillmyer, M. A. *Macromolecules* **2005**, 38 (1), 3–5.
- (89) Du, N.; Robertson, G. P.; Song, J.; Pinnau, I.; Thomas, S.; Guiver, M. D. *Macromolecules* **2008**, 41 (24), 9656–9662.
- (90) Hu, X.; An, Q.; Li, G.; Tao, S.; Liu, J. *Angew. Chemie Int. Ed.* **2006**, 45 (48), 8145–8148.
- (91) Thomas, A.; Goettmann, F.; Antonietti, M. *Chem. Mater.* **2008**, 20 (3), 738–755.
- (92) Lu, A.-H.; Schüth, F. *Adv. Mater.* **2006**, 18 (14), 1793–1805.
- (93) Stein, A.; Li, F.; Denny, N. R. *Chem. Mater.* **2008**, 20 (3), 649–666.
- (94) Wu, D.; Xu, F.; Sun, B.; Fu, R.; He, H.; Matyjaszewski, K. *Chem. Rev.* **2012**, 112 (7), 3959–4015.
- (95) Hillmyer, M. A. Abetz, V., Ed.; Springer Berlin Heidelberg: Berlin, Heidelberg, 2005; pp 137–181.
- (96) Rzaev, J.; Hillmyer, M. A. *J. Am. Chem. Soc.* **2005**, 127 (38), 13373–13379.
- (97) Al-Muhtaseb, S. A.; Ritter, J. A. *Adv. Mater.* **2003**, 15 (2), 101–114.
- (98) Tsyurupa, M. P.; Davankov, V. A. *React. Funct. Polym.* **2006**, 66 (7), 768–779.
- (99) Mastalerz, M. *Angew. Chemie Int. Ed.* **2008**, 47 (3), 445–447.
- (100) Doonan, C. J.; Tranchemontagne, D. J.; Glover, T. G.; Hunt, J. R.; Yaghi, O. M. *Nat. Chem.* **2010**, 2 (3), 235–238.
- (101) Nagai, A.; Guo, Z.; Feng, X.; Jin, S.; Chen, X.; Ding, X.; Jiang, D. *Nat. Commun.* **2011**, 2, 536.

- (102) Liu, X.; Basu, A. *J. Am. Chem. Soc.* **2009**, *131* (16), 5718–5719.
- (103) Li, Z.; Yang, Y.-W. *J. Mater. Chem. B* **2017**.
- (104) Liu, F.; Wang, S.; Lin, G.; Chen, S. *New J. Chem.* **2017**.
- (105) Schacher, F.; Ulbricht, M.; Müller, A. H. E. *Adv. Funct. Mater.* **2009**, *19* (7), 1040–1045.
- (106) Yang, S. Y.; Park, J.; Yoon, J.; Ree, M.; Jang, S. K.; Kim, J. K. *Adv. Funct. Mater.* **2008**, *18* (9), 1371–1377.
- (107) Fan, W.; Zhang, L.; Liu, T. *Mater. Chem. Front.* **2017**.
- (108) Kou, Y.; Xu, Y.; Guo, Z.; Jiang, D. *Angew. Chemie Int. Ed.* **2011**, *50* (37), 8753–8757.
- (109) Wu, D.; Fu, R.; Dresselhaus, M. S.; Dresselhaus, G. *Carbon N. Y.* **2006**, *44* (4), 675–681.
- (110) Zeng, Q.; Wu, D.; Zou, C.; Xu, F.; Fu, R.; Li, Z.; Liang, Y.; Su, D. *Chem. Commun.* **2010**, *46* (32), 5927.
- (111) Zou, C.; Wu, D.; Li, M.; Zeng, Q.; Xu, F.; Huang, Z.; Fu, R. *J. Mater. Chem.* **2010**, *20* (4), 731–735.
- (112) Silverstein, M. S. *Prog. Polym. Sci.* **2014**, *39* (1), 199–234.
- (113) Manley, S. S.; Graeber, N.; Grof, Z.; Menner, A.; Hewitt, G. F.; Stepanek, F.; Bismarck, A. *Soft Matter* **2009**, *5* (23), 4780.
- (114) Kimmins, S. D.; Cameron, N. R. *Adv. Funct. Mater.* **2011**, *21* (2), 211–225.
- (115) Butler, R.; Hopkinson, I.; Cooper, A. I. *J. Am. Chem. Soc.* **2003**, *125* (47), 14473–14481.
- (116) Butler, R.; Davies, C. M.; Hopkinson, I.; Cooper, A. I. *Am. Chem. Soc. Polym. Prepr. Div. Polym. Chem.* **2002**, *43* (1), 744–745.
- (117) Lee, J.-Y.; Tan, B.; Cooper, A. I. *Macromolecules* **2007**, *40* (6), 1955–1961.
- (118) Shirshova, N.; Bismarck, A.; Steinke, J. H. G. *Macromol. Rapid Commun.* **2011**, *32* (23), 1899–1904.
- (119) Gurevitch, I.; Silverstein, M. S. *Macromolecules* **2011**, *44* (9), 3398–3409.
- (120) Lovelady, E.; Kimmins, S. D.; Wu, J.; Cameron, N. R. *Polym. Chem.* **2011**, *2* (3), 559–562.
- (121) Kovačič, S.; Krajnc, P.; Slugovc, C. *Chem. Commun.* **2010**, *46* (40), 7504.
- (122) Yao, C.; Qi, L.; Jia, H.; Xin, P.; Yang, G.; Chen, Y. *J. Mater. Chem.* **2009**, *19* (6), 767–772.
- (123) Li, T.; Liu, H.; Zeng, L.; Yang, S.; Li, Z.; Zhang, J.; Zhou, X. *J. Mater. Chem.* **2011**, *21* (34), 12865–12872.
- (124) Ikem, V. O.; Menner, A.; Bismarck, A. *Langmuir* **2010**, *26* (11), 8836–8841.
- (125) Pickering, S. U. *J. Chem. Soc. Trans.* **1907**, *91* (0), 2001–2021.
- (126) Menner, A.; Ikem, V.; Salgueiro, M.; Shaffer, M. S. P.; Bismarck, A. *Chem. Commun.* **2007**, *c* (41), 4274.
- (127) Ikem, V. O.; Menner, A.; Horozov, T. S.; Bismarck, A. *Adv. Mater.* **2010**, *22* (32), 3588–3592.
- (128) Ikem, V. O.; Menner, A.; Bismarck, A. *Soft Matter* **2011**, *7* (14), 6571.
- (129) Wong, L. L. C.; Ikem, V. O.; Menner, A.; Bismarck, A. *Macromol. Rapid Commun.* **2011**, *32* (19), 1563–1568.
- (130) Barbetta, A.; Dentini, M.; Leandri, L.; Ferraris, G.; Coletta, A.; Bernabei, M. *React. Funct. Polym.* **2009**, *69* (9), 724–736.
- (131) Schwab, M. G.; Senkovska, I.; Rose, M.; Klein, N.; Koch, M.; Pahnke, J.; Jonschker, G.; Schmitz, B.; Hirscher, M.; Kaskel, S. *Soft Matter* **2009**, *5* (5), 1055.

- (132) Gross, A. F.; Nowak, A. P. *Langmuir* **2010**, *26* (13), 11378–11383.
- (133) Vílchez, S.; Pérez-Carrillo, L. A.; Miras, J.; Solans, C.; Esquena, J. *Langmuir* **2012**, *28* (20), 7614–7621.
- (134) Woodward, R. T.; Jobbe-Duval, A.; Marchesini, S.; Anthony, D. B.; Petit, C.; Bismarck, A. *Polym. (United Kingdom)* **2017**, *115*, 146–153.
- (135) Zhang, H.; Hardy, G. C.; Khimiyak, Y. Z.; Rosseinsky, M. J.; Cooper, A. I. *Chem. Mater.* **2004**, *16* (22), 4245–4256.
- (136) Zhang, H.; Cooper, A. I. *Ind. Eng. Chem. Res.* **2005**, *44* (23), 8707–8714.
- (137) Zhang, Y.; Liang, H.; Zhao, C. Y.; Liu, Y. *J. Mater. Sci.* **2009**, *44* (3), 931–938.
- (138) Zou, G.; Wang, H.; Mara, N.; Luo, H.; Li, N.; Di, Z.; Bauer, E.; Wang, Y.; McCleskey, T.; Burrell, A.; Zhang, X.; Nastasi, M.; Jia, Q. *J. Am. Chem. Soc.* **2010**, *132* (8), 2516–2517.
- (139) Koc, R. *J. Mater. Sci.* **1998**, *33*, 1049–1055.
- (140) Fu, C.; Li, M.; Li, H.; Li, C.; Qu, C.; Yang, B. *Mater. Sci. Eng. C* **2017**, *72*, 425–432.
- (141) Bersani, M.; Paduano, A.; Favaro, M.; Koshy, P.; Sorrell, C. C.; Martucci, A.; Granozzi, G. *Ceram. Int.* **2016**, *42* (6), 7690–7696.
- (142) Berger, L. M.; Gruner, W.; Langholf, E.; Stolle, S. *Int. J. Refract. Met. Hard Mater.* **1999**, *17* (1–3), 235–243.
- (143) Preiss, H.; Berger, L.-M.; Schultze, D. *J. Eur. Ceram. Soc.* **1999**, *19* (2), 195–206.
- (144) Wang, X.; Lu, M.; Qiu, L.; Huang, H.; Li, D.; Wang, H.; Cheng, Y. B. *Ceram. Int.* **2016**, *42* (1), 122–131.
- (145) Xia, X.; Zhang, Y.; Chao, D.; Xiong, Q.; Fan, Z.; Tong, X.; Tu, J.; Zhang, H.; Fan, H. *J. Energy Environ. Sci.* **2015**, *8* (5), 1559–1568.
- (146) Tao, X.; Du, J.; Yang, Y.; Li, Y.; Xia, Y.; Gan, Y.; Huang, H.; Zhang, W.; Li, X. *Cryst. Growth Des.* **2011**, *11* (10), 4422–4426.
- (147) Gotoh, Y.; Fujimura, K.; Koike, M.; Ohkoshi, Y.; Nagura, M.; Akamatsu, K.; Deki, S. *Mater. Res. Bull.* **2001**, *36* (13), 2263–2275.
- (148) Ma, Y.; Bao, C.; Han, L.; Chen, J. *J. Mater. Eng. Perform.* **2017**, *26* (2), 636–643.
- (149) Ramos, J. P.; Senos, A. M. R.; Stora, T.; Fernandes, C. M.; Bowen, P. *J. Eur. Ceram. Soc.* **2017**, *37* (13), 3899–3908.
- (150) Kovačič, S. *Acta Chim. Slov.* **2013**, *60* (2), 448–454.
- (151) Reichardt, C.; Welton, T. In *Solvents and Solvent Effects in Organic Chemistry*; Wiley-VCH Verlag GmbH & Co. KGaA, 2010; pp 425–508.
- (152) Zhao, Z.; Zhang, X.; Zhang, G.; Liu, Z.; Qu, D.; Miao, X.; Feng, P.; Sun, Z. *Nano Res.* **2015**, *8* (12), 4061–4071.
- (153) Zhang, L. F.; Hu, J. J.; Voevodin, A. A.; Fong, H. *Nanoscale* **2010**, *2* (9), 1670–1673.
- (154) Del Franco, G. J. Tetra(5-norbornen-2-methyl)titanate. US 3342842, 1967.
- (155) Kovačič, S.; Preishuber-Pflügl, F.; Slugovc, C. *Macromol. Mater. Eng.* **2014**, *299* (7), 843–850.
- (156) Hassoun, J.; Croce, F.; Armand, M.; Scrosati, B. *Angew. Chemie - Int. Ed.* **2011**, *50* (13), 2999–3002.
- (157) Adam, W.; Kazakov, D. V.; Kazakov, V. P. *Chem. Rev.* **2005**, *105* (9), 3371–3387.
- (158) Ogilby, P. R. *Chem. Soc. Rev.* **2010**, *39*, 3181–3209.

- (159) Mulliken, R. S. *Phys. Rev.* **1929**, 33 (5), 730–747.
- (160) Schweitzer, C.; Schmidt, R. *Chem. Rev.* **2003**, 103 (5), 1685–1757.
- (161) McKeown, B.; Waters, W. A. *J. Chem. Soc.* **1966**, B, 1040–1046.
- (162) Ogilby, P. R. P.; Foote, C. C. S. *J. Am. Chem. Soc.* **1981**, 103 (11), 3423–3430.
- (163) Badger, R. M.; Wright, A. C.; Whitlock, R. F. *J. Chem. Phys.* **1965**, 43 (12), 4345–4350.
- (164) Li, Q.; Chen, F.; Zhao, W.; Xu, M.; Fang, B.; Zhang, Y.; Duo, L.; Jin, Y.; Sang, F. *Bull. Korean Chem. Soc.* **2007**, 28 (10), 1656–1660.
- (165) Guiraud, H. J.; Foote, C. S. *J. Am. Chem. Soc.* **1976**, 98 (7), 1984–1986.
- (166) Khan, A. U. *Science* (80-). **1970**, 168 (3930), 476 LP-477.
- (167) Carlsson, D. J. *J. Polym. Sci. Polym. Lett. Ed.* **1978**, 16 (9), 485–486.
- (168) Enko, B.; Borisov, S. M.; Regensburger, J.; B??umler, W.; Gescheidt, G.; Klimant, I. *J. Phys. Chem. A* **2013**, 117 (36), 8873–8882.
- (169) Aubry, J. M.; Pierlot, C.; Rigaudy, J.; Schmidt, R. *Acc. Chem. Res.* **2003**, 36 (9), 668–675.
- (170) Stevens, B.; Perez, S. R.; Ors, J. A. *J. Am. Chem. Soc.* **1974**, 96 (1), 6846–6850.
- (171) Thotiyil, M. M. O.; Freunberger, S. a; Peng, Z.; Bruce, P. G. *J. Am. Chem. Soc.* **2013**, 135 (1), 494–500.
- (172) Schafzahl, L.; Mahne, N.; Schafzahl, B.; Wilkening, M.; Slugovc, C.; Borisov, S. M.; Freunberger, S. A. *Angew. Chemie Int. Ed.* **2017**, 15728–15732.
- (173) Bryantsev, V. S.; Blanco, M.; Faglioni, F. *J. Phys. Chem. A* **2010**, 114 (31), 8165–8169.
- (174) Blanco, J. M.; Fernández, F.; García-Mera, X.; Rodríguez-Borges, J. E. *Tetrahedron* **2002**, 58 (43), 8843–8849.